The Astrophysical Journal, 942:74 (43pp), 2023 January 10 https://doi.org/10.3847/1538-4357/ac9411

Turbulence in Particle-laden Midplane Layers of Planet-forming Disks

Debanjan Sengupta[1,2,3,4] and Orkan M. Umurhan[1,5,6]
[1] NASA Ames Research Center, Mail Stop 245-3, Moffett Field, CA 94035, USA
[2] Universities Space Research Association; 7178 Columbia Gateway Drive, Columbia, MD 21046, USA
[3] Department of Astronomy, New Mexico State University, Las Cruces, NM 88003-8001, USA; debanjan@nmsu.edu
[4] NASA Postdoctoral Program (NPP) Fellow
[5] SETI Institute, 389 Bernardo Way, Mountain View, CA 94043, USA; oumurhan@seti.org
[6] Cornell Center for Astrophysics and Planetary Sciences, Cornell University, Ithaca, NY 14853, USA
Received 2022 April 1; revised 2022 September 17; accepted 2022 September 19; published 2023 January 12

Abstract

We examine the settled particle layers of planet-forming disks in which the streaming instability (SI) is thought to be either weak or inactive. A suite of low-to-moderate-resolution 3D simulations in a $0.2H$-sized box, where H is the pressure scale height, are performed using PENCIL for two Stokes numbers, $\mathrm{St} = 0.04$ and 0.2, at 1% disk metallicity. We find that a complex of Ekman-layer jet flows emerge subject to three co-acting linearly growing processes: (1) the Kelvin–Helmholtz instability (KHI), (2) the planet-forming disk analog of the baroclinic Symmetric Instability (SymI), and (3) a later-time weakly acting secondary transition process, possibly a manifestation of the SI, producing a radially propagating pattern state. For $\mathrm{St} = 0.2$ KHI is dominant and manifests as off-midplane axisymmetric rolls, while for $\mathrm{St} = 0.04$ the axisymmetric SymI mainly drives turbulence. SymI is analytically developed in a model disk flow, predicting that it becomes strongly active when the Richardson number (Ri) of the particle–gas midplane layer transitions below 1, exhibiting growth rates $\leqslant \sqrt{2/\mathrm{Ri} - 2} \cdot \Omega$, where Ω is the local disk rotation rate. For fairly general situations absent external sources of turbulence it is conjectured that the SI, when and if initiated, emerges out of a turbulent state primarily driven and shaped by at least SymI and/or KHI. We also find that turbulence produced in 256^3 resolution simulations are not statistically converged and that corresponding 512^3 simulations may be converged for $\mathrm{St} = 0.2$. Furthermore, we report that our numerical simulations significantly dissipate turbulent kinetic energy on scales less than six to eight grid points.

Unified Astronomy Thesaurus concepts: Astrophysical fluid dynamics (101); Planetesimals (1259); Protoplanetary disks (1300); Hydrodynamical simulations (767)

1. Introduction

An understanding of how the basic building blocks of planets form remains elusive. In the standard picture, the nascent solar nebula is populated with submicron grains that, through collisional sticking, grow until they reach millimeter to centimeter scales; however, various dynamical growth barriers prevent further incremental growth en route to the eventual formation of these 50–100 km sized planetesimals (for a deeper discussion see Estrada et al. 2016; Drazkowska et al. 2022). Overcoming the so-called centimeter barrier has been the subject of intense research for up to two decades now. Several proposed routes that can circumvent this barrier and produce overdensities that are gravitationally bound have been considered of late, including (but not limited to) particle concentration by giant vortices (see recent work by Lyra et al. 2018; Raettig et al. 2021) and particle density enhancements resulting from turbulent concentration (e.g., Chambers 2010; Hartlep & Cuzzi 2020). The leading candidate process, having received the most attention, is the streaming instability (SI; Youdin & Goodman 2005; Johansen et al. 2007), which can routinely produce gravitationally bound overdensities (e.g., Simon et al. 2017; Abod et al. 2019). The SI—which produces high-density clumps through a strong resonance between two counterflowing streams (Squire & Hopkins 2018a)—is promising for several reasons, including the correspondence between the observed angular momentum orientation distribution of cold classical Kuiper Belt objects and that of gravitationally bound overdensities produced in high-resolution SI simulations (Nesvorný et al. 2019). On the other hand, if planetesimal-forming disk regions experience some kind of hydrodynamic or magnetohydrodynamic turbulence (see, e.g., review of Lyra & Umurhan 2019), the efficacy of the SI at producing gravitationally bound overdensities remains uncertain and subject to ongoing debate (Chen & Lin 2020; Gole et al. 2020; Schäfer et al. 2020; Umurhan et al. 2020).

For what protoplanetary disk conditions, then, should the SI be expected to lead to clumps dense enough to trigger gravitational collapse? Assuming that the disk is not subject to some sort of external turbulence source and the disk's particle size distribution is monodisperse, this question has been rephrased by asking what combination of disk metallicity (Z) and particle Stokes number (St) leads to SI activity strong enough to produce gravitationally bound overdensities (Carrera et al. 2015; Yang et al. 2017; Li & Youdin 2021)? Based on a survey of 3D axisymmetric and full 3D particle–gas simulations, these studies have sought to determine a critical St-number-dependent metallicity, $Z_c(\mathrm{St})$, for which values of $Z > Z_c$ are likely to lead to gravitationally bound clumps. Up until recently, Z_c appeared to be parabolic-like in St, with a minimum value $Z_{c,\min} \approx 0.015$ occurring roughly at around $\mathrm{St} \approx 0.04$. However, during the preparation stage of this manuscript the study by Li & Youdin (2021) was released, suggesting that this minimum Z_c value may go well below $Z = 0.01$, occurring at $\mathrm{St} \approx 0.3$ instead, and that Z_c shows a

strong upward jump in value for values of $\mathrm{St} \lessapprox 0.015$. The reasons for the discrepancies between these various investigations have yet to be clarified. A further important clue was identified by Sekiya & Onishi (2018), who, based on an independent parameter study of the SI, conjecture that the outcome of particle–gas disk simulations is actually a function of St and the ratio Z/Π, where Π is the nondimensionalization of a disk's local background radial pressure gradient.

In almost all cases considered, midplane-settled particle layers go through a nominally turbulent pre-clump phase before strong clumping manifests; this is especially true for input values of $\mathrm{St} \lessapprox 0.1$, where this turbulent phase can last up to several dozens of orbit times. For values of $Z < Z_c$ this turbulent state appears to persist relatively unabated (see, e.g., the corresponding simulations of Sekiya & Onishi 2018).

It is generally assumed that the SI simultaneously coexists and/or emerges out of a shear-driven turbulent state. This shear state, originally envisioned by Weidenschilling (1980) to be central to particle–disk scenarios, and leading to the Kelvin–Helmholtz instability ("KHI" hereafter) and roll-up ("KH roll-up" hereafter), should also develop Ekman-type flow structure owing to the presence of strong rotation (Cuzzi et al. 1993; Dobrovolskis et al. 1999). In the recent study of full 3D particle–disk simulations by Gerbig et al. (2020) it was shown that for input parameters Z and St that should *not* lead to strong SI activity, the Richardson numbers (Ri) of the turbulent state seem to routinely exceed the classical limiting value of $1/4$ expected for nonrotating stratified flow setups (Howard 1961; Miles 1961). Indeed, there have been a series of antecedent studies considering the problem of KH roll-up with strong rotation either in a restricted nonaxisymmetric 2D geometry (i.e., dynamics restricted to the azimuthal–vertical plane of the disk, most notably Gómez & Ostriker 2005; Johansen et al. 2006; Barranco 2009) or considered in full 3D via a facsimile single-fluid model with an imposed composition gradient (Barranco 2009; Lee et al. 2010a, 2010b). All of these studies indicate that activity may persist for values of $\mathrm{Ri} > 1/4$ and likely less than $\mathrm{Ri} < 1$ and conclude that rotation somehow pushes the boundary of stability away from the traditional value of $1/4$; exactly how far this boundary extends is not settled under the relevant conditions.

With these considerations in mind, we set out to better understand how midplane-settled protoplanetary disk particle layers behave when the SI is either weak or effectively extinguished. In this study we are focused on disk models with no external sources of turbulence. One set of specific aims here is to characterize the shear flow that manifests within the streaming layer, to witness its transformation into a nonsteady (and likely turbulent) state, and to identify the mechanism(s) that drive this transition. Could the insights gained as a result of this exercise lead to better understanding of the $\mathrm{Ri} > 1/4$ findings of Gerbig et al. (2020)?

The study by Sekiya & Onishi (2018) offers some preliminary glimpses. These authors conducted a suite of low-to-moderate-resolution simulations (that include parameter inputs that do not lead to strong density clumping) in which they showcase vertically integrated particle density that manifests azimuthally oriented banded structure. Presumably the rotationally modified KHI or some other fluid dynamical process(es), possibly including a very weak operation of the SI, sculpts these phenomena. In this regard the unpublished study of Ishitsu et al. (2009) offers further insights wherein they investigated the purely 3D axisymmetric development of a settled particle–gas midplane layer, finding relatively pronounced fluid dynamical development in three to five orbit times for low St (=0.001) with correspondingly weak and/or dispersed particle clumping (in particular see Figure 3 of Ishitsu et al. 2009). Understanding the flow structure underpinning this effect when particle clumping is weak and St is low therefore deserves further scrutiny: what about the underlying flow state thwarts the SI's emergence?

Another one of our broader aims is to characterize the turbulent kinetic energy spectra during various stages of the layer's development in order to help assess the kind of turbulence that might be emerging. Beyond very recent investigations reported in the geophysical fluid dynamics literature, little is known about the character and nature of the turbulent kinetic energy spectrum in flows that are simultaneously subject to strong rotation and stratification (Alexakis & Biferale 2018). Moreover, beyond brief glimpses reported in Li et al. (2018), to our knowledge there seem to be no published insights in the matter for protoplanetary disk scenarios like those considered here.

We approach these questions by conducting a limited series of 3D axisymmetric and full 3D particle–gas shearing-box numerical simulations employing the widely used numerical platform PENCIL. We follow the approach taken by numerous previous investigators in our initial setup by adopting a monodisperse distribution of particles characterized by a single St and positioned along a Gaussian distribution with respect to the disk midplane. There are no external sources of turbulence. The experiment is then monitored as the particles collapse and drive dynamical activity. Our simulations do not have particle self-gravity turned on at any stage. We consider two values of St, 0.04 and 0.2, with a metallicity of $Z = 0.01$, as parameter inputs that ought not lead to active SI and/or putatively Roche density exceeding overdensities—e.g., as based on Figure 8 of Carrera et al. (2015) and Figure 9 of Yang et al. (2017).[7] In this sense, our parameter inputs might be considered analogous to the subset of those examined by Sekiya & Onishi (2018) that lead to weak clump production. We wish to better understand the emergent flow state under these weakly clumping conditions in order to extend the insights made by Sekiya & Onishi (2018) in this regard. As such, we are primarily concerned with the particle–gas dynamical state right on up to the point where either the SI emerges, in some possibly weak incarnation, or the flow exhibits a patterned state.

This study is organized as follows. In Section 2, we present the numerical model and simulation setup with the publicly available PENCIL code. The results of these hydrodynamic simulations with particles and gas, especially the system's transition to a turbulent state, are discussed in Section 3. In Section 4, the turbulence statistics from the simulations are analyzed, which include a calibration of PENCIL. A selected set of linear theory analyses for the dynamics of the shear-driven midplane-settled particle layer is presented in Section 5 using tools independent of PENCIL. We discuss our findings and their implications in the context of several previous studies in Section 6. Given the substantial content of this paper, readers are encouraged first to skip to Section 7, where we, in brief, summarize the main findings of this work.

[7] However, as noted earlier, Li & Youdin (2021) report that the SI ought to be active for both sets of model parameters we have adopted here. We keep this in mind throughout this discussion.

Table 1
Variables Used in Theoretical Modeling

Variable	Meaning
H, H_g	Gas scale height (appearing interchangeably)
H_p	Particle scale height
Ω, Ω_0	Keplerian frequency (appearing interchangeably)
R	Orbital distance from central star
V_K	Keplerian velocity
$\boldsymbol{U}_g$	Total gas velocity vector
$\boldsymbol{u}_g$	Perturbation gas velocity vector
u_g, v_g, w_g	Three components of gas velocity
$\langle u_g\rangle_y$, $\langle v_g\rangle_y$, $\langle w_g\rangle_y$	Azimuthal average of gas velocities
$\langle u_g\rangle_{xy}$, $\langle v_g\rangle_{xy}$, $\langle w_g\rangle_{xy}$	Radial–azimuthal average of gas velocities
$\boldsymbol{U}_p$	Total particle fluid velocity vector
$\boldsymbol{u}_p$	Perturbation particle fluid velocity vector
u_p, v_p, w_p	Three components of particle fluid velocity
$\langle u_p\rangle_y$, $\langle v_p\rangle_y$, $\langle w_p\rangle_y$	Azimuthal average of particle fluid velocities
$\langle u_p\rangle_{xy}$, $\langle v_p\rangle_{xy}$, $\langle w_p\rangle_{xy}$	Radial–azimuthal average of particle fluid velocities
$\boldsymbol{x}_\mathrm{i}$	Position vector for particle i
$\boldsymbol{u}_{pi}$	Lagrangian velocity vector for particle i
x_i, y_i, z_i	Three components of particle i's position
u_{pi}, v_{pi}, w_{pi}	Three components of particle i's Lagrangian velocity
c_s	Local isothermal sound speed
α	Turbulence strength
ρ_g	Gas volume density
ρ_p	Particle volume density
ρ_m	Box-averaged mean solid density
ϵ	Dust-to-gas mass ratio
$\rho_{g,0}$	Azimuthally averaged midplane ρ_g
$\langle\rho_p\rangle_{y,0}$	Azimuthally averaged midplane ρ_p
$\langle\rho_p\rangle_{xy}$	Radial–azimuthal average of particle fluid field
t_f	Friction/stopping time
St	Stokes number
Ri_r	Richardson number based on radial velocity
Ri_ϕ	Richardson number based on azimuthal velocity
$\mathrm{Ri}_{\phi,0}$	Midplane estimate for Ri_ϕ
Re	Reynolds number

2. Analytical and Numerical Model

The nascent planet-forming environment is a complex system containing gas with dust as the solid counterpart. Here we describe the analytical and numerical model we have used for this investigation. All the relevant parameters and variables, along with their definition are listed in Table 1. The formal modeling of such systems is generally formulated with the Euler's equation for the gaseous component, along with the solids treated as a pressureless fluid. The dynamics of the gas and the dust are coupled via a drag force experienced by the dust, arising from a headwind due to the pressure-supported gas that slightly reduces the radial velocity of the solids. The continuity and momentum conservation equations for the disk gas, in cylindrical coordinates $(\hat{R}, \hat{\phi}, \hat{z})$ with unit vector $\hat{\boldsymbol{r}} = R\hat{\boldsymbol{R}} + \phi\hat{\boldsymbol{\phi}} + z\hat{\boldsymbol{z}}$, can respectively be written as

$$\frac{\partial\rho_g}{\partial t} + \nabla\cdot(\rho_g\boldsymbol{U}_g) = 0, \tag{1}$$

$$\frac{\partial\boldsymbol{U}_g}{\partial t} + (\boldsymbol{U}_g\cdot\nabla)\boldsymbol{u}_g = -\Omega^2\hat{\boldsymbol{r}} + \frac{\rho_p}{\rho_g}\frac{\boldsymbol{U}_p - \boldsymbol{U}_g}{t_f} - \frac{1}{\rho_g}\nabla P, \tag{2}$$

where $\boldsymbol{U}_g$ and $\boldsymbol{U}_p$ are the total gas and particle velocities, respectively, P is the gas pressure; and $\Omega = \sqrt{GM_\star/R^3}$ is the local orbital frequency, with G and $M_\star$ being the universal gravitational constant and the stellar mass, respectively. With this, the local Keplerian velocity can be expressed as $V_k = R\Omega$. The corresponding equations for the particles treated as a fluid (hereafter we often refer to it as the particle fluid) read as

$$\frac{\partial\rho_p}{\partial t} + \nabla\cdot(\rho_p\boldsymbol{U}_p) = 0, \tag{3}$$

$$\frac{\partial\boldsymbol{U}_p}{\partial t} + (\boldsymbol{U}_p\cdot\nabla)\boldsymbol{U}_p = -\Omega^2\hat{\boldsymbol{r}} - \frac{\boldsymbol{U}_p - \boldsymbol{U}_g}{t_f}. \tag{4}$$

The second term on the right-hand side of each of Equations (2) and (4) represents the drag between the gas and the dust components, which is proportional to their relative velocities, normalized by t_f, a mechanical relaxation timescale also known as the friction time. Particles, being a pressureless fluid, move with the local Keplerian velocity $U_{p,\mathrm{K}} = R\Omega$, whereas the gas feels the radial pressure gradient, the ∇P term in Equation (2), which makes their motion slightly sub-Keplerian. The reduction in gas speed is quantified by the parameter η given by

$$\eta = -\frac{1}{2}h^2\frac{\partial\ln\rho_g}{\partial\ln R} = \frac{1}{2}\beta h > 0, \tag{5}$$

where $h = H_g/R$ is the disk aspect ratio and

$$\beta = -h\frac{\partial\ln\rho_g}{\partial\ln R}. \tag{6}$$

In modeling the system, the parameter β is often a representation of the global radial pressure gradient in the system. In systems such as described here, the ratio of the reduction in local Keplerian speed ηV_K and the sound speed c_s, a measure of the dynamical compressibility of the system, is designated by $\Pi = \eta V_K/c_s$. With Equations (5)–(6), Π can be expressed in terms of β as

$$\Pi = -\frac{1}{2}\beta. \tag{7}$$

In all our simulations, the value of Π is chosen as 0.05.

2.1. Numerical Setup

For numerical solutions of Equations (1)–(4), we use the PENCIL code,[8] which is sixth order in space and third order in time. The hydrodynamic equations are solved in a shearing-box setup (Goldreich & Lynden-Bell 1965; Umurhan & Regev 2004; Latter & Papaloizou 2017), which is a small box in the Cartesian coordinate system corotating with local Ω, corresponding to a distance R from the central star. The shearing-box approximation assumes that the radial (x) and the azimuthal (y) dimensions of the box (L_x, L_y) are small compared to R, whereas the vertical dimension (L_z) is not constrained by the shearing-box approximation. The unperturbed azimuthal gas velocity in the corotating frame can be written as $V_K = -q\Omega x$, where

$$q = -\frac{d\ln\Omega}{d\ln R}, \tag{8}$$

which is $-3/2$ for a Keplerian disk. Here q is the measure of the linear shear the simulation box is subjected to. We will

[8] http://pencil-code.nordita.org/

assume $q = -3/2$ throughout. With the shearing-box setup, we solve Equations (1)–(2) in the isothermal approximation with equation of state $P = \rho c_s^2$, with c_s being the local isothermal sound speed. We write the total velocity components as a sum of a perturbation field plus Keplerian flow, i.e., $\boldsymbol{U}_g = V_K\hat{\boldsymbol{y}} + \boldsymbol{u}_g$ and $\boldsymbol{U}_p = V_K\hat{\boldsymbol{y}} + \boldsymbol{u}_p$ for gas and particles (respectively), resulting in the form

$$\frac{\partial \rho_g}{\partial t} + \nabla \cdot (\rho_g \boldsymbol{u}_g) + V_K \frac{\partial \rho_g}{\partial y} = f_D(\rho_g, \boldsymbol{u}_g), \tag{9}$$

$$\frac{\partial \boldsymbol{u}_g}{\partial t} + (\boldsymbol{u}_g \cdot \nabla) + V_K \frac{\partial \boldsymbol{u}_g}{\partial y} = -c_s^2 \nabla \ln \rho_g + h\beta\Omega\hat{x} + \left(2\Omega v\hat{x} - \frac{1}{2}\Omega u\hat{y} - \Omega^2 z\hat{z}\right) + \frac{\rho_p}{\rho_g}\frac{\boldsymbol{u}_g - \boldsymbol{u}_p}{t_f} + f_\nu(\boldsymbol{u}_g, \rho_g). \tag{10}$$

The perturbation gas velocity and its respective Cartesian components are written with $\boldsymbol{u}_g \equiv (u_g, v_g, w_g)$, and similarly for the perturbation particle fluid velocity and its components as $\boldsymbol{u}_p \equiv (u_p, v_p, w_p)$. The third term on the left-hand side of Equation (10) is the advection of gas due to the shear. The terms in parentheses on the right-hand side denote the combined effects of the centrifugal force, Coriolis force, and stellar gravity. The pressure term of Equation (2) is decomposed into two components: a local and a global pressure gradient, represented by the first and second terms on the right-hand side of Equation (10). The local particle mass volume density is ρ_p. Note that the large-scale pressure gradient present in a typical protoplanetary disk is modeled as a constant forcing represented by the term $h\beta\Omega$ and is unresponsive to the gasdynamics.

In all the simulations, periodic and shear-periodic boundary conditions have been used in azimuthal and radial directions, respectively. In the vertical direction a reflective boundary condition has been used. It is important to remark here that Li et al. (2018) made a detailed study on the effect of different choices of vertical boundary conditions and found that the thickness of the dust layer changes with different choices. In particular, the thickness of the settled dust layer is smaller when a periodic boundary condition is used. In this work we have not explored the effects of the different setup and stick to the reflective one in all our simulations.

For these simulations we choose values of $h\beta$ such that in the absence of particles $u_g = w_g = 0$ and $v_g = -0.05c_s$ everywhere, indicating a weakly pressure-supported Keplerian steady state. Equations (9)–(10) are solved on an Eulerian grid (x_j, y_j, z_j). In order to stabilize the code in cases where steep gradients appear in the solutions, PENCIL uses sixth-order hyperviscosity and hyperdiffusivity, which are represented by f_D in Equation (9) and f_ν in Equation (10), respectively. These two terms allow the fields to dissipate their energy near the smallest scale while preserving the power spectra at the large scales. For more details on these schemes, the reader is referred to Appendix D.

The use of hyperdissipation over the normal (second-order) dissipation scheme greatly improves the bandwidth of the inertial range obtained from the simulations. In simulations with ∼2500 grids per H_g, a bandwidth of more than a decade is obtained using the hyperdissipation scheme (see Figure 16), which is impossible to obtain with a normal second-order viscosity prescription. However, even with this scheme, a considerable part of the simulation domain is lost in dissipation, with roughly one-third of the Nyquist frequency (corresponding to π/dx, where dx is grid size, i.e., a $2dx$ wave) not giving anything meaningful as far as the gas and particle dynamics are concerned. This issue is examined in more detail in Section 4.2.

The equations for the solid component are implemented in the form of Lagrangian superparticles (Johansen et al. 2007). The simulation box is seeded with $N_{\rm par}$ superparticles, each labeled by i, with position vector $\boldsymbol{x}_i \equiv (x_i, y_i, z_i)$ randomly chosen from a Gaussian distribution with scale height $H_{p,0}$. Each particle's corresponding perturbation velocity vector $\boldsymbol{u}_{pi}$ is similarly chosen to be random such that $|\boldsymbol{u}_{pi}| < 0.002c_s$. The evolution set Equations (3)–(4) for each solid's position and velocity are solved in the form

$$\frac{d\boldsymbol{x}_i}{dt} = -q\Omega x_i\hat{y} + \boldsymbol{u}_{pi} \tag{11}$$

and

$$\frac{d\boldsymbol{u}_{pi}}{dt} = \left(2\Omega v_{pi}\hat{x} - \frac{1}{2}\Omega u_{pi}\hat{y} - \Omega^2 z_i\hat{z}\right) - \frac{\boldsymbol{u}_g(x_i, y_i, z_i) - \boldsymbol{u}_{pi}}{t_f}. \tag{12}$$

For simulations with monodisperse solids, particles are chosen as a swarm of identical particles with a single Stokes number St and a predetermined disk metallicity Z, interacting with the gas collectively through the drag force. In order to achieve a smooth solution for the superparticle properties, a triangular-shaped cloud (TSC) scheme (Hockney & Eastwood 1981; Youdin & Johansen 2007) is adopted (see also the PENCIL code manual), which uses a second-order interpolation and assignment method, by a quadratic spline or quadratic polynomial. This scheme provides an interpolated estimate for $\boldsymbol{u}_g(x_i, y_i, z_i)$ based on the gas velocity values that are known on the fixed Eulerian grid set (x_j, y_j, z_j) (indexed by j) and given $\boldsymbol{x}_i$ and $\boldsymbol{u}_{pi}$, constructing an estimate for $\boldsymbol{u}_p$ on the Eulerian grid for ultimate use in Equation (10). For more details of this scheme, the reader is referred to Youdin & Johansen (2007, their Appendix A).

The properties of superparticles are determined based on the parameters used for the simulation box. The surface density Σ of the box, with a midplane gas density ρ_0, is $\sqrt{2\pi}\,\rho_0 H$, where $H = c_s/\Omega$ is the gas scale height. With this, the mean gas density in the box becomes $\rho_m = \Sigma/L_z$. The representative density of each superparticle thus reads as

$$\rho_{\rm par,swarm} = \frac{Z\rho_m}{N_{\rm par}/(N_x N_y N_z)}, \tag{13}$$

where $N_{\rm par}$ is the total number of superparticles introduced in the box with number of grids N_x, N_y, and N_z in the x-, y-, and z-directions, respectively. Similarly, the total mass represented by each is given by

$$m_{\rm par,swarm} = \frac{Z\rho_m V_{\rm box}}{N_{\rm par}}, \tag{14}$$

where $V_{\rm box} = L_x L_y L_z$ is the volume of the simulation box.

For post-analysis purposes, in order to construct an effective particle fluid velocity field on the gas fluid's Eulerian simulation grid, we do the following: (1) for each Eulerian grid cube with coordinate (x_j, y_j, z_j) and side Δ we find the set

Table 2
List of Simulations and Relevant Parameters

Simulation Name	Domain[a] $L_x \times L_y \times L_z$	$N_{\rm grid}$ $N_x \times N_y \times N_z$	$N_{\rm par}$	St	Z	$N_{\rm par}$/Grid
A2D-04H	$0.2 \times 0.2 \times 0.2$	$512 \times 1 \times 512$	2^{18}	0.04	0.01	1
A2D-04M	$0.2 \times 0.2 \times 0.2$	$1024 \times 1 \times 1024$	2^{20}	0.04	0.01	1
A2D-04SH	$0.2 \times 0.2 \times 0.2$	$2048 \times 1 \times 2048$	2^{22}	0.04	0.01	1
A2D-2H	$0.2 \times 0.2 \times 0.2$	$512 \times 1 \times 512$	2^{18}	0.2	0.01	1
A2D-2SH	$0.2 \times 0.2 \times 0.2$	$2048 \times 1 \times 2048$	2^{22}	0.2	0.01	1
B3D-04L	$0.2 \times 0.2 \times 0.2$	$128 \times 128 \times 128$	2^{21}	0.04	0.01	1
B3D-04M	$0.2 \times 0.2 \times 0.2$	$256 \times 256 \times 256$	2^{24}	0.04	0.01	1
B3D-2L	$0.2 \times 0.2 \times 0.2$	$128 \times 128 \times 128$	2^{21}	0.2	0.01	1
B3D-2M	$0.2 \times 0.2 \times 0.2$	$256 \times 256 \times 256$	2^{24}	0.2	0.01	1
B3D-2H	$0.2 \times 0.2 \times 0.2$	$512 \times 512 \times 512$	2^{24}	0.2	0.01	0.125
F3D-512[b]	$2\pi \times 2\pi \times 2\pi$	$512 \times 512 \times 512$	…	…	…	…

Notes. Simulation sets presented in this paper. The y-dimension in 3D axisymmetric runs is arbitrarily noted as 0.2.
[a] All lengths in units of H.
[b] 512^3 forced simulation used to identify useful subdomain.

of all particles $\{i\}$ that lie within the cube; (2) the total number of particles in the cube is added, and a value of $\rho_p(x_j, y_j, z_j)$ is assigned after multiplication by Equation (13); followed by (3) taking the average of all $\boldsymbol{u}_{pi}$ contained in the same grid box and assigning its value to the particle fluid's Eulerian velocity, i.e., $\boldsymbol{u}_p(x_j, y_j, z_j)$. A value of $\boldsymbol{u}_p = 0$, $\rho_p = 0$ is assigned when there are no particles in the grid box. As a matter of course, when there are two or more particles found within the grid box we calculate a standard deviation and assign it to the vector field $\delta\boldsymbol{u}_p$.

2.2. Initial Conditions and Simulation Sets

In all our simulations, the gas is assumed to follow the isothermal equation of state $P = \rho_g c_s^2$, where, in code units, we assign $c_s = 1$, $\rho_g = 1$, along with $\Omega = 1$. This choice of initial conditions translates to a gas scale height $H_g = c_s/\Omega = 1$.[9] The initial metallicity is assumed to be $Z = 0.01$, which sets the initial mass of the solids in the box. Given that the main objective of this work is a thorough investigation of the turbulence generation mechanism in the settled dust layer, we choose combinations of St and Z that are not expected to readily lead to SI in the simulations (see Carrera et al. 2015, for acceptable parameters leading to SI). For this work, we choose St = 0.04 and 0.2, values that are thought to lead to weak SI growth when combined with $Z = 0.01$, although, as mentioned earlier, there is uncertainty in this expectation (e.g., Li & Youdin 2021).

The size of the simulation box is set as $(L_x, L_y, L_z) \equiv (0.2, 0.2, 0.2)H_g$, and the initial positions of the superparticles are assigned randomly following a Gaussian distribution, constrained by a predetermined initial scale height $H_p = 0.1H_g$. For the 3D simulations, we choose resolutions of 128^3 (low) and 256^3 (moderate) for both the St values chosen. $N_{\rm par}$ is set accordingly in order to achieve one particle per grid. We also present a high-resolution simulation with 512 grid points in each direction for St = 0.2 with a lower number of particles to save computation time. In Table 2, we present the list of simulations along with the relevant parameters.

In terms of diagnostics, the evolving scale heights and velocity fields of the particles are calculated dynamically by the numerical code. In order to compute the scale height H_p of the particles representative of the full domain, the simulation box is divided into N_x slices in the radial direction. H_p is then calculated first for each individual slice following the rms of the particle vertical distances from the midplane,

$$H_{p,k} = \sqrt{\frac{1}{N_{{\rm par},k}} \sum |z_i - \langle z \rangle|^2}\,, \tag{15}$$

where $H_{p,k}$ is the scale height for the kth slice, z_i denotes the position of the superparticle i contained in that slice, $N_{{\rm par},k}$ is the total number of particles, and $\langle z \rangle$ is the average vertical position of all $N_{{\rm par},k}$ particles belonging to the kth slice. The final scale height H_p is calculated by taking the weighted average of all $H_{p,k}$ from Equation (15) over all 2D slices:

$$H_p = \frac{1}{N_x} \sum H_{p,k}. \tag{16}$$

3. Transition to Turbulent State

3.1. Stages of Development

Figure 1 summarizes several shared characteristic stages exhibited by simulations during their development over time. This sequence of phases is also generally typical of SI simulations reported in the literature. We describe the stages as (1) the *dust settling phase*, in which the settling and drifting dust generates strong velocity shears in both the gas and dusty components, particularly in the radial and perturbation azimuthal component velocity fields; (2) the *bounce*, out of which the fluid state is sufficiently dynamically unstable so that the midplane trajectory of the settling dust particles is reversed (at some time t_b) and the layer starts to thicken some; and (3) a particle-drift-driven shear-turbulent state in which the shear turbulence is maintained and a quasi-steady turbulent state emerges where the particle layer settles onto a corresponding

[9] However, despite these simplifications, we explicitly quote all quantities in terms of their physical units throughout this study.

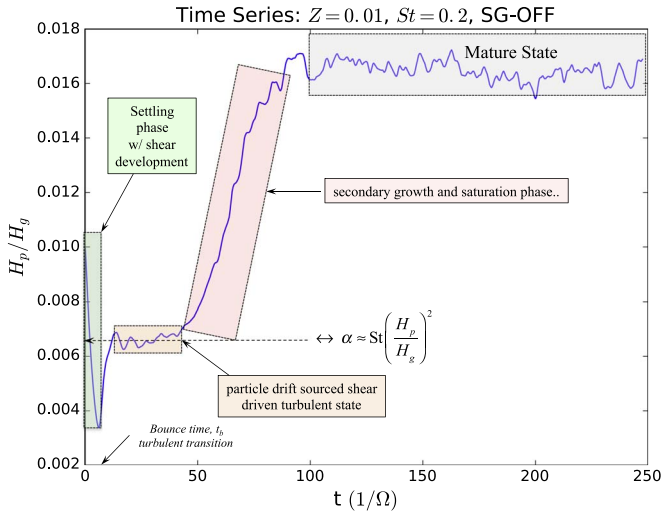

Figure 1. Time series of particle scale height for 3D simulation B3D-2L with $Z = 0.01$ and $\mathrm{St} = 0.2$. The various stages of development are labeled.

steady scale height from which we infer an effective measure of the turbulent state via $\alpha \approx \mathrm{St}(H_p/H)^2$ (e.g., a la Cuzzi et al. 1993; Dubrulle et al. 1995). All simulations reported here further exhibit some type of (4) *secondary growth phase*, followed by (5) a *drifting pattern state*. The last two stages may or may not be an instance of the SI. We further describe the details of these stages in what follows.

3.2. Spacetime Plots and Observed Pattern Drift

In Figures 2–3 we show the spacetime plots based on the low-resolution 128^3 simulations (B3D-04L, B3D-2L). As a function of radius x and time t, each figure displays (i) midplane azimuthal gas velocity, $\langle v_g \rangle_{y,0}$ averaged over y-direction; (ii) the midplane gas pressure perturbation per unit gas density, $\Pi'(x, t)$; (iii) the ratio of the azimuthally averaged midplane particle density, i.e., $\langle \rho_p \rangle_{y,0}$, to the midplane gas density, i.e., $\langle \rho_g \rangle_{y,0}$, where, in other words,

$$\epsilon_0(x, t) \equiv \frac{\langle \rho_p \rangle_{y,0}(x, t)}{\langle \rho_g \rangle_{y,0}(x, t)}; \tag{17}$$

and (iv) the azimuthally averaged metallicity, $\bar{Z}(x, t)$. Because the particle layers are close to the midplane, and given that the box sizes considered here are small, the gas densities throughout the domain are nearly constant. This allows us to replace $\langle \rho_g \rangle_{y,0}$ instead with the global average $\rho_{g,0}$. The exception is when we analyze a perturbation pressure quantity defined by

$$\Pi' \equiv c_s^2(\ln \langle \rho_g \rangle_{y,0}(x, t) - \ln \rho_{g,0}). \tag{18}$$

Inspection of Figures 2–3 readily shows that the density/pressure fluctuations are indeed weak, effectively rendering these dynamics nearly incompressible. The radial metallicity is defined as

$$\bar{Z}(x, t) \equiv \int_{-\infty}^{\infty} \langle \rho_p \rangle_y(x, z, t) dz \Big/ \sqrt{2\pi} H \rho_{g,0}, \tag{19}$$

where $\langle \rho_p \rangle_y$ is the azimuthally averaged particle density.

Figure 2 shows the development for $\mathrm{St} = 0.04$. The settling and bounce phase, which occurs within $t\Omega = 12$, is clearly evident in the ϵ_0 quantity (third panel). This initial stage is followed by a relatively long period of time ($t\Omega \sim 250$) in which the fluid appears to be in a turbulent state. By $t\Omega = 300$ the flow transitions into a symmetry-breaking patterned state, in which all quantities exhibit an outwardly propagating traveling wave with approximate wave speed $\approx 7 \times 10^{-3} c_s$ (solid black lines in Figure 2). The patterned state appears to fill 2.5 wavelengths on the simulation's radial domain. $\langle v_g \rangle_{y,0}$ also exhibits an inwardly propagating secondary pattern with a longer approximated pattern speed $\approx 4 \times 10^{-4} c_s$ (hatched black line in left panel of Figure 2). This same inwardly propagating pattern is also weakly visible in the $\bar{\Pi}'$ field, for which we also note its extremely low amplitudes, $< \mathcal{O}(10^{-4} c_s^2)$, which is consistent with the dynamics here being largely incompressible.

During the midplane shear turbulence phase, $\langle v_g \rangle_{y,0}$ shows weak fluctuations about a mean perturbation velocity $\approx -0.037 c_s$ (i.e., sub-Keplerian). After transition into the secondary nonlinear state, $\langle v_g \rangle_{y,0}$ increases its oscillation amplitude, exhibiting relatively steady fluctuations above this mean value, indicated by the red contours in the first panel of Figure 2, together with more pulsed fluctuations below this mean value, shown by the blue contours of the same. The weaker left-propagating pattern is only weakly visible in the midplane particle density and metallicity plot (right two panels of Figure 2). A close inspection of these two quantities at about $t\Omega = 570$ shows that there is an abrupt downshifting of the outwardly propagating pattern speed to $\approx 4 \times 10^{-3} c_s$, slightly more than 40% of what it was earlier (hatched magenta lines in the right panels of Figure 2). While the midplane particle densities hover between $1.1\rho_{g,0}$ and $1.2\rho_{g,0}$, after the transition into the patterned state $\langle \rho_p \rangle_{y,0}$ falls well below $\rho_{g,0}$, as the ratio ϵ_0 generally drops down into the $0.5 < \epsilon_0 < 0.8$ range. There are only narrow spatial extents where ϵ_0 only slightly exceeds 1. We also observe that the metallicity lies in the range $0.006 < Z < 0.014$.

Figure 3 shows the analogous evolution for $\mathrm{St} = 0.2$. The development sequence is similar to the $\mathrm{St} = 0.04$ case, with a settling/bounce phase ($t\Omega < 10$), followed by a turbulent state up to about $t\Omega \approx 40$, finally leading into a secondary nonlinear patterned state exhibiting about two wavelengths in the radial domain. However, here the pattern propagation in the secondary state is opposite to what it is in the $\mathrm{St} = 0.04$ case: $\langle v_g \rangle_{y,0}$ and $\bar{\Pi}'$ show inwardly propagating pattern speeds $\approx 1.7 \times 10^{-3} c_s$ (solid magenta lines in the left two panels of Figure 3), while correspondingly less discernible in the particle fields ϵ_0 and $\bar{Z}$ (hatched lines in the right two panels of Figure 3). During the bounce phase, $\langle v_g \rangle_{y,0}$ shows a strong burst (also examined further in the next section), followed by a slow growth of a period 2 nonpropagating pattern during the midplane turbulent phase (i.e., $10 \lessapprox t\Omega \lessapprox 40$). The transition into the patterned state becomes manifest ($t\Omega \approx 70$) with an amplitude variation in $\langle v_g \rangle_{y,0}$ about a nominal equilibrium value of around $\approx -0.04 c_s$, with extremes between $\pm 0.01 c_s$, painting the picture of an emergent jet flow.

Interestingly, $\bar{Z}$ appears to show a fast-moving radial streak pattern (solid black line in the far right panel of Figure 3) with a pattern speed $\approx 9 \times 10^{-3} c_s$. ϵ_0 shows a deep spike at the extreme bounce phase (with $\epsilon_0 \approx 2.7$) followed by settling into a quasi-steady turbulent value with $\epsilon_0 \approx 1.5$ before transitioning into the patterned state with a typical value of $\epsilon_0 \approx 0.8$. Aside from the possibly weak expression of the fast inward

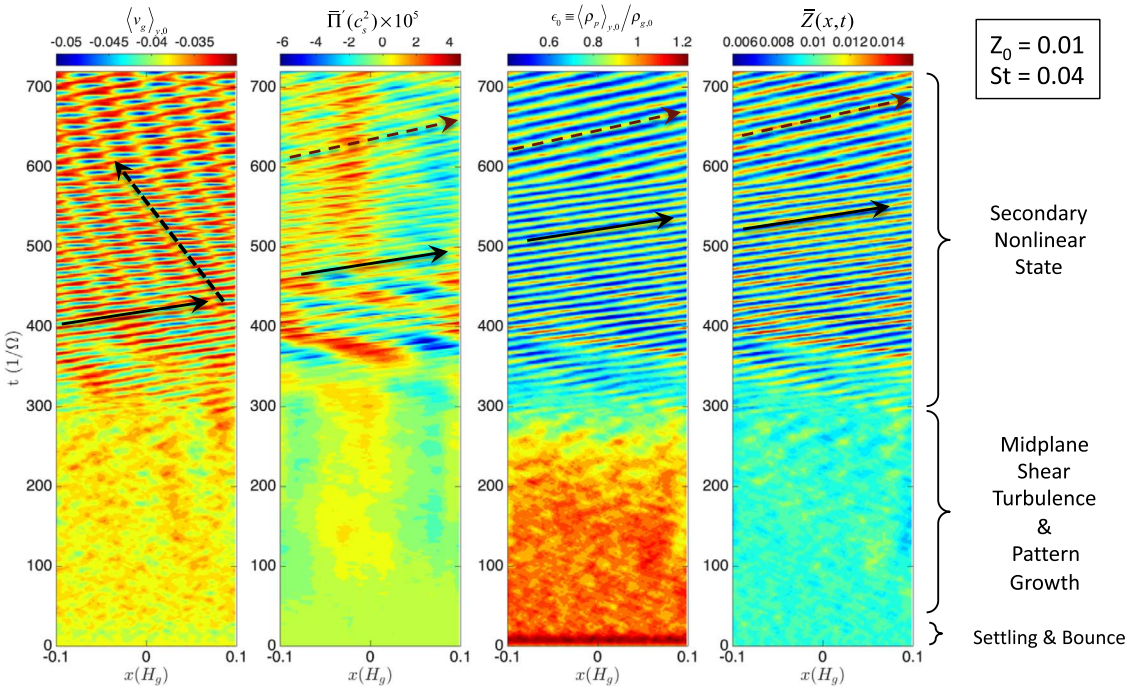

Figure 2. Composite figure showing spacetime diagrams for several quantities with St = 0.04 (simulation B3D-04L).

drifting pattern, the metallicity shows no particular organization, with its values remaining well in the range of 0.0075–1.2.

3.3. 3D Simulations

We now present several views of the simulation results and describe their notable characteristics. We focus our discussion on the early bounce phase and the shear-turbulent states of development.

3.3.1. St = 0.2

Figure 4 shows azimuthal and azimuthal–vertical averages of the three gas velocity components, $\langle u_g \rangle_y$, $\langle v_g \rangle_y$, $\langle w_g \rangle_y$ and $\langle u_g \rangle_{xy}$, $\langle v_g \rangle_{xy}$, $\langle w_g \rangle_{xy}$, respectively. The plot shows three time snapshots nominally representing the three stages of development shown in Figure 1. Each x-z slice shows with black dashed lines the corresponding averaged particle densities as a function of disk height, denoted by $\langle \rho_p \rangle_y$. The bounce phase is deepest at $t\Omega = 5$–6, where the emergence of a pair of counterflowing radial jets in u_g can be seen contained in two midplane symmetrically placed layers $0.005 < |z/H_g| < 0.02$. The positions of these jets are also highlighted in Figure 14 (the shaded region in the bottom left panel) in the context of a discussion on the Richardson's number of the system (see Section 3.5). Most importantly, the particle layer with $H_p = 0.003H_g$ is localized well away from the off-midplane jet layers. Moreover, the jet layers show signs of developing cat's eyes in u_g, indicating the ongoing emergence of a dominantly axisymmetric dynamic, which can also be seen in the azimuthally averaged w_g field. The quantity $\langle v_g \rangle_y$ exhibits a strong azimuthally directed jet mostly coinciding with the extent of the particle layer. v_g asymptotes to the predicted particle-free pressure-balanced limiting value ($\rightarrow -0.05c_s$) far from the particle layer.

Figures 5(a)–(b) display slices through the flow field at $t\Omega = 6$. The first of these displays the gas quantities as a function of radius at a nominal azimuthal position (here $y = -0.05H_g$). The vertical extent of the particle layer is well within $0.005H$ of the midplane (we note that for this snapshot $H_p \approx 0.003H_g$). The particle field is diffusely filamentary exhibiting outward-directed chevron patterning, which is also weakly apparent in the radial velocity u_g field in the same region. ρ_p typically falls in the values of $1\rho_g$–$3\rho_g$, with extreme events as high as $5\rho_g$. Away from the midplane u_g exhibits the strong counterflowing structure, together with the aforementioned signs of roll-up. The azimuthal velocity has an imprint of the activity seen in u_g in the counterflowing layers above the midplane. There is clear evidence of dynamical activity in the midplane layer as well, but its severity is muted in comparison to what manifests in the counterflowing layers.

Figure 5(b) shows an azimuthal slice at the radial position $x = 0$. The particle density field similarly displays filamentary chevron patterning directed toward the increasing azimuthal direction, conforming with the mean vertical structure of v_g, which is greater near the midplane than farther away. Figure 6 displays the azimuthal vorticity defined as

$$\omega_{y,g} \equiv \frac{\partial \langle u_g \rangle_y}{\partial z} - \frac{\partial \langle w_g \rangle_y}{\partial x}. \tag{20}$$

Overlaid are contours of constant azimuthally averaged particle density, once again depicting that those regions remain far away from the active layers above and below the midplane. The figure shows a radial–azimuthal planar plot of v_g vertically averaged across a layer containing the positive $\omega_{y,g}$ vorticity anomaly above the midplane, i.e., for $0.0055H_g \lessapprox z \lessapprox 0.0095H_g$. The imprint of the strong developing axisymmetric dynamic is evident with the emergence of zonal-flow-like structure with radial periodicity of $\sim 0.02H$. For the same layer the figure also shows an average of the particle velocity field exhibiting fluctuations with the same pattern. Similarly, the layer-restricted vertical average of w_g is shown with contours of

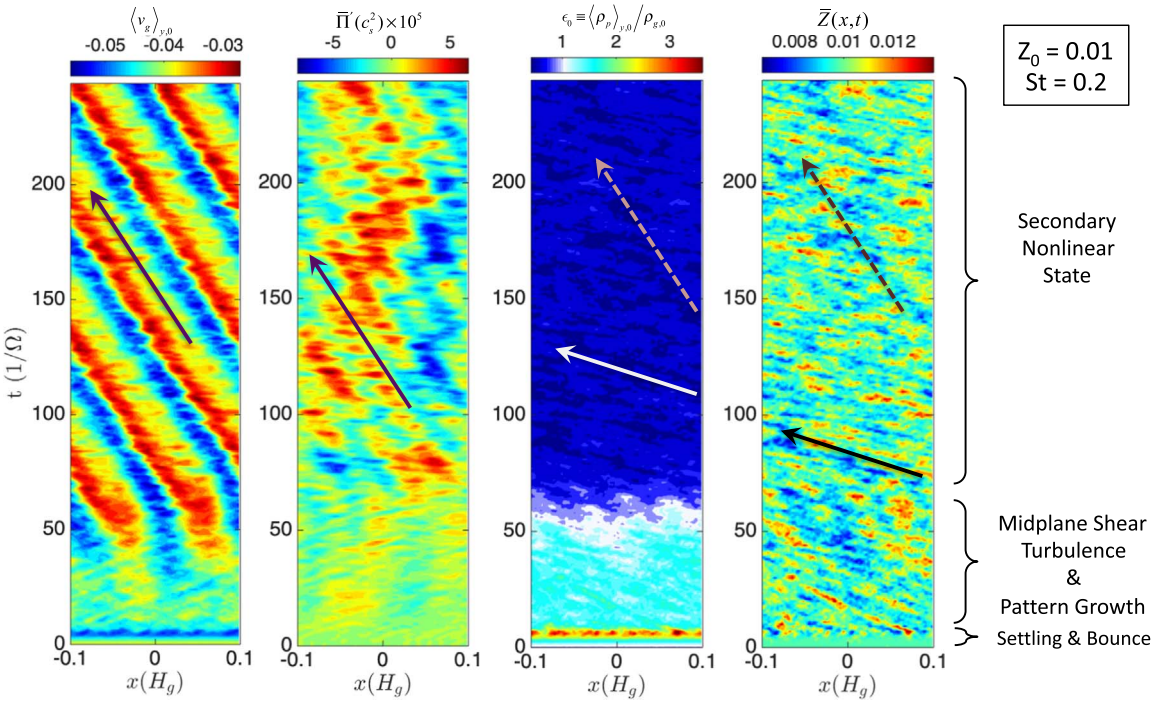

Figure 3. Same as Figure 2, except with St = 0.2 (simulation B3D-2L).

the vertical layer average of ρ_p, showing a strong correlation between positive vertical velocity and positive density anomaly, indicating that the emergent roll-up dynamics vertically advects the settled particle layer below.

In the shear-turbulent phase all quantities show the signs of turbulent motions, but with some retention of basic counter-flowing jet flow that led to instability. As the second column of Figure 4 shows ($t\Omega = 25$), the jet layer structure in $\langle u_g \rangle_y$ has fragmented while still retaining some discernible axisymmetric structure. Structure in $\langle u_g \rangle_y$ shows vertical spread (up to $\pm 0.05 H_g$). A similar vertical spread is also seen in $\langle \rho_p \rangle_{xy}$ (with $H_p \approx 0.05 H_g$). Midplane asymmetry has developed in $\langle u_g \rangle_{xy}$, but $\langle v_g \rangle_y$ remains largely intact, with clear evidence of the emergence of some organized axisymmetric structure near the midplane. The averaged vertical velocity field $\langle w_g \rangle_y$ has fragmented into small-scale structures that extend as far as those structures observed for $\langle u_g \rangle_y$.

However, the radial and azimuthal slices at this shear-turbulent stage, shown in Figures 5(c)–(d), tell a story that is lost if one focuses purely on the azimuthal averages. Figure 5(c) displays a large-scale radial sinusoidal pattern appearing in v_g, with wavelength about half of the box size. Imprinted on that pattern are small-scale unsteady turbulent motions. $\langle u_g \rangle_y$ also shows a pattern of strong positive value following the sinusoidal structure observed in v_g, with the regions in between interspersed with regions of negative velocity. Moreover, the spatial distribution of the particles appears restricted to $\pm 0.01H$ but now shows more dramatic filamentary structure with densities in places as large as $10\rho_g$. The filaments appear comparably oriented with the midplane as with the vertical. Figure 5(d), which depicts an azimuthal slice at the middle of the box $x = 0$, shows similar disordered turbulent quality imprinted on broad segregated zones of positive or negative mean values of u_g and v_g. Similarly, the azimuthal slice of ρ_p shows filamentary structure like that seen in the radial slice, with the only difference possibly being that the filaments are more aligned parallel with the midplane than with the vertical.

Figure 7 shows how $\omega_{y,g}$ is developing strong coherence conforming to the period 2 radial wave structure mentioned above. The particle layer, while still mainly contained around the midplane, also expresses the period 2 wave structure. Moreover, vertical averages of ρ_p and v_g across the same off-midplane layer discussed in Figure 6 show that the azimuthally aligned structures start to fragment with a tilt $\approx 45°$ from the upper left toward the lower right. In this orientation ρ_p shows wispy high-density structure that is reminiscent of filamentary density structures characteristic of simulations in which the SI is known to be operative (see, e.g., Figure 1 of Simon et al. 2017, and several others). The layer average of v_g exhibits a period 2 axisymmetrically banded zonal flow structure with similarly finely layered 45° oriented wisps seen in ρ_p. However, there does not appear to be any correlation between high-density filaments and the relative departures of v_g with respect to its layer mean: high-density filaments appear together with both high and low amplitude values of v_g; only the relative gross orientation of the finer-scale structures seems to correlate. A similar correlated pattern is seen between ρ_p and the layer average of w_g. Aside from streak orientation, there is even less correlation between high values of ρ_p and the corresponding layer average of $\omega_{z,g}$, where the gas vertical vorticity is defined as

$$\omega_{z,g} \equiv \frac{\partial v_g}{\partial x} - \frac{\partial u_g}{\partial y}. \tag{21}$$

Finally, in the secondary pattern state, the layer expresses a strong period 2 sinusoidal disturbance in all quantities. This midplane layer undulation phenomenon has been observed in several simulations in which the SI is the primary dynamical driver (e.g., Yang et al. 2017; Li et al. 2018; Yang et al. 2018; Gerbig et al. 2020, and others). The final column of Figure 4

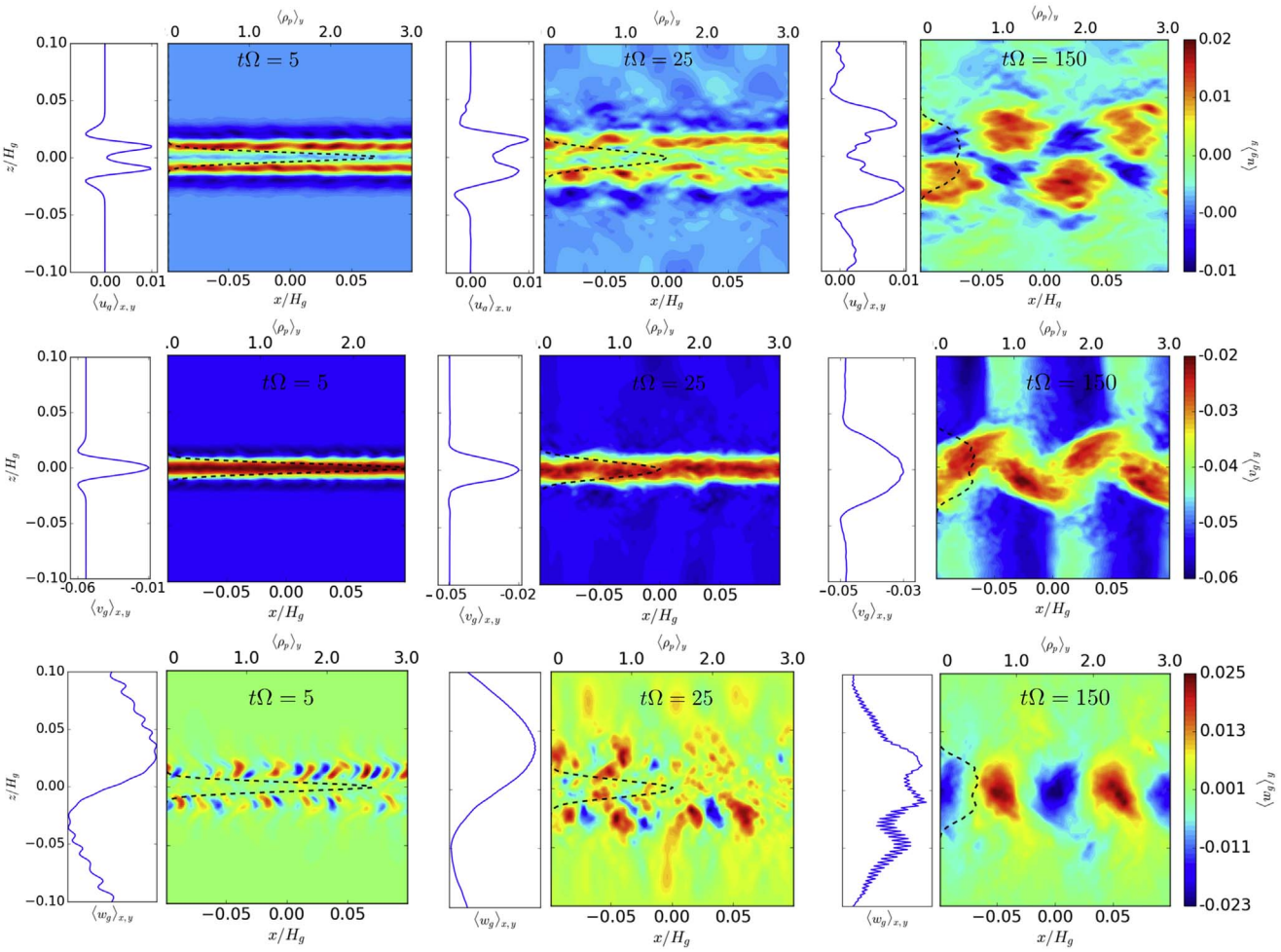

Figure 4. Flow structure development for the azimuthally averaged gas velocities by component: u_g (top row; $\langle u_g\rangle_y$), v_g (middle row; $\langle v_g\rangle_y$) and w_g (bottom row; $\langle w_g\rangle_y$). The figure shows the results for simulation B3D-2L with St = 0.2 at $t\Omega = 5$ (bounce state; left column), 25 (shear-driven turbulence state; middle column), and 150 (mature state; right column). Each figure has two components: the subpanels on the left show the combined azimuthally and radially averaged vertical profiles of the corresponding flow velocity components ($\langle u_g\rangle_{xy}, \langle v_g\rangle_{xy}, \langle w_g\rangle_{xy}$). The color plot in each case shows the azimuthally averaged velocity components in the simulation domain. The line plot, superimposed on the 2D color plot, with the axis on the top, shows the corresponding vertical profile of the solid density ($\langle\rho_p\rangle_y$) averaged over x and y.

most unambiguously illustrates this state of affairs. The interlaced but steadily disintegrating off-midplane configuration of $\langle u_g\rangle_y$ found during the shear turbulence phase has transitioned into a coherent midplane-crossing zigzagging oscillatory pattern. Interestingly, while $\langle v_g\rangle_y$ shows similar period 2 oscillatory character but where the near-midplane azimuthal jet profile now appears crenellated, far from the midplane the azimuthal gas velocity field shows an alternating vertically oriented radial pattern where the far field value of $\langle v_g\rangle_y$ now oscillates around its particle-free limiting value. Likewise, $\langle w_g\rangle_y$ shows radial oscillation, indicating that the particle layer is similarly sinusoidally undulating. This is borne out in the top panel of Figure 8, where the particle layer has entered into an organized sinusoidal configuration. A detailed examination of the nature of this stage is reserved for a future publication.

3.3.2. St = 0.04

Analogous to Figure 4, Figure 9 depicts azimuthally averaged flow fields during the three stages of development. During the early developing bounce phase (see the figure's first column), $\langle u_g\rangle_y$ develops a jet-like structure above and below the midplane just like for the St = 0.2 case, but its amplitude is weaker by a factor of 10 as $\langle u_g\rangle_{xy}$ clearly illustrates. There is no obvious development of Kelvin's cat's eyes unlike the St = 0.2 case. There is no discernible structure in $\langle v_g\rangle_y$ aside from weak perturbations atop the dominant midplane jet structure. Similarly, $\langle v_g\rangle_y$ shows perturbations that are of very small scale and amplitude and confined to within the layer containing the bulk of the particles, whose scale height is around $H_p \sim 0.01 H_g$.

Once again, the radial/azimuthal slice images (Figures 10(a)–(b)) demonstrate that in fact the layer is strongly active during the bounce phase. The radial slice of v_g shows that this layer is undergoing significant dynamical activity with the appearance of plumes up through to where the particle layer effectively terminates ($\sim 2.5 H_p$). The plumes' length scales are between $0.005 H_g$ and $0.01 H_g$. The u_g field shows activity restricted to within the dust layer, in contrast to the St = 0.2 case, where dynamics in u_g extends far beyond the dust layer. u_g also shows structure on the scale of the plumes, but whose horizontal scales are anywhere from 2 to 3 times the vertical scales. Structure in u_g also appears to be larger in size up past one to

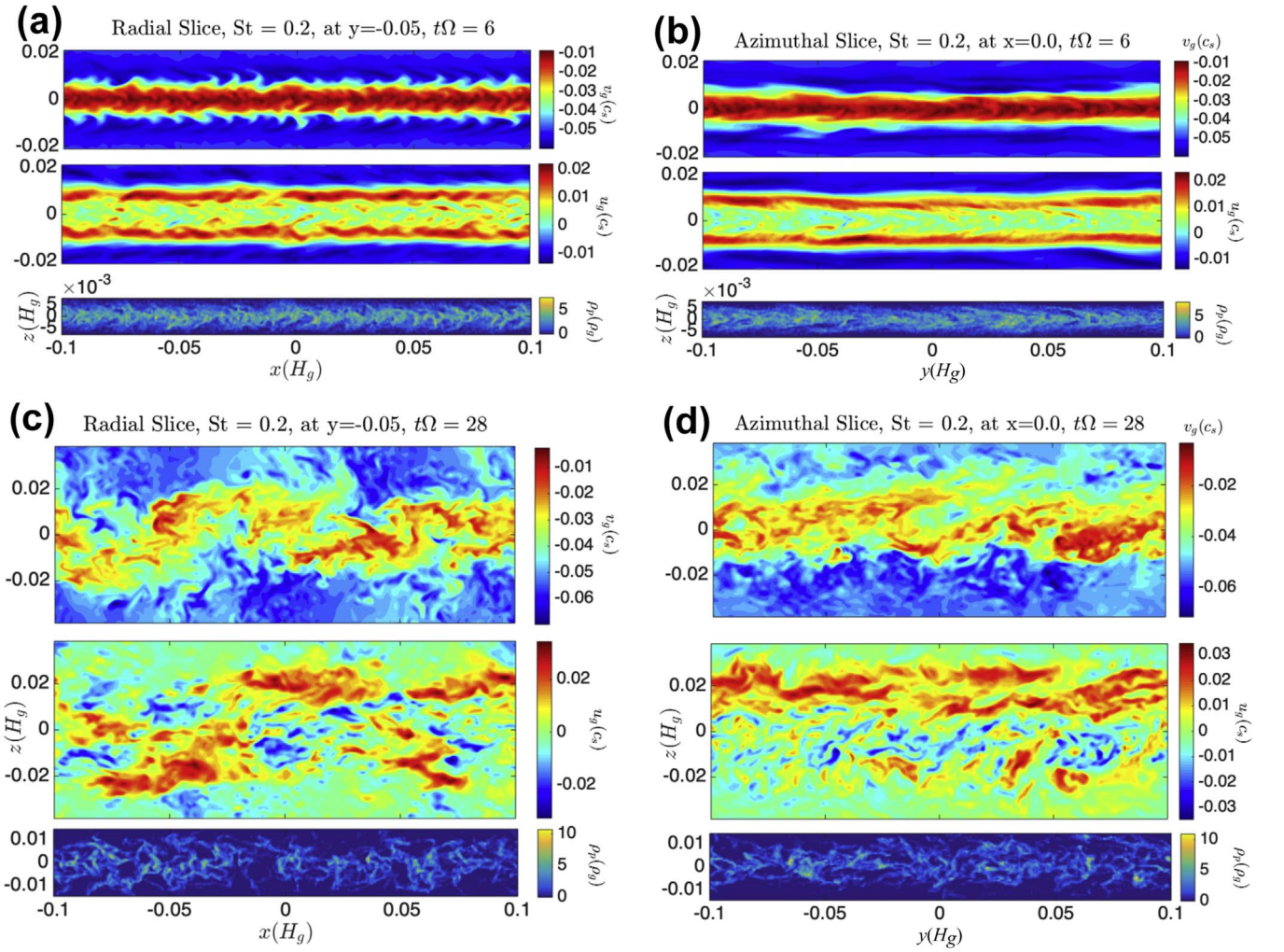

Figure 5. Four sets of flow visualizations as slices for St = 0.2 at two different times representing the early turbulence development (bounce) phase and the nominally shear-turbulent phase. Each set consists of three rows depicting u_g, u_g, and ρ_p, respectively: (a) radial slice at $y = -0.05H$ and $t\Omega = 6$, (b) an azimuthal slice at $x = 0$ and $t\Omega = 6$, (c) radial slice at $y = -0.05H$ and $t\Omega = 28$, and (d) azimuthal slice at $x = 0$ and $t\Omega = 28$. These depict the B3D-2M simulation set.

two particle scale heights and, moreover, shows no obvious organization like that seen during the bounce phase of St = 0.2 (see Figure 5(a)). The radial slice of ρ_p shows that the filaments are far more diffuse and seem to follow the textures seen in v_g; overall the ρ_p field is far more nondescript compared to the St = 0.2 case. The azimuthal slices shown in Figure 10(b) follow the general tenor of the qualities exhibited in the radial slice case, with perhaps the only real difference being that the v_g and u_g fields are slightly more azimuthally elongated, especially at heights about $1H_p$–$2H_p$ from the midplane.

For St = 0.04 the turbulence phase takes root by $t\Omega = 40$. The second column of Figure 9 shows that the weak jet structure that emerged during the bounce phase has fragmented somewhat and that its overall structure has significant asymmetries. The vertical extent of the particle layer has expanded some, and $\langle v_g \rangle_y$ is now showing signs of dynamical unsteadiness. The $\langle w_g \rangle_y$ also shows that there is a qualitative transition with structures growing in size and extending vertically across the domain, with the appearance of some amount of diffuse vertical alignment in the field.

Remarkably, the radial/azimuthal slices (Figures 10(c)–(d)) during this turbulent phase seem to show that the overall qualitative nature of the unsteady motions emerging during the bounce phase characterizes the turbulent flow as well. Aside from stretching its vertical extent a bit, the characters of v_g and u_g, in both of their azimuthal and radial slices, look very much like what they look like during the bounce phase: unsteady motions with plumes in v_g at $1H_p$–$2H_p$ distance from the midplane, with small-scale structures in u_g on similar scales. Perhaps the only significant difference is that filaments in ρ_p are somewhat finer, where higher values of ρ_p are achieved compared to the early development. Nonetheless, ρ_p is generally diffuse, especially when compared to the situation encountered in the corresponding St = 0.2 case (see the ρ_p fields of Figures 5(c)–(d)).

As the final column of Figure 9 shows, when the flow has fully transitioned into its secondary state ($t\Omega \gtrapprox 300$), the flow fields have transformed as well. A period 3 midplane symmetric pattern emerges in $\langle v_g \rangle_y$ up to the vertical extent of the particle layer whose $H_p \sim 0.015 H_g$. $\langle u_g \rangle_y$ develops into a vertical domain filled with organized structure of zigzagging contours that extends far away from where the particles are mostly concentrated: $\langle u_g \rangle_y$ exhibits an outward-pointing chevron pattern within the particle layer but then switches its orientation when moving away about $2H_p$–$3H_p$ from the midplane. It is also remarkable that the vertical gas velocity

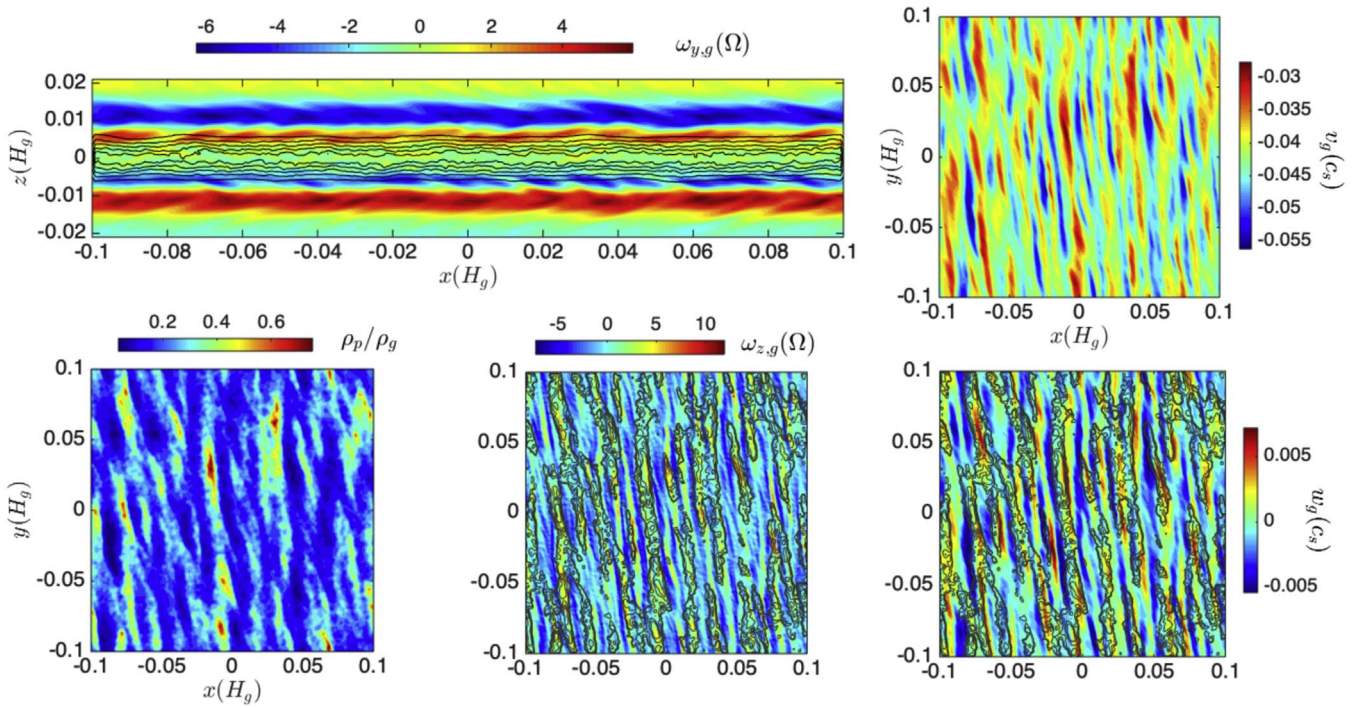

Figure 6. More flow visualization for St = 0.2 utilizing B3D-2M simulations at $t\Omega = 6$ (bounce phase). Top left: the azimuthal gas vorticity ($\omega_{y,g}$) formed from the azimuthally averaged gas velocities (see text). The off-midplane counterflowing jet layers ($0.005 < |z/H_g| < 0.015$) show the beginnings of dipolar vortex pair formation, with approximately 14–16 cat's eye pairs in evidence each above and below the midplane. Overlaid in black contours are corresponding isolevels of the azimuthally averaged ρ_p/ρ_g. As a function of radial and azimuthal coordinate, the top right panel shows the vertical average of v_g across a narrow layer in the range of $0.0055 \leqslant z/H_g \leqslant 0.0095$, corresponding to five grid points and nominally centered on the positive $\omega_{g,y}$ vorticity anomaly above the midplane (the red layer) of the top left panel. Bottom row: vertical averages across the same narrow layer for ρ_p/ρ_g (left), the vertical gas vorticity ($\omega_{z,g}$; middle), and the vertical gas velocity (right). Across the positive $\omega_{g,y}$ vorticity anomaly layer the average of ρ_p/ρ_g is ≈0.22. The last two panels show ρ_p/ρ_g in dark contour lines for values (0.22, 0.25, 0.4, 0.5), all denoting lines of density enhancement compared to the layer's mean. Positive w_g appears correlated with $\rho_p/\rho_g > 0.22$.

$\langle w_g \rangle_y$ field is nearly zero within the particle layer but then takes on a period 3 nearly vertically oriented alternating band structure away from the particle layer, as similarly observed by Li et al. (2018). The reasons for this curious feature are not clear. The bottom panel of Figure 8 shows $\omega_{y,g}$ overlaid with $\langle \rho_p \rangle_y$ contours demonstrating the emergence of a period 3 structure here as well. Finally, Figure 11 shows radial slices during the beginning of the late stage, and it is notable that the general turbulent character seen in the earlier stage, especially in the v_g, persists as the sinusoidal structure begins to set in.

3.4. A Comparison of 3D Axisymmetric Dynamics with Those Uncovered in Full 3D Flows

We consider a limited set of 3D axisymmetric simulations in an effort to gain some insight about the emergent turbulent dynamics reported in the previous subsection. We run these simulations specifically to examine how the transition from the bounce phase into the turbulent state takes shape. We are wary of running these axisymmetric simulations much farther than these early phases simply because secondary and tertiary transitions involving nonaxisymmetric mechanisms likely characterize the true descent into turbulence in the 3D simulations discussed so far. Thus, any of the interesting features that manifest in the axisymmetric case likely get washed away under the more realistic scenario. Despite this, some useful insights can be inferred. To be concrete with terminology, 3D axisymmetric means to refer to runs in which all three components of position and velocity are present but are only dependent on the radial and vertical coordinates. In contrast to this, hereafter we sometimes refer to the full 3D calculations as "unrestricted 3D."

Figure 12 shows the axisymmetric development of ρ_p, v_g, u_g for St = 0.04 in straight analogy with Figures 10(a) and (c) and 11. Remarkably, we find that the instability development bounce phase velocity fields v_g and u_g (i.e., $t\Omega = 6$; top three panels of Figure 12, simulation A2D-04H) look qualitatively identical to the radial flow slices of v_g and u_g *at every stage* of the corresponding full 3D simulation (simulation B3D-04M). Even during the emergent phase of the secondary state (see, e.g., top panel of Figure 11), while the layer exhibits a period 2–3 radial sinusoidal variation, the small-scale clearly turbulent dynamics exhibited by v_g are essentially the same as in the axisymmetric case. These trends suggest that the dynamics of the unrestricted 3D case are *not* primarily driven by KH roll-up in the azimuthal direction, as is commonly assumed to be the case; that instability in the St = 0.04 case is primarily an axisymmetric phenomenon. Moreover, the full 3D simulations also seem to evolve in a way that the flow fields look more like what they look like during its early turbulent phase, perhaps suggesting some type of self-regulation mechanism at work, in which the system is always sufficiently above—but not too far from—an instability threshold. Indeed, by comparison with the later time stamp illustration of the axisymmetric simulation ($t\Omega = 16$; bottom three panels of Figure 11), the dynamical zone has puffed out to higher levels in z with attendant appearances of wispy structures and ever-finer-scale vortex structure.

This direct comparison also shows that the particle densities tend to be higher in the axisymmetric simulations despite the

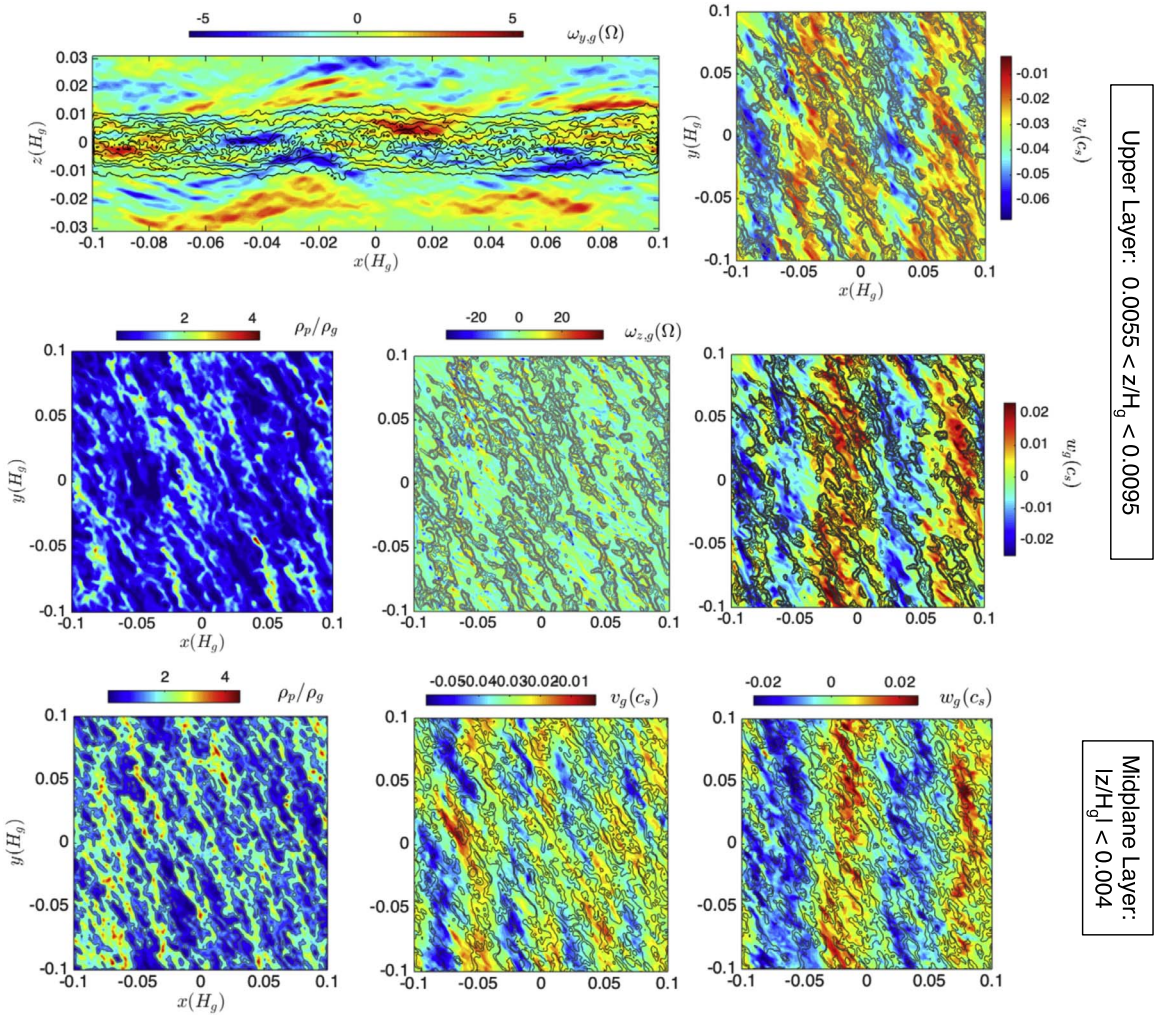

Figure 7. Similar to Figure 6, but at $t\Omega = 28$ (shear-turbulent phase). Top row: azimuthal average of $\omega_{y,g}$ (left) and vertical average of v_g (right) of the same off-midplane layer of Figure 6. Middle row: similar off-midplane layer averages of ρ_p/ρ_g (left), $\omega_{z,g}$ (middle), and w_g (right). The overlaid contours, ρ_p/ρ_g (0.81, 1, 1.25, 1.5, 2, 3), all represent enhancements in ρ_p/ρ_g over and above the layer average of 0.81. Note the appearance of broadly zonal flow in v_g exhibiting finer-scale wispy substructure that is found in other quantities. Bottom row: analogous midplane-centered averages ($|z/H_g| \leqslant 0.004$, $\leftrightarrow$ 9 grid points), ρ_p/ρ_g (left), v_g (middle), and w_g (right). Density contours are shown for $\rho_p/\rho_g = 1$ and 1.54 only, where the latter corresponds to the layer's mean.

fact that the flow field dynamics are similar to one another. The filaments developing in ρ_p are of finer scale and far more spindly compared to the filaments observed in the corresponding radial slices of ρ_p in Figures 10(a) and (c). Values of ρ_p/ρ_g within particle filaments can get as high as 8–10 in the axisymmetric case, while they rarely exceed values of 3–4 in corresponding full 3D simulations. In addition, filament sharpening and attendant void space growth in the axisymmetric case appear to intensify as the simulation evolves. Overall, this may be a consequence of a downscale forward enstrophy cascade occurring in the axisymmetric case, which should induce sharpening of filamentary structures. On the other hand, nonaxisymmetric motions will readily disrupt such coherent filament development. However, at this stage this remains a conjecture that should be investigated further. Nonetheless, these trends behoove exercising caution before interpreting the results of axisymmetric simulations as being applicable to full 3D scenarios.

Figure 13 shows the analogous axisymmetric development of St = 0.2 that ought to be compared against the results of the corresponding unrestricted 3D flow fields shown in Figures 5(a) and (c). During the early instability development phase ($t\Omega = 6$; top set of three panels of Figure 5, simulation A2D-2H), v_g shows the emergence of dramatic plumes directed away from the midplane and originating near where the particle layer ends. Signs of this can be seen in v_g for the full 3D simulation at about the same time (Figure 5(a)), although the plumes there appear to be somewhat muted in comparison, appearing more wispy. Unlike the unrestricted 3D case, u_g does not exhibit the same clear signs of emergent cat's eye structure within the off-midplane counterflowing jet layer for $0.005H_g \lessapprox |z| \lessapprox 0.015H_g$, although there are clear signs there of large-amplitude sinusoidal variation in u_g contours. Nevertheless, the midplane layers containing particles exhibit complex textural structure that is qualitatively similar to the emergent unstable dynamics seen in the St = 0.04 case, but to a far more muted extent.

In addition, similar to our concerns above, ρ_p is focused into filaments of stronger relief in the axisymmetric case than compared to what emerges in the full 3D simulations. The typical density count in the filaments emerging from the axisymmetric simulation is also nearly a factor of two larger than that in the corresponding full 3D simulation.

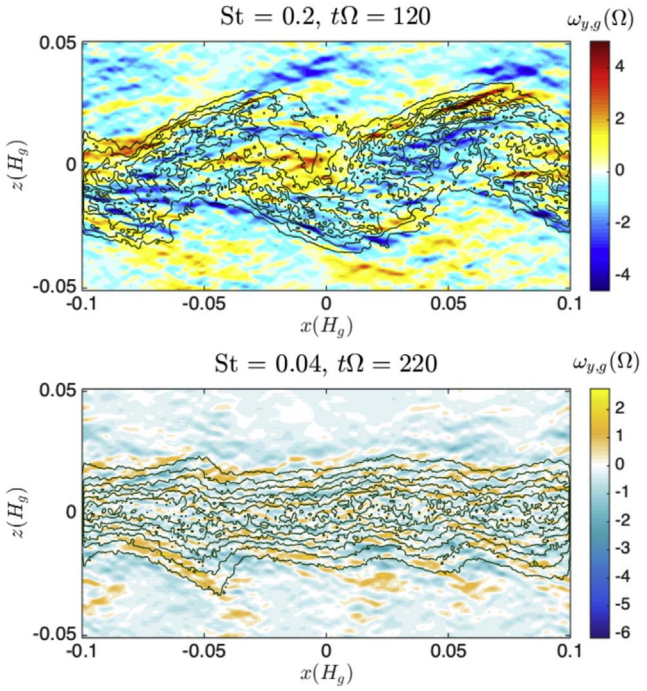

Figure 8. Radial slice depictions of $\omega_{y,g}$ and $\langle \rho_p \rangle_y$ during late-stage development after secondary transition. Top: St = 0.2 at $t\Omega = 120$ with contours on $\langle \rho_p \rangle_y$ ranging from 0 to $0.8\rho_{g,0}$ (simulation B3D-2M). Bottom: St = 0.04 at $t\Omega = 220$ with $\langle \rho_p \rangle_y$ contours ranging from 0 to $1.2\rho_{g,0}$ (simulation B3D-04M).

We observe that by the time the axisymmetric simulation is sufficiently past the bounce phase, the flow field structure that develops in both u_g and v_g ($t\Omega = 12$, Figure 13) diverges in quality from what normally develops in the full 3D case at similar times. In particular, several plume-like phenomena in v_g extend significantly away from the midplane with no accompanying particle filaments. For example, at $t\Omega = 12$ there is a pronounced plume−filament structure in v_g lying between $x = -0.05H_g$ and 0, and above the midplane between $z = 0.02H_g$ and $z = 0.04H_g$. Cross-referencing this structure against the map of ρ_p shows that there are no particles there. There are several other instances of this feature throughout the simulations studied. Conversely, there are also features in v_g that do correlate with enhanced particle locations as in the case of the dramatic, near-midplane, symmetrically oriented particle filament found in $0 \leqslant |z/H_g| \leqslant 0.02$ and $0 < x/H_g < 0.02$, which corresponds to a similarly shaped texture in v_g at the same location.

The situation becomes even more muddled when one attempts to find connections between particles and gas flow fields in the full 3D calculations, as no clear correspondences lend themselves to easy visual detection. This observation raises the question, how exactly do the particles influence the turbulent dynamics once the turbulence sets in?

3.5. Richardson Numbers

The Richardson number (in general denoted as "Ri") is the nondimensional quantity measuring the destabilizing role of shear against the stabilizing influence of buoyancy oscillations. In the protoplanetary disk settings considered here, it is assessed on the basis of a radially and azimuthally uniform but vertically varying mean velocity profile generically denoted here by $\mathcal{U}(z)$. While a formal effective Ri characterizing nonsteady particle-laden flows in accretion disks is not currently formulated, we adopt the following *effective* definition:

$$\mathrm{Ri} = \mathrm{Ri}_{\mathrm{eff}} \equiv -\frac{\Omega^2 z \rho_p}{\rho_g + \rho_p}\left(\frac{1}{\rho_p}\frac{\partial \rho_p}{\partial z}\right)\Bigg/\left(\frac{\partial \mathcal{U}}{\partial z}\right)^2, \tag{22}$$

as promoted by Sekiya (1998) and Chiang (2008). Implicit in this definition is the assumption that the particle layer is thin enough that the background gas density is unvarying over the vertical scales of interest, which is certainly the case here.

The Miles–Howard theorem states that a sufficient condition for the stability of a parallel stratified flow against infinitesimal perturbations is if $\mathrm{Ri} > 1/4$ everywhere within (Howard 1961; Miles 1961). If, on the other hand, there are locations/regions where $\mathrm{Ri} < 1/4$, then the flow is a candidate for *classic* stratified shear flow instability (e.g., Chandrasekhar 1961; Drazin & Reid 2004), which we generically refer to as the leading KH roll-up. We note that we consider here the classical criterion for KH roll-up and discuss further in Section 6.7 the effect strong rotation has on this criterion, especially in light of other previous studies (e.g., Gómez & Ostriker 2005; Barranco 2009).

There are several possible choices for $\mathcal{U}$ to use in the definition found in Equation (22) using the radial–azimuthal mean quantities introduced in Section 3.3. However, given recent single-fluid descriptions of particle-coupled disk gasdynamics (e.g., Lin & Youdin 2017), we also think it justified to consider calculating Ri in terms of center-of-mass velocities defined (respectively) for the radial and azimuthal component. As such, we motivate

$$U_{\mathrm{cm}} \equiv \frac{\rho_{g,0}\langle u_g\rangle_{xy} + \langle \rho_p\rangle_{xy}\langle u_p\rangle_{xy}}{\rho_{g,0} + \langle \rho_p\rangle_{xy}},$$
$$V_{\mathrm{cm}} \equiv \frac{\rho_{g,0}\langle v_g\rangle_{xy} + \langle \rho_p\rangle_{xy}\langle v_p\rangle_{xy}}{\rho_{g,0} + \langle \rho_p\rangle_{xy}}, \tag{23}$$

in which $\langle u_p\rangle_{xy}$ and $\langle v_p\rangle_{xy}$ are the radial–azimuthal averages of the particle fluid velocity fields based on their reconstruction described at the end of Section 2.1. Note also that in the above we use a constant value $\rho_{g,0}$ instead of an analogously defined radial–azimuthal gas mean $\langle \rho_g\rangle_y$ simply because the vertical box and particle extents are so close to the midplane that there is hardly vertical variation of the gas density, i.e., it can be easily shown that $\langle \rho_g\rangle_y \approx \rho_{g,0}$. We consider three instances of Ri, all evaluated based on the above center-of-mass velocities. For the first, denoted by Ri_ϕ, we follow the traditional approach in considering only the vertical variation of the azimuthal velocity component V_{cm}, i.e.,

$$\mathrm{Ri}_\phi \equiv -\frac{\Omega^2 z\langle \rho_p\rangle_{xy}}{\rho_{g,0} + \langle \rho_p\rangle_{xy}}\left(\frac{1}{\langle \rho_p\rangle_{xy}}\frac{\partial\langle \rho_p\rangle_{xy}}{\partial z}\right)\Bigg/\left(\frac{\partial V_{\mathrm{cm}}}{\partial z}\right)^2. \tag{24}$$

In the same vein, we consider an Ri defined on the vertical variation of the radial velocity component U_{cm},

$$\mathrm{Ri}_r \equiv -\frac{\Omega^2 z\langle \rho_p\rangle_{xy}}{\rho_{g,0} + \langle \rho_p\rangle_{xy}}\left(\frac{1}{\langle \rho_p\rangle_{xy}}\frac{\partial\langle \rho_p\rangle_{xy}}{\partial z}\right)\Bigg/\left(\frac{\partial U_{\mathrm{cm}}}{\partial z}\right)^2. \tag{25}$$

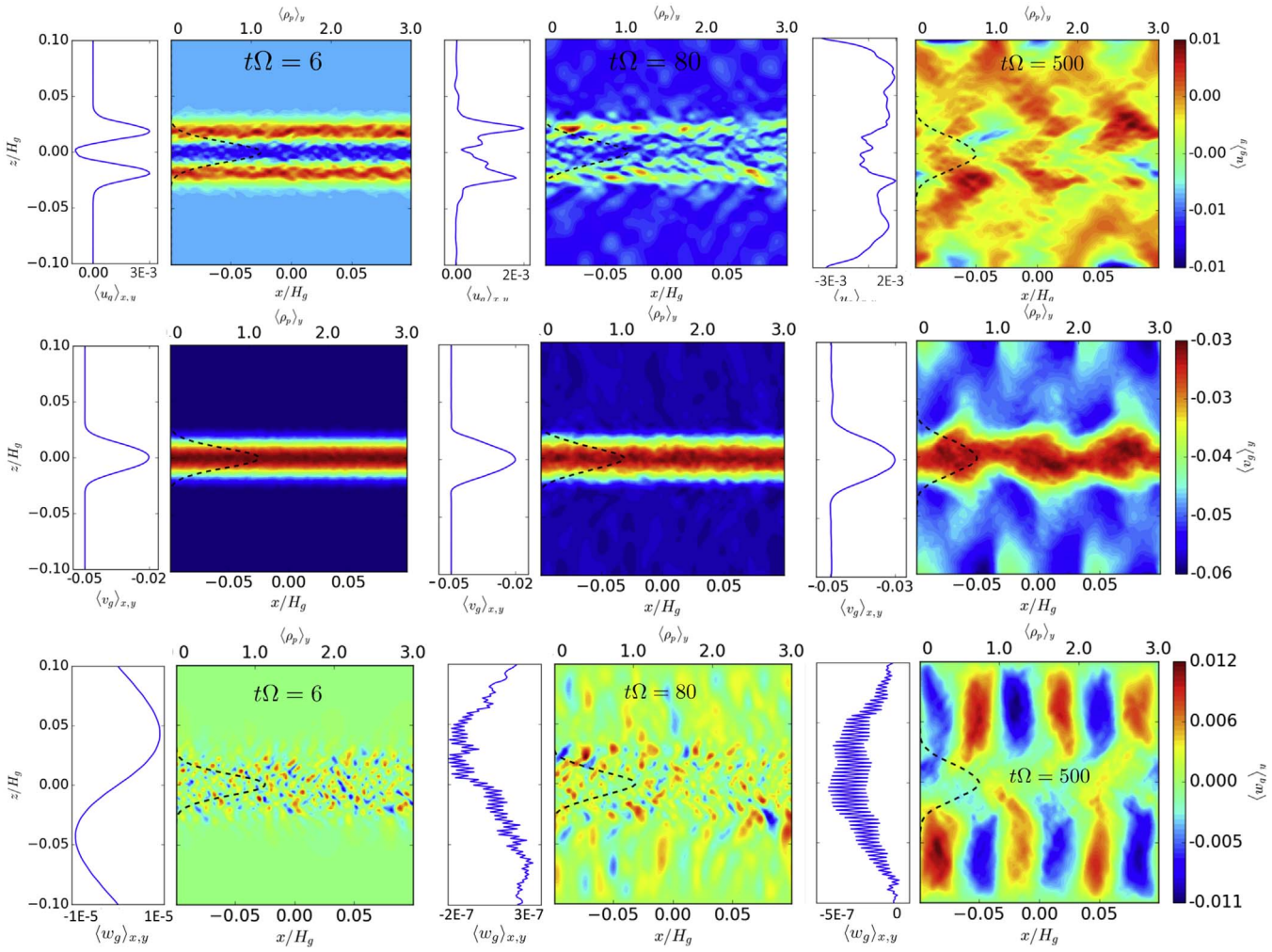

Figure 9. Representation of the development of velocity profiles, similar to Figure 4, for St = 0.04 (simulation B3D-04L): snapshots at $t\Omega = 6$ (bounce phase; left column), $t\Omega = 80$ (shear-driven turbulence phase; middle column), and $t\Omega = 500$ (mature state; right column). Note the period 3 banded structure in all three fields in the mature state.

For the final version, we adopt $\mathrm{Ri}_{\mathrm{eff}}$ as given in Equation (22), but with $\mathcal{U}$ replaced according to

$$\mathcal{U}^2 \rightarrow U_{\mathrm{cm}}^2 + V_{\mathrm{cm}}^2, \tag{26}$$

together with $\rho_p \rightarrow \langle \rho_p \rangle_{xy}$ and $\rho_g \rightarrow \rho_{g,0}$.

Ri_ϕ, with U_{cm} instead replaced by U_g, is the same definition used recently by Gerbig et al. (2020), as well as in several previous disk studies (Johansen et al. 2006; Barranco 2009; Lee et al. 2010a, 2010b; Hasegawa & Tsuribe 2014, to name a few). In this formulation Ri_ϕ has been used by previous studies to diagnose whether or not a vertically varying azimuthal profile is stable against nonaxisymmetric KH roll-up. Adopting Ri_r is analogously appropriate for axisymmetric KH roll-up scenarios like those considered in Ishitsu et al. (2009) and Lin (2021) and is appropriate for the solutions discussed here. Finally, the generalized form $\mathrm{Ri}_{\mathrm{eff}}$ is useful in assessing the shear stability of Ekman flows (e.g., Mkhinini et al. 2013).

In the spirit of Johansen et al. (2006), Figure 14 shows Ri plotted as a function of disk height at various turbulent development epochs for both the full 3D and axisymmetric simulations conducted here. As a reference we overlay the $\mathrm{Ri} = 0.25$ line in all the figures, keeping in mind that the actual critical Ri value for a disk setting that includes rotation may be different from the classical criterion (Gómez & Ostriker 2005; Barranco 2009). The top two rows of Figure 14 show the results for St = 0.04. The axisymmetric runs are shown up to the main bounce phase, and two main things are evident: first, the radial velocity fields do not satisfy the condition for KH roll-up, as Ri_r never gets near the critical value 0.25; and second, Ri_ϕ appears to hover about 0.25 and rise to nearly 1 at distances from the midplane both containing the particle layer and exhibiting turbulent dynamics (i.e., for $0 < |z/H_g| < 0.025$). By the time the axisymmetric simulation reaches its strongest turbulent transition point ($t\Omega \approx 6$) Ri_r remains mostly greater than 0.25—despite its large-amplitude fluctuations—over the bulk of the vertical extent except for a few grid points in the midplane region, while Ri_ϕ have smaller-amplitude fluctuations dropping occasionally below 0.25 across significant vertical stretches of domain. In any event, the axisymmetric simulations demonstrate that something other than KHI is operative here.

The situation is more stark in the full 3D case. In the lead-up to turbulent transition, and continuing well beyond it, Ri_r remains far above 0.25. Similarly, except for a very localized excursion below 0.25, Ri_ϕ essentially remains greater than the condition for radial KHI across the vertical extent of interest. Moreover, not only is $\mathrm{Ri}_\phi > 0.25$, but its value is also closer to

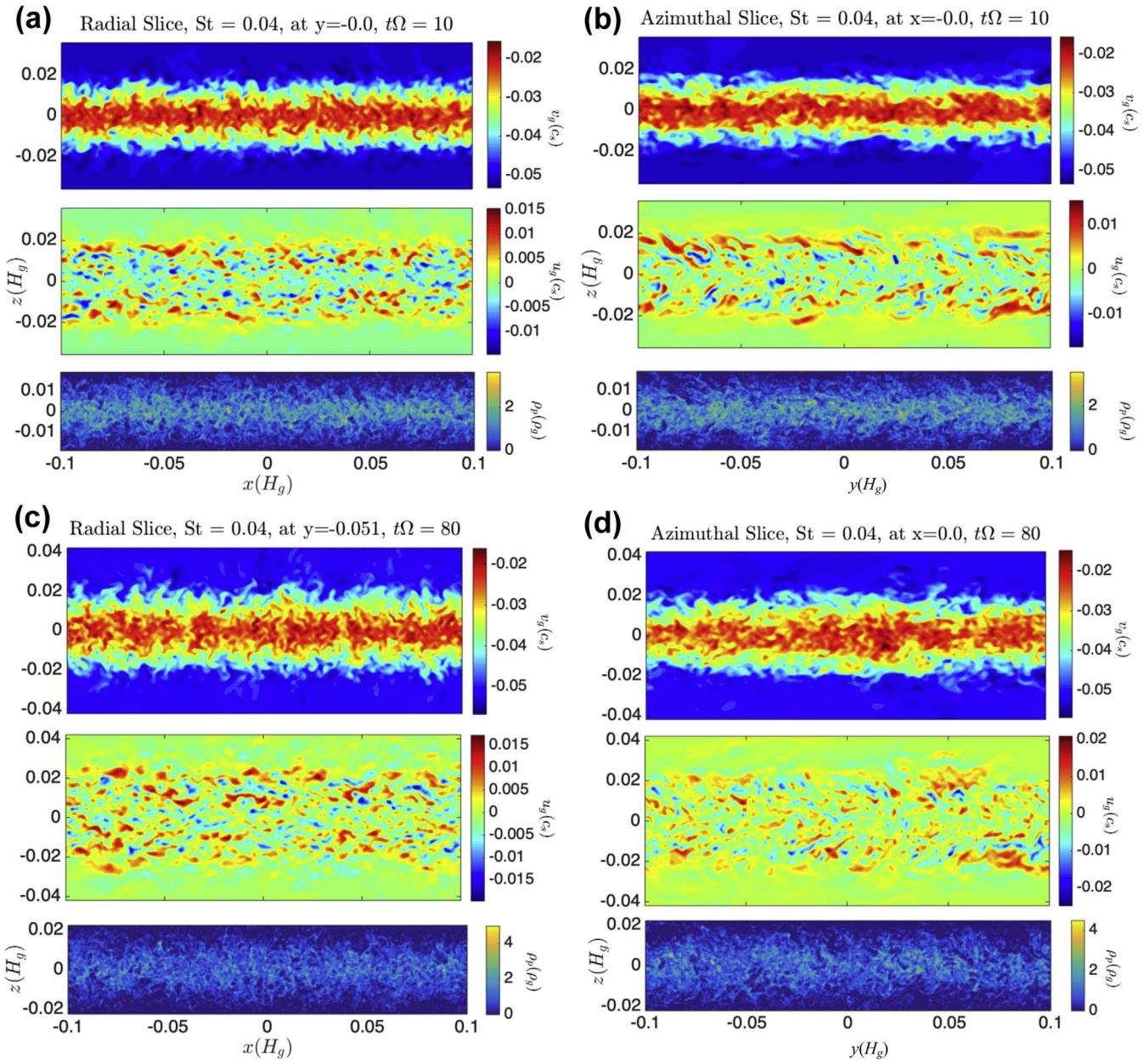

Figure 10. Flow visualizations analogous to Figure 5 except for St = 0.04: (a) radial slice at $y = -0.0H$ and $t\Omega = 10$, (b) an azimuthal slice at $x = 0$ and $t\Omega = 10$, (c) radial slice at $y = -0.05H$ and $t\Omega = 80$, and (d) azimuthal slice at $x = 0$ and $t\Omega = 80$. These depict the B3D-04M simulation results.

0.32 at transition over the vertical extent, only dropping close to 0.25 in specific locations of narrow vertical extent—e.g., near $z/H_g \approx \pm 0.02$ for $t\Omega = 6$, and a bit higher up for $t\Omega = 52$. When the simulation is well within its turbulent phase, Ri_ϕ near the midplane gets even larger, increasing beyond 0.4 over the bulk of the layer. This includes the midplane, although, once again, Ri_ϕ hovers near but always above 0.25 even with the most extreme cases (e.g., near $|z| \sim 0.25H_g$ at $t\Omega = 52$). Once the simulation has transitioned into its secondary pattern state, Ri_ϕ is everywhere far removed from 0.25 but lies primarily under 1 for the bulk of the turbulent layer with the exception of regions near the midplane ($|z/H_g| < 0.005$ at $t\Omega = 500$), where $\mathrm{Ri}_\phi > 1$ in fact. These features strongly indicate that the classical nonrotating KHI—as either radial or azimuthal roll-up—does not play the primary role in the development or maintenance of turbulent motions in these simulations where St = 0.04. It his possible, however, that a rotationally modified form of KHI is operating based on a previous linear study (Barranco 2009; see also discussion in Section 6.7).

The bottom two rows of Figure 14 show Ri for St = 0.2. In both full 3D and axisymmetric cases we see that by the time the simulations reach their deep bounce phase ($t\Omega = 6$) Ri_ϕ dips below 0.25 across the full vertical extent containing particles. At this time marker $H_p \approx 0.003H_g$, so that the particle layer is mostly confined to $|z/H_g| < 0.01$ (see, e.g., top left panel of Figure 6). By reference we see that the value of Ri_ϕ lurks around 0.034 up to $z \approx \pm 0.01H$, beyond which it precipitously drops in magnitude. Except for short-ranged dips below 0.25 (e.g., near $z \approx \pm\, 0.06H_g$), Ri_r mainly remains above 0.25 up to about $z \approx \pm\, 0.01H_g$ before similarly dropping precipitously in magnitude like Ri_ϕ. The dynamically developing off-midplane jet flow layers, with their incipient cat's eye formations,

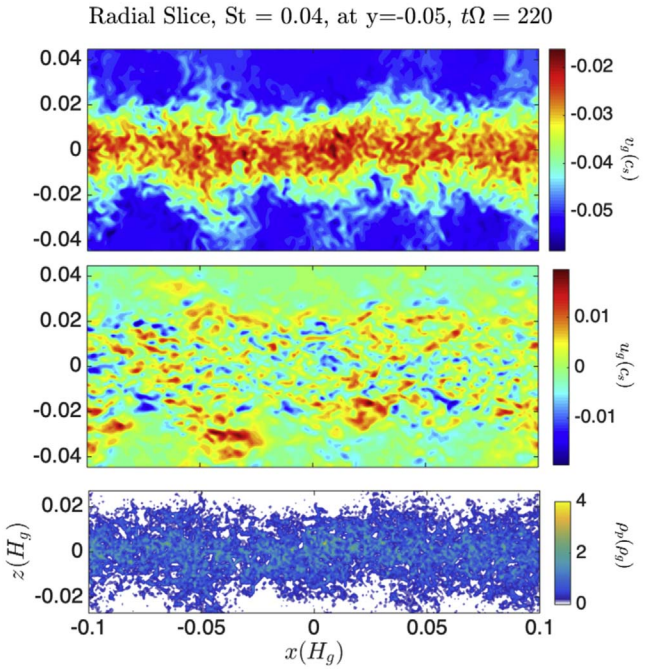

Figure 11. Radial flow slices for St = 0.04, $t\Omega = 220$. These depict the B3D-04M simulation results.

coincide to where both Ri numbers drop in magnitude for $|z/H_g| > 0.01$. We therefore conclude that these layers really are undergoing KH roll-up dynamics. However, within the particle-containing midplane layer the situation is different, as the Ri_r values there remain significantly above the criterion for radial KHI. On the other hand, Ri_ϕ does remain below 0.25, suggesting that this part of the layer is susceptible to azimuthally directed KH roll-up—although evidence for such formation is hard to discern from the snapshots shown for this case (see, e.g., Figure 5(c)). However, we also cannot rule out the possibility that this part of the midplane is not also subject to the same non-KHI unstable dynamics characterizing the turbulent dynamics in the St = 0.04 case discussed above.

By the time the system has moved well into the midplane turbulent phase, the situation for Ri has changed. We focus here only on the full 3D calculation by referring to the bottom middle panel of Figure 14, corresponding to the time stamp $t\Omega = 28$. It is evident that $\mathrm{Ri}_r > 1/4$ across that part of the midplane containing most of the particles, and only when $|z/H_g| > 0.02$ does Ri_r cross below 1/4, indicating that the layer gets even more stable against radial KH roll-up as the system evolves. Ri_ϕ also remains above 1/4 and largely below 1 across the particle-containing part of the midplane, but it drops well below 1/4 once $|z/H_g|$ exceeds 0.0125, suggesting that these upper layers may themselves be undergoing azimuthal KH roll-up. By the time the system has transitioned into its secondary pattern state (see, e.g., bottom right panel of Figure 14, for $t\Omega = 160$), except possibly for a narrow range near the midplane, the simulation appears stable against both radial and azimuthal KH roll-up across fully half of its vertical domain. Of course, this situation corresponds to the emergence of the heretofore-discussed radial sinusoidal period 2 feature in all fields.

In all panels of Figure 14 we plot an estimated "effective" midplane value for Ri_ϕ, denoted hereafter by $\mathrm{Ri}_{\phi,0}$. The aim here is to develop a relatively smooth estimate derived from the

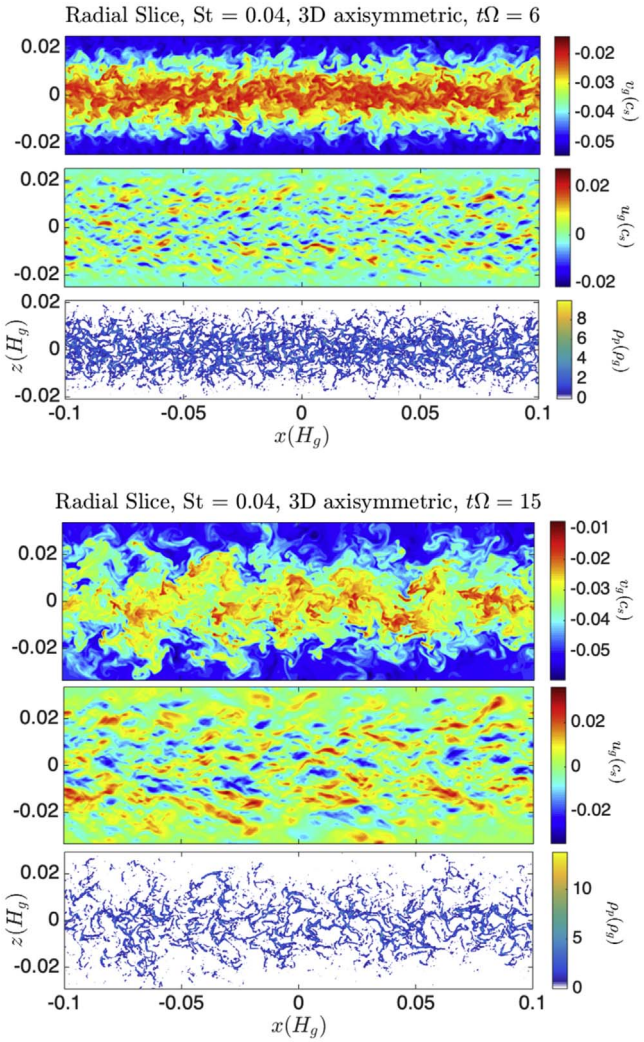

Figure 12. Flow slices like in Figure 10, except for 3D axisymmetric simulations with St = 0.04 (simulation A2D-04H). Top set of three panels: $t\Omega = 6$; bottom set of three panels: $t\Omega = 15$.

simulation output in the region primarily containing the bulk of the particles. Toward this end we assume a Gaussian-like model for $\langle \rho_p \rangle_{xy}$,

$$\langle \rho_p \rangle_{xy} \approx \rho_{p,\mathrm{mod}} \equiv \delta\rho_{p,0} \exp\left(-\frac{1}{2}\frac{z^2}{H_p^2}\right), \tag{27}$$

and determine the values of the parameters $\delta\rho_{p,0}$ and H_p using standard error minimization techniques (e.g., Nimmo et al. 2017). We note that the values determined for H_p via this approach basically agree with the values calculated for H_p according to the prescription described by Equations (15)–(16) found at the end of Section 2.2.

We similarly adopt a Gaussian-like form for V_{cm}, in which

$$V_{\mathrm{cm}} \approx V_{\mathrm{cm,mod}} \equiv v_{\mathrm{cm},\infty} + \delta v_{00} \exp\left(-\frac{1}{2}\frac{z^2}{H_s^2}\right), \tag{28}$$

where $v_{\mathrm{cm},\infty} = -0.05 c_s$ is the expected asymptotic value far away from the particle layer. The fit parameters δv_{00} and H_s are also determined via error minimization over a vertical domain

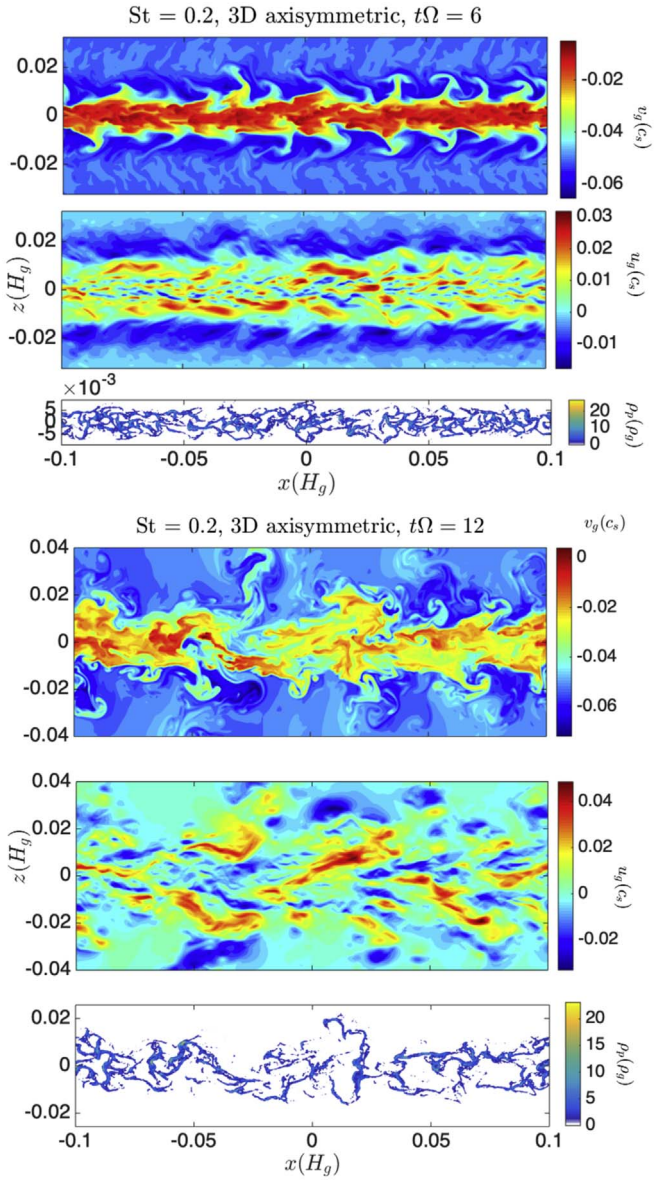

Figure 13. Flow slices like in Figure 5, except for 3D axisymmetric simulations with St = 0.2 (simulation A2D-2H). Top set of three panels: $t\Omega = 6$; bottom set of three panels: $t\Omega = 12$. Note the emergence of strong dipolar vorticity plumes in v_g for $t\Omega = 6$.

of up to $2.5H_p$, the aim being to best represent the vertical variation of $V_{\rm cm}$ over the bulk of the particle layer. Figure 15 shows an example of this approximate fitted form for simulation B3D-04M during its early bounce phase. We find that this approximate form is satisfactory for our purposes hereafter.

With these parameters determined, we insert the model forms Equations (28)–(27) into the definition of Ri_ϕ found in Equation (24), followed by evaluating the resulting expression at $z = 0$, i.e.,

$$\mathrm{Ri}_{\phi,0} \equiv \mathrm{Ri}_\phi(z=0) = \frac{\epsilon_0}{1+\epsilon_0}\frac{\Omega^2 H_s^4}{\delta v_{00}^2 H_p^2}, \quad \epsilon_0 \equiv \frac{\delta\rho_{p,0}}{\rho_{g,0}}. \tag{29}$$

In Table 3 we summarize the determined fit parameters, together with the estimated value of $\mathrm{Ri}_{\phi,0}$ for each of the simulations and their time stamps shown in Figure 14. $\mathrm{Ri}_{\phi,0}$ is shown in each plot as well.

We note two features. First, we find that the H_s is generally always larger than H_p by up to a factor of 2 or more, which is an unexpected trend. Second, the value of $\mathrm{Ri}_{\phi,0}$ appears to well characterize the behavior of Ri_ϕ in the St = 0.04 simulations through the bounce and early turbulent phases. This approximation to Ri_ϕ fails to capture its character for full 3D simulations that are in the secondary transition phase. Similar performance is seen in the St = 0.2 simulations, although it captures the essence of an averaged value across the particle layer in the primary turbulent phase (e.g., for the $t\Omega = 28$ time stamp shown). This leads us to conclude that during these late stages the simulations for St = 0.2 have undergone a significant transition in character. Despite its limitation, this type of model representation should prove useful in ascertaining the transition to turbulence, especially for cases where St = 0.04, as elucidated further in Section 5.2.

4. Turbulence and Statistics

4.1. Energy Formulation

It is informative to consider energy balances within the simulated dynamics. Since the gas component dynamics are largely incompressible, we adopt Equation (10) together with the incompressibility statement

$$\partial_i u_{gi} = 0, \tag{30}$$

in place of mass continuity, Equation (9). We designate u_{gi} to be the components of the gas velocity and u_{pi} to be the same for the particle velocities.[10] This means that the pressure term in the gas momentum equation is replaced with a diagnostic field P; thus, the equation, with the assumption of Einstein's summation convention, can be rewritten as

$$\begin{aligned}&\partial_t \rho_g u_{gi} + \partial_j \rho_g u_{gi} u_{gj} + V_K \partial_y \rho_g u_{gi} \\ &- 2\Omega\rho_g u_{g2}\delta_{i1} + (\Omega/2)\rho_g u_{g1}\delta_{i2} = -\partial_i p - \overline{P}_r \delta_{i1} \\ &- \Omega_0^2 \rho_g z \delta_{i3} - \Omega_0 \rho_p (u_{gi} - u_{pi})/\mathrm{St} + D_i(u_{gi}),\end{aligned} \tag{31}$$

in which δ_{ij} is the Kronecker delta symbol, $D_i(u_{gi})$ is a viscous dissipation function, and $\overline{P}_r$ is the mean radial pressure gradient. We are reminded that in these simulations u_{gi} and u_{pi} are deviations atop the base Keplerian flow V_K. In this vein, we identify the total velocities in each fluid component with $U_{gi} = u_{gi} + \delta_{i2} V_K$ and $U_{pi} = u_{pi} + \delta_{i2} V_K$, respectively, for the gas and particle components.

With respect to the energy measures considered in this section, we use the shorthand $\langle \bullet \rangle \leftrightarrow \int_V [\bullet]\, dV$ to denote volume integrals. In our domain the volume V will be over the computational domain L_x, L_y, L_z. We define the volume-integrated perturbation gas kinetic energy by

$$\varepsilon_g \equiv \left\langle \frac{1}{2}\rho_g u_{gi} u_{gi} \right\rangle, \tag{32}$$

[10] In this section we adopt Einstein notation with the usual convention of summing over repeated dummy indices i, j, where $i, j = 1, 2, 3$ reference the x, y, z components, respectively. Thus, i, j here ought not be confused with particle label i or grid label j used in Section 2.1.

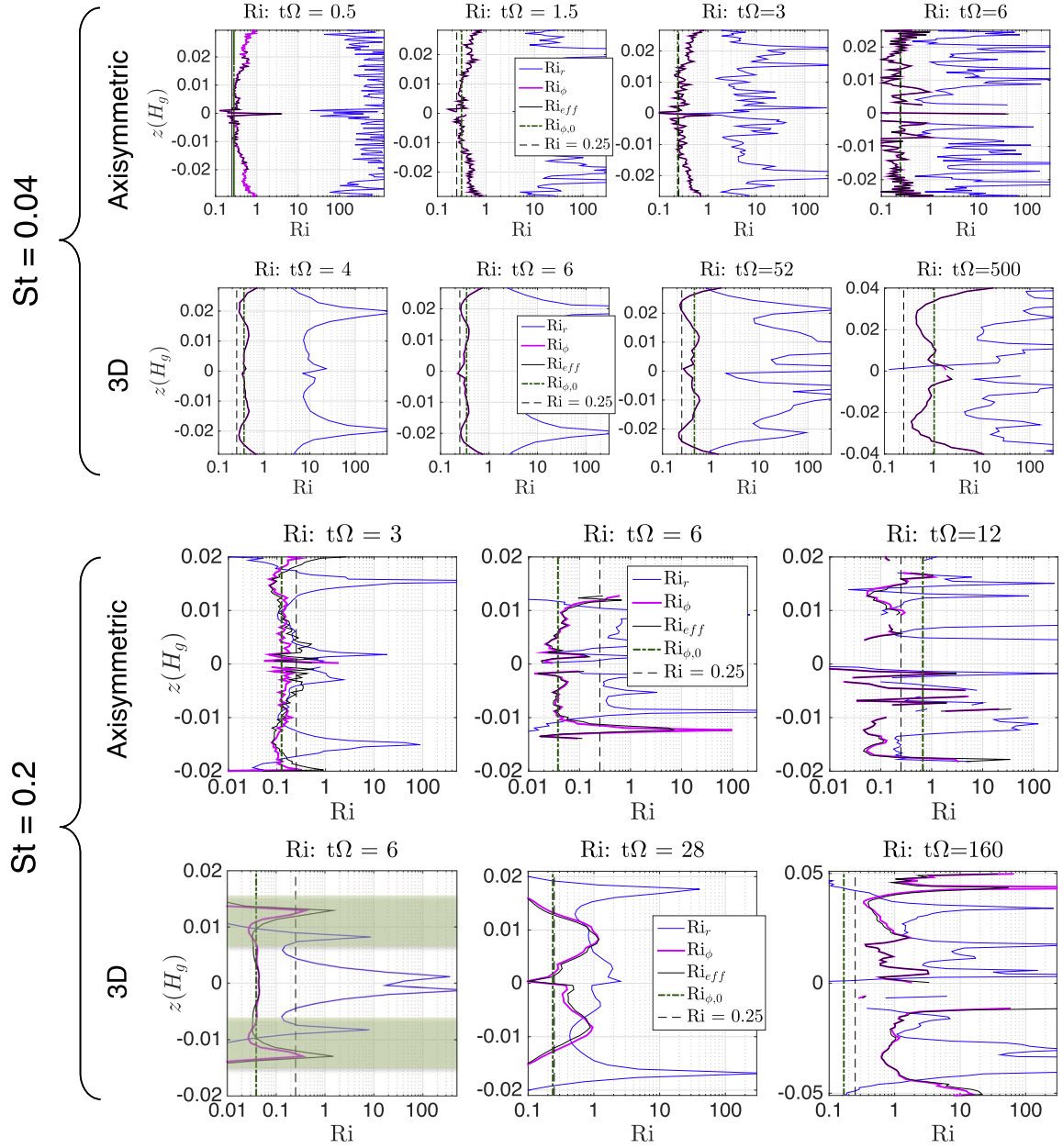

Figure 14. Richardson number plots. See text for details. The shaded region in the bottom left panel coincides with the location of the jets that appeared in Figure 4 for $t\Omega = 5$.

and similarly, the volume-integrated perturbation particle kinetic energy

$$\varepsilon_p \equiv \left\langle \frac{1}{2}\rho_p u_{pi} u_{pi} \right\rangle, \tag{33}$$

4.2. Energy Spectra

The energy integral formulation is oftentimes rewritten in Fourier space. With $\boldsymbol{k}$ being the 3D wavenumber and $k \equiv |\boldsymbol{k}|$ its absolute magnitude, it is customary to define a kinetic energy density per unit wavenumber as $\varepsilon_{k,g}$, which here is taken to be the total perturbation kinetic energy contained in all wavevectors $\boldsymbol{k}$ whose (absolute) wavenumbers lie in between k and $k + dk$. Defining $\tilde{u}_{gi}$ to be the Fourier transform of u_{gi}, this sum is formally expressed as

$$\varepsilon_{k,g} = \frac{\rho_g}{2\delta k} \sum_{k'=k}^{k+\delta k} \tilde{u}^*_{gi} \tilde{u}_{gi}, \tag{34}$$

where the star superscript denotes complex conjugation. The expression is divided by δk to preserve the defined units. The sum of all of these contributions must equal the total volume-integrated energy of the domain, thus the discrete infinite sum (i.e., $\forall k$, where $k = 0,\ \delta k,\ 2\delta k,\ \cdots$)

$$\sum_{k=0}^{\infty} \varepsilon_{k,g} \delta k = \left\langle \frac{1}{2}\rho_g u_{gi} u_{gi} \right\rangle = \varepsilon_g, \tag{35}$$

as defined in Equation (32). Based on this, we motivate a similar parsing of the total perturbation kinetic energy contained in the particle fluid. Unlike the gas component,

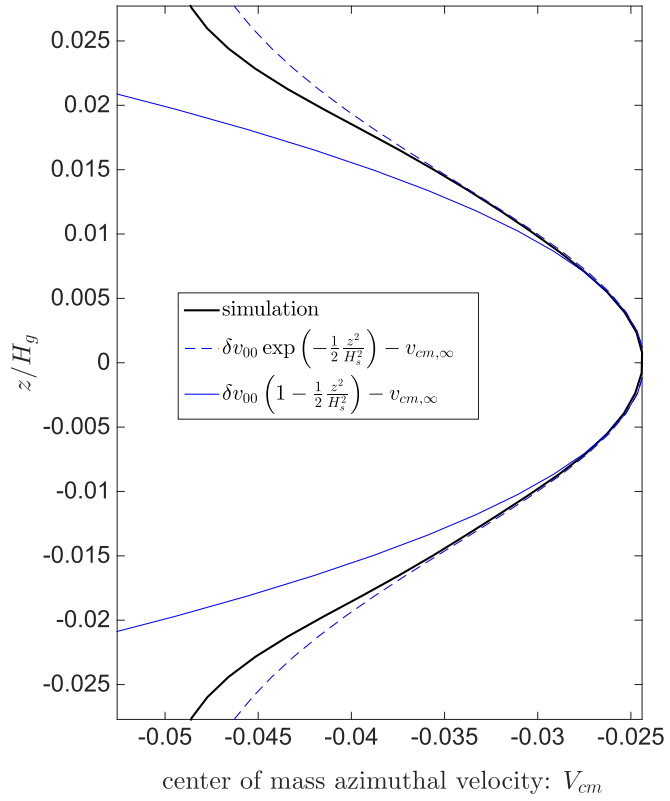

Figure 15. An azimuthally radially averaged plot of the center-of-mass azimuthal velocity $V_{\rm cm}$ for simulation B3D-04M taken at $t\Omega = 4$. The corresponding Gaussian fit and its parabolic approximation are shown. The fit parameters are found in Table 3.

whose density is treated as constant, the particle component has strongly fluctuating densities, and to properly account for its partial energies in Fourier space, we define a new quantity $\mu_i \equiv \sqrt{\rho_p}\, u_{gi}$, which is amenable to sensible interpretation and analysis (see Appendix A). Similarly denoting $\tilde{\mu}_i$ to be the Fourier transform of μ_i, we define

$$\varepsilon_{k,p} = \frac{1}{2\delta k}\sum_{k'=k}^{k+\delta k} \tilde{\mu}_i^{*}\tilde{\mu}_i, \tag{36}$$

whose infinite discrete sum over k yields ε_p, i.e.,

$$\sum_{k=0}^{\infty} \varepsilon_{k,p}\delta k = \left\langle \frac{1}{2}\rho_p v_i v_i \right\rangle = \varepsilon_p. \tag{37}$$

An overarching long-term programmatic goal into the future is to assess the dependencies of $\varepsilon_{k,g}$ and $\varepsilon_{k,p}$ on $|\boldsymbol{k}|$ and to gain some understanding of how energy flows between scales (i.e., in what direction does it move, are there multiple cascades involved, etc.) and what mechanisms are mainly responsible for this transfer. While the latter set of aims is outside the scope of this study, in this preliminary examination we empirically show what the spectrum may possibly look like based on our highest-resolution simulations and what various trends occur as simulation parameters change. Under simplifying assumptions (isotropy, single fluid, etc.) the Kolmogorov dependence $\varepsilon_{k,g} \sim k^{-5/3}$ falls out of the above equation on the assumption that there exists a range in wavenumbers (the inertial range) in which the rate of energy transfer across the sphere of radius k, i.e., $\varepsilon_{k,g}$, is steady in time. Typically once a simulation has reached a statistically steady state, in which the energy injected is compensated by losses (see above), an energy spectrum is assessed. In the simulations we have conducted, any mismatch in this results in a momentary change in the total energy of the system, which averages out over long stretches of time. It is for this reason that spectra produced from simulations are made from composite averages at several time steps.

4.2.1. Calibration Spectra

As we alluded to in Section 2, the numerical diffusion in the simulations (namely, hyperdiffusion) restricts the usable domain in k-space to examine turbulent dynamics and, as such, sets a length scale below which the validity of results—vis-à-vis turbulent dynamics and associated structures—ought to be viewed with great caution. Hence, to identify the reliable simulation subdomain and identify the location of the dissipation scale set by the numerical methods, we conducted a gas-only 512^3 simulation (F3D-512) in a $(2\pi)^3$ periodic domain where turbulence is forced at some larger length scale by a simple forcing function.

In order to obtain a calibration spectra, we have used the forcing module already existing in the PENCIL code without any modifications. The temporally random forcing function $\boldsymbol{\mathcal{F}} = \boldsymbol{f}(\boldsymbol{x}, t)$ can be written as (Brandenburg 2001)

$$\boldsymbol{f}(\boldsymbol{x}, t) \equiv \mathrm{Re}\,\{\mathcal{N}\boldsymbol{f}_{\boldsymbol{k}(t)}\exp[i\boldsymbol{k}(t)\cdot\boldsymbol{x} + i\phi(t)]\}. \tag{38}$$

Here $\boldsymbol{k}(t)$ and $\phi(t)$ respectively denote the time-dependent wavevector and random phase with $|\phi(t)| < \pi$. $\mathcal{N}$ is the normalization factor, which varies as $\delta t^{-1/2}$, with δt being the time step. We choose to force the system at $k = 2$, in which case at each step a randomly chosen possible wavenumber with $1.5 < |\boldsymbol{k}| < 2.5$ is forced. The forcing is executed with the eigenfunctions of the curl operator

$$\boldsymbol{f}_{\boldsymbol{k}} = \frac{i\boldsymbol{k}\times(\boldsymbol{k}\times\hat{e}) - \sigma|\boldsymbol{k}|(\boldsymbol{k}\times\hat{e})}{\sqrt{1+\sigma^2}\boldsymbol{k}^2\sqrt{1-(\boldsymbol{k}\cdot\hat{e})^2/\boldsymbol{k}^2}}. \tag{39}$$

Here $\hat{e}$ is the arbitrary unit vector used to generate $\boldsymbol{k}\times e$, which is perpendicular to $\boldsymbol{k}$. σ denotes the helicity factor, which is set to zero in order to make the forcing purely nonhelical. Note that this forcing is essentially divergenceless. However, as the fluid equations solved by the code are not strictly incompressible, which is perhaps more applicable for astrophysical systems, a small nonzero divergence is introduced over the course of the simulation. Nonetheless, the spatiotemporal dynamics of all of our simulations are effectively incompressible, where density variations are extremely weak (see, e.g., the quantity $\bar{\Pi}'$ in Figures 2–3).

The power spectra obtained from the simulation F3D-512 using the method outlined in Section 4.2 and Equation (34) are shown in Figure 16. It is evident from the figure that in the simulation the turbulence is resolved and a cascade of energy toward smaller length scales (higher k) is taking place with an inertial range spanning more than a decade. The energy density behaves like a power law, i.e., $\varepsilon_k \sim k^{-n}$, with $n = 1.65 \pm 0.03$ best fitting the inertial range, confirming that to within reasonable error this solution is consistent with Kolmogorov's spectra (with an $n = 5/3$) expected for homogeneous isotropic turbulence. However, it is important to note that the actual dissipation scale set by the simulation is placed somewhere around $k_{\mathrm{N},D} \approx k_{\mathrm{N}}/4$, where k_{N} is the Nyquist wavenumber corresponding to a wave spanning two grid points ($2\Delta x$). This

Table 3
Derived Parameters for Plots Shown in Figure 14

Simulation ID	$t\Omega$	Phase	H_p[a]	H_s[a]	δv_{00}[b]	ϵ_0	$\mathrm{Ri}_{\phi,0}$	Ro[c]
A2D-04H	0.5	bounce	0.0098	0.0136	0.025	1.02	0.279	0.919
	1.5	bounce	0.0094	0.0137	0.025	1.06	0.315	0.912
	3.0	bounce	0.0089	0.0126	0.027	1.13	0.238	1.071
	6.0	bounce	0.0084	0.0129	0.030	1.19	0.244	1.163
	15.0	shear	0.0117	0.0129	0.028	0.94	0.150	1.085
B3D-04L	4.0	bounce	0.0092	0.0141	0.0257	1.08	0.361	0.911
	6.0	bounce	0.0089	0.0138	0.0265	1.12	0.350	0.960
	52.0	shear	0.0096	0.0153	0.0257	1.011	0.455	0.840
	500.0	pattern	0.0134	0.0218	0.0225	0.745	1.062	0.516
A2D-2H	3.0	bounce	0.0056	0.0091	0.0335	1.790	0.125	1.841
	6.0	bounce	0.0037	0.0059	0.0419	2.521	0.038	3.551
	12.0	shear	0.0073	0.0165	0.0350	1.509	0.670	1.061
B3D-2M	6	bounce	0.0031	0.0056	0.0445	3.211	0.039	3.973
	28.0	shear	0.0058	0.0101	0.0289	1.730	0.237	1.431
	160.0	pattern	0.0170	0.0162	0.0223	0.543	0.168	1.377

Notes.
[a] In units of H_g.
[b] In in units of c_s.
[c] Rossby number defined in Equation (62).

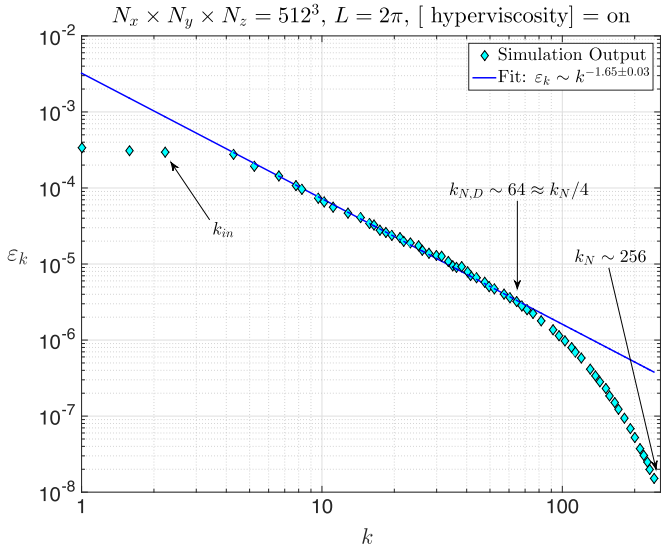

Figure 16. Kinetic energy spectra ε_k vs. k produced from the 512^3-element forcing run F3D-512. Simulation of cube with side $L = 2\pi$ and forcing wavenumbers $2.5 < k_{\rm in}L < 3.5$. A fit to the simulation output reveals an inertial range Kolmogorov dependence $\varepsilon_k \sim k^{-5/3}$ in the range $k_{\rm in} < k \lessapprox k_{\rm N}/4$, where $Lk_{\rm N} = 256$ is the Nyquist scale ($2dx$).

trend in kinetic energy power is ubiquitous across all of our science simulations listed in Table 2 (see below for more details).

It is also important to mention that the use of hyperviscosity can lead to a bottleneck effect where energy gets piled up at the smaller scale (e.g., Haugen & Brandenburg 2004). This happens particularly when the hyperviscosity is not strong enough to dissipate the energy at those small scales (high wavenumber). This effect is particularly problematic, as the accumulated energy tends to scatter back to the larger scale seeking an equipartition among all wavenumbers, ultimately altering the power spectrum and the overall gasdynamics. Note that this numerical effect is not the same as inverse cascade, where an upscale enstrophy cascade takes place.

During the early stages of this investigation, we found that choosing the hyperviscosity parameter to too low a value led to the bottleneck effect, which resulted in code blow-up characterized by widespread generation of $2\Delta x$ waves. Following selection guidelines documented in Haugen & Brandenburg (2004), as well as in the PENCIL manual, we have carefully chosen the values of hyperviscosity for all our simulations to ensure that the bottleneck effect does not kick in and the gas energy does not show any upward trend in the dissipation range, a feature characteristic of the bottleneck effect.

4.2.2. Energy Spectra from Particle–Gas Simulations: St = 0.2

With the calibration established in the previous section, we now move on to the science simulations and discuss the energy spectrum produced by them, along with any possible interpretations that may follow. In Figure 17 we show the energy spectrum for $\mathrm{St} = 0.2$ for both full 3D (Figures 17(a)–(b)) and 3D axisymmetric (Figures 17(c)–(d)) simulations for both gas and solid components.

Figure 17(a) shows energy spectra for both the gas and particle fluids for the B3D-2M simulation during its midplane shear-turbulent phase. It is the average of the time steps $t\Omega = 28$, 35, and 55. We note several features: starting from $k \approx 220H_g^{-1}$ and going up to about $k_{N,D} = k_N/4 \approx 1000H_g^{-1}$, the energy density of the gas component exhibits power-law behavior, i.e., $\varepsilon_{k,g} \sim k^{-n_g}$ with $n_g = 1.15 \pm 0.06$. For this set we established the inferred power-law fit using a least-squares procedure utilizing energy data starting from $k \approx 350H_g^{-1}$ up to $k = k_{\rm N}/4.5$, just shy of the expected cutoff $k_{{\rm N},D}$. As expected based on our calibration spectra, $\varepsilon_{k,g}$ steeply plummets beyond $k_{{\rm N},D}$. Up to the beginning of the observed power-law behavior $\varepsilon_{k,g}$ carries power that largely lies above the power that might have been predicted had the power law been extended to larger scales: that is to say, larger-scale modes in the gas component all lie above the blue line. Similarly, the particle component also exhibits power-law behavior in the same k range as the gas

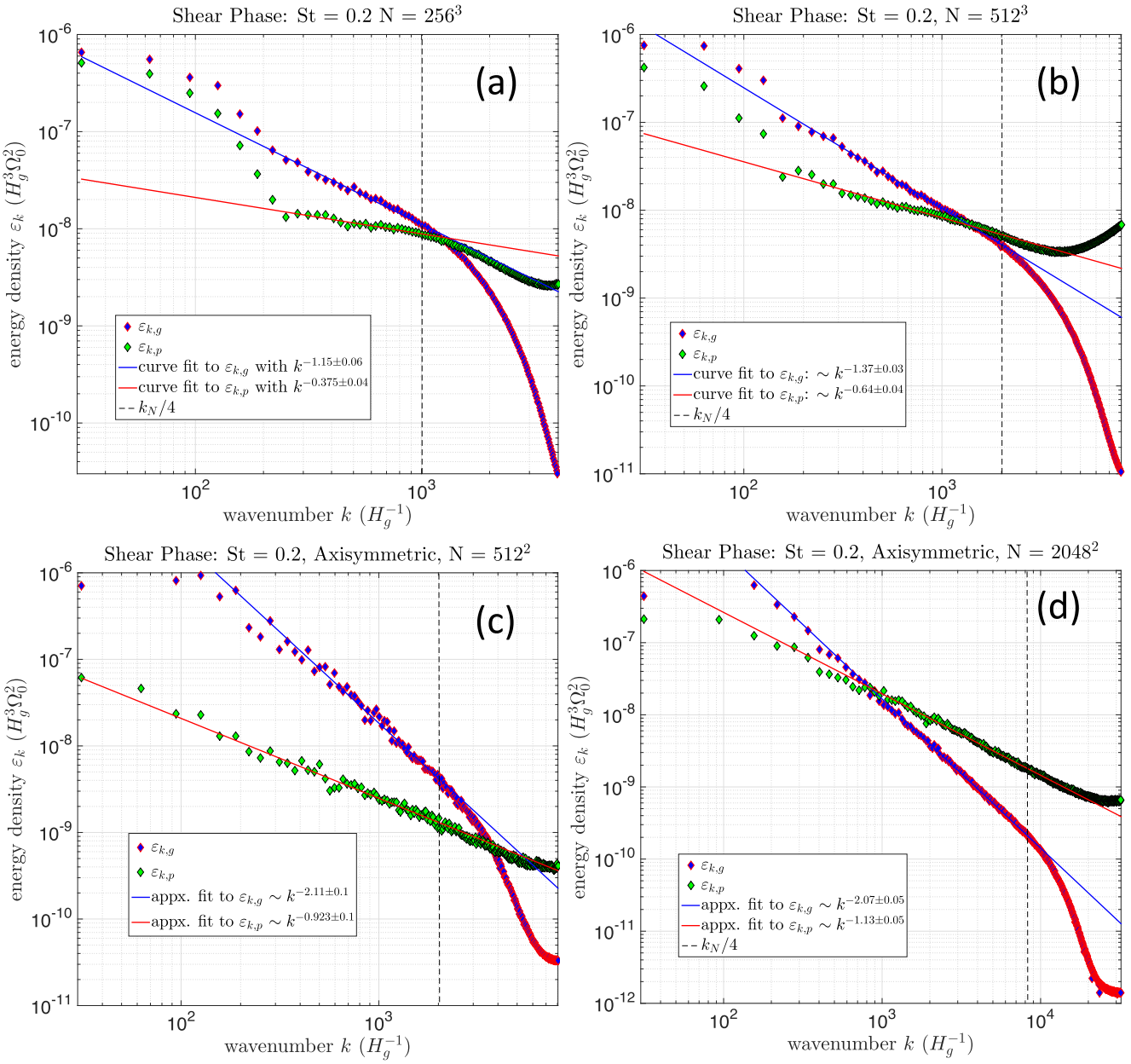

Figure 17. The kinetic energy spectrum from the science simulations with St = 0.2 at the shear phase. The top row shows the spectrum from the 3D simulations with (a) moderate (B3D-2M) and (b) high (B3D-2H) resolution. The purple and green diamonds respectively show the power for gas and solids. The bottom row shows the spectrum for the 3D axisymmetric simulations with (c) low (A2D-2H) and (d) high (A2D-2SH) resolution. The pink and green diamonds represent the spectral energy density for gas and solids. The vertical dashed lines correspond to the wavenumber $k_N/4$, the dissipative end of the nominal inertial range. In all four cases, the blue and red solid lines represent power-law fits to the nominal inertial range of each spectrum (between $kH_g \approx 350$ and $k_N/4$) of the gas and dust, respectively. The power-law index fits to the inertial range of the 3D spectra significantly steepen upon increasing resolution from 256^3 to 512^3. However, no such difference is observed in the axisymmetric simulations when going from 512^2 to 2048^2 resolution, suggesting that these are effectively converged for 512^2 resolution. (See text for more discussion.)

component, but its power-law index is flatter, i.e., $\varepsilon_{k,p} \sim k^{-n_p}$ with $n_p = 0.375 \pm 0.04$. Just like in the gas component, for scales larger than $k \approx 220 H_g^{-1}$, the particle field also contains power larger than that predicted by extending the observed power-law behavior into that regime. With some caution, we therefore *nominally* identify $k_{\rm integral} = 220 H_g^{-1}$ as the start of an inertial range for both fluids. While we observe that the energy contained in the particle component is generally dominated by the gas component up to the beginning of the numerical dissipation scale $k_{N,D} \approx 1000 H_g^{-1}$, the two values appear to be equal to one another at $k \approx 1300 H_g^{-1}$, which lies at slightly shorter scale. Nonetheless, this equality is confirmed at higher resolution.

Figure 17(b) shows the corresponding energy spectra for the B3D-2H simulation. It is constructed as the average spectra of only two time stamps, $t\Omega = 35$ and 55. We immediately note that energy in the gas and particles is indeed equal at the length scale $k \approx 1300 H_g^{-1}$, which is noteworthy. As expected, this higher-resolution simulation shows power-law behavior for a full decade in scales ranging from $k \approx k_{\rm integral}$ up to $k_{N,D} \approx 2000 H_g^{-1}$, extending the resolvable turbulent range by a factor of two in scale. However, we find that the power-law

index in this higher-resolution run has steepened in both quantities where $n_g \approx 1.37 \pm 0.03$ and $n_p \approx 0.64 \pm 0.04$. Based on this, we are led to the tentative conclusion that the 256^3-element simulation is not statistically converged. Whether or not the higher-resolution 512^3-element solution is converged cannot be judged at this juncture, requiring a future even higher-resolution simulation for confirmation. However, from our findings for the 3D axisymmetric runs discussed further below, we conjecture that this 512^3 simulation may have this medium-scale inertial range converged.

This lack of convergence does not appear to be an issue for the 3D axisymmetric simulations we investigated, where we have conducted two runs, one being "high" resolution with 512^2 elements (simulation A2D-2H) up to "superhigh" resolution with 2048^2 elements (simulation A2D-2SH). In Figures 17(c) and (d), the energy spectra for the axisymmetric simulations for both the gas ($\varepsilon_{k,g}$; purple diamond) and the solids ($\varepsilon_{k,p}$; green diamonds) are shown. The spectrum for the gas from the high-resolution run (512^2) follows a power law $\varepsilon_{k,p} \sim k^{-n_g}$ in the inertial range, where $n_g = 2.11 \pm 0.1$. The same for the super-high-resolution simulation (2048^2) comes out as $n_g \approx 2.07 \pm 0.05$, lying in the same range of its 512^2 counterpart within reasonable errors, indicating a convergence in the simulations. The beginning of the inertial range in both the cases starts at $k_{\rm integral} \approx 200 H_g^{-1}$, extending all the way to $k_{{\rm N},D} \approx k_{\rm N}/4$ in the respective cases, producing an inertial range slightly less than a couple of decades in the super-high-resolution run.

When compared to the full 3D simulations, the 3D axisymmetric cases produce a much steeper slope for $\varepsilon_{k,g}$, which falls well within our expectation. Throughout this discussion we keep in mind that the energetics and transport characteristics in 2D isotropic turbulence (no rotation, no stratification) are inherently different from those of its 3D isotropic counterpart, with the former exhibiting prominent enstrophy cascade toward smaller scales. Questions such as what might the transport characteristics be for flows like these representing a section of disk, where rotation and stratification are dynamically important, and is there a dual cascade of energy and enstrophy in the axisymmetric case currently remain open. With this in mind, we note that the gas energy $\varepsilon_{k,g}$ at the wavenumber $k_{{\rm N},D} \approx k_{\rm N}/4$ is approximately the same around $3 \times 10^{-9} H_g^3 \Omega_0^2$, whereas the energy at the integral scale ($k_{\rm integral} \approx 200 H_g^{-1}$) is approximately an order of magnitude more in the 3D axisymmetric run (A2D-2H) compared to the full 3D one (B3D-2H). Whether this extra energy in the axisymmetric simulation is a result of a more efficient extraction of free energy from the background shear at $k_{\rm integral}$ or an outcome of some upscale and—as yet—unquantified energy cascade mechanism is not known, requiring further investigation.

The energy spectra in the particles $\varepsilon_{k,g}$ in the two simulations, though, show a little difference in the power-law behavior. For simulation A2D-2H with 512^2 resolution, the inertial range follows a power law k^{-n_p} where $n_p \approx 0.923 \pm 0.1$. For simulation A2D-2SH, however, $n_p \approx 1.13 \pm 0.05$. The power-law behavior of the two-particle spectrum with a shallower slope extends beyond the wavenumber $k_{\rm N}/4$, with significantly more energy compared to the gas fields at the small scales, a feature that is still unclear to us.

In Figure 18, a collapsed gas energy spectrum for the 3D simulation B3D-2H is presented based on the azimuthally averaged velocity fields ($k_y = 0$; purple circles). The power-law

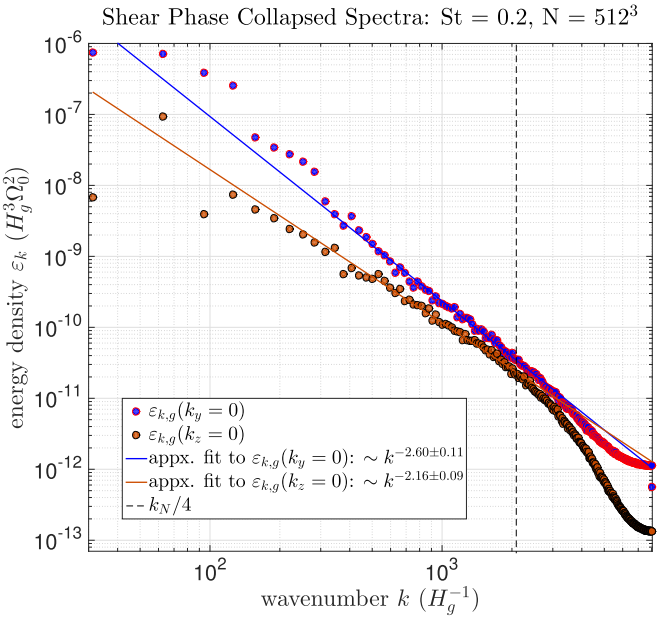

Figure 18. Energy spectrum $\varepsilon_{k,g}$ for the gas field from simulation B3D-2H collapsed in the azimuthal ($k_y = 0$) and vertical ($k_z = 0$) direction. An inertial range in the azimuthally collapsed spectra is steeper than the 3D axisymmetric simulation A2D-2H (see Figure 17(c)) with the same resolution, implying the existence of additional energy modes in the axisymmetric direction.

index in $\varepsilon_{k,g}$ for the inertial range here comes out as $n_g \approx 2.6 \pm 0.11$, which is significantly steeper than the corresponding 3D axisymmetric run A2D-2H. From this result we infer that there are additional modes of energy transfer into and out of axisymmetric structures that are otherwise suppressed in the 3D axisymmetric simulations. We also show the gas energy spectrum for the vertically averaged velocity fields ($k_z = 0$; orange circles), which exhibit power-law behavior with an index $n_g = 2.16 \pm 0.09$. How these may or may not relate to overall composite spectrum remain to be elucidated. We note that the power-law behavior in both cases here extends somewhat beyond the cutoff wavenumber $k_{\rm N}/4$; however, we caution against inferring anything about the meaning of this until further analysis is done.

4.2.3. Energy Spectra from Particle–Gas Simulations: St = 0.04

Figure 19 shows the energy spectra $\varepsilon_{k,g}$ and $\varepsilon_{k,p}$ for gas and particle fields, respectively, for St = 0.04. Panel (a) is derived from the 256^3 3D simulation B3D-04M. Panels (b) and (c) are from the axisymmetric simulations A2D-04H and A2D-04SH, respectively, with the averages taken with the snapshots at $t\Omega = 80$, 120, and 220.

The energy spectrum $\varepsilon_{k,g}$ for the gas field from the 3D run shows an unexpected nearly flat behavior: $\varepsilon_{k,g} \sim k^{-n_g}$ with $n_g \approx 0.0972 \pm 0.02$. The flat region of the spectra starts at $k_{\rm integral} \approx 300 H_g^{-1}$ and extends up to $k_{{\rm N},D} \approx k_{\rm N}/4 \approx 1000 H_g^{-1}$. The lower resolution of the simulation constrains the bandwidth of the inertial range well short of a decade. Beyond $k_{{\rm N},D}$, the energy in the gas field drops by nearly a couple of orders of magnitude, and no bottleneck effect is observed either. An unusual pattern is also observed in $\varepsilon_{k,p}$, where the inertial range follows a power law with a positive index: $\varepsilon_{k,p} \sim k^{-n_p}$ with $n_p \approx -0.218 \pm 0.06$. Similar to the simulations with St = 0.2, an increase in the particle energy is also evident here beyond $k_{{\rm N},D}$. We are yet to identify the exact

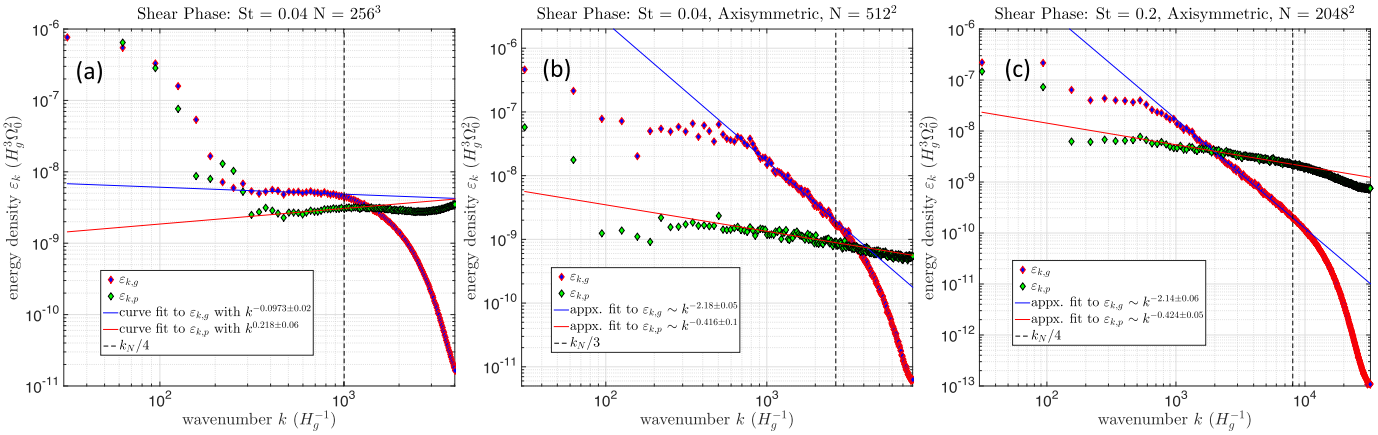

Figure 19. Kinetic energy spectrum from simulations with St = 0.04 at the shear phase for both 3D and 3D axisymmetric runs. Panel (a) shows the spectrum for simulation B3D-04M, with the purple and green diamonds representing the gas and particle energy, respectively. Panels (b) and (c) show the energy spectrum from the axisymmetric runs A2D-04H and A2D-04SH, respectively. Similar to Figure 17, the blue and red solid lines are the power-law fit to the gas and particle spectral energy densities, respectively. The vertical black dashed lines denote the positions for $k_N/4$. For both axisymmetric runs, the inertial ranges for the gas and solids follow a similar power-law index. The monotonic decrease of the gas energy beyond the inertial range ensures that the bottleneck effect is not at play.

reason for the observed behavior in the gas and particle field energy at these small scales. However, it is important to remark that a proper understanding of such systems in the fluid turbulence literature is still in its infancy, and a community-wide effort to better understand the particle–gas interplay in a protoplanetary disk setup is warranted. In terms of the convergence of the 3D simulation, it is still too early to assert anything without a high-resolution simulation with St = 0.04 similar to B3D-02H. Unfortunately, we do not have that at this point owing to limited available computational resources.

In case of the 3D axisymmetric simulations (Figures 19(b) and (c)), we see that $\varepsilon_{k,g} \sim k^{-n_g}$ where $n_g \approx 2.18 \pm 0.05$ for A2D-04H with 2560 grids per H_g and 2.14 ± 0.06 for A2D-04SH with 10,240 grids/H_g. In both cases, the inertial range starts at $k_{\rm integral} \approx 500 H_g^{-1}$ and extends through $k_{{\rm N},D} \sim k_{\rm N}/4$. However, as is expected from the low-resolution run, the bandwidth of the inertial range is significantly shorter compared to its high-resolution counterpart. It can be safely asserted that the 3D axisymmetric simulations with St = 0.04 are converged with the same power-law indices of the inertial range within acceptable uncertainties. When studied in parallel to the ones with St = 0.2, it only looks more certain that 512^2 resolution (2560 grids/H_g) is probably where a statistical convergence is attained.

The energy spectrum for the particles $\varepsilon_{k,p}$ also behaves in a similar fashion for the 3D axisymmetric simulations where $\varepsilon_{k,p} \sim k^{-n_p}$ with $n_p \sim 0.0416 \pm 0.1$ for A2D-04H and 0.424 ± 0.05 for A2D-04SH. Interestingly, $\varepsilon_{k,p}$ in both cases do not fall off beyond $k_{{\rm N},D}$, but follow the inertial range trend extending through the smallest scales. As we mentioned before, more attention to this matter is needed in order to understand the particle–gas interplay in the smallest scales, where the majority of the interesting physics take place in the context of planetesimal formation.

5. Selected Linear Analyses

5.1. Ekman Spirals, Off-midplane Kelvin–Helmholtz Roll-up, and Ri of Settling Dust

Most of our simulations begin from a laminar state in which dust particles are distributed symmetrically about the midplane using a Gaussian profile with some initial particle scale height H_{p0}. It is of interest—in particular, with respect to turbulent development—to understand how the horizontal velocity components develop as the particles begin their settling toward the midplane. We expect that the system will respond by setting up a velocity field reminiscent of an Ekman layer, as predicted for particle–gas layers in disks (Dobrovolskis et al. 1999), but modified by epicyclic motions. We therefore consider the horizontally uniform spatiotemporal evolution of the gas and particle velocities as an initial value problem of particles released from rest initially distributed as just described.

In Appendix B we detail the methods we use to derive the solutions discussed here, which have similarities to the solutions developed in Lin (2021). We condense here the basic assumptions of our problem:

1. We assume horizontally uniform solutions.
2. Since the particles are distributed over a layer that is significantly smaller than H_g, together with the earlier observation that the evolution of the gaseous component is essentially incompressible in our main simulations, we assume the gas density to be constant and denote it as $\bar{\rho}_g$.
3. In steady state the gas has no appreciable vertical motion.
4. The particles are treated as a second fluid with a steady vertical velocity that varies linearly, i.e., $W_p = -\Omega_0 \beta z$, where $\beta = \beta_-({\rm St})$ is a constant found in Equation (B8) in Appendix B (see also Lin 2021).
5. The particle density exhibits homologous evolution preserving its Gaussian form defined on the time-dependent particle scale height $H_p(t)$:

$$\varepsilon \equiv \frac{\rho_p}{\bar{\rho}_g} = \varepsilon_0(t) \exp\left(-\frac{z^2}{2H_p^2}\right),$$
$$H_p = H_{p0} \exp\left(-\beta\Omega_0 t\right),$$
$$\varepsilon_0(t) = \varepsilon_{00} \exp\left(\beta\Omega_0 t\right). \quad (40)$$

6. And since the total dust mass is vertically conserved, in which it follows $\varepsilon_{00} = Z \cdot (H_g/H_{p0})$, solutions are defined by an input value of St, H_{p0}, and local metallicity Z.

The numerical method employed to solve this problem is different from what is used in PENCIL. Since our aim is to

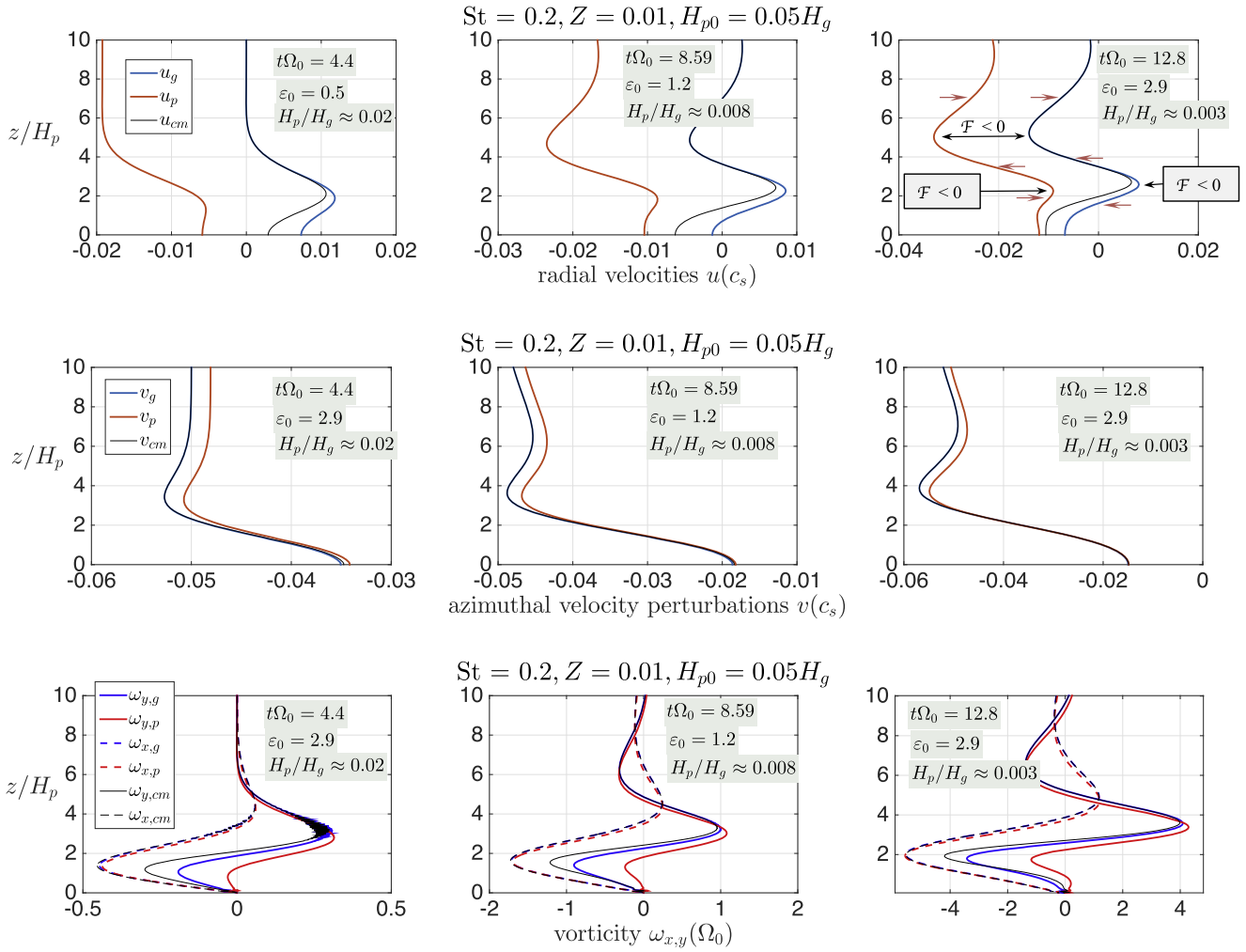

Figure 20. Settling solutions for St = 0.2, $Z = 0.01$, and initial particle scale height $H_{p0} = 0.05H_g$, at three selected times. Top row: the radial velocities of the gas (blue), particles (red), and center of mass (gray); middle row: corresponding perturbation azimuthal velocities; bottom row: associated azimuthal (solid lines) and radial vorticities (hatched lines). Panel insets also indicate midplane values of ε_0 and H_p.

follow the emergence of horizontal jets as the layer continues its inexorable collapse toward the midplane, it is necessary to resolve the ever-finer developing scales on which particle–gas momentum exchange occurs—something that cannot be reliably done in simulations with a static vertical grid, especially when the particle scale height approaches the grid scales itself. The method described therefore follows the evolution of the particle–gas layer in a vertically comoving coordinate frame formulated on a Gaussian grid characterized by the time-dependent particle scale height $H_p(t)$ found in Equation (40). For further details of the method see Appendix B.

We discuss the broad properties of the settling solutions by showcasing results for the two values of St we consider in our large production runs, i.e., St = 0.04 and 0.2, together with $Z = 0.01$. Our main focus here will be on the latter St value, displaying the former in Appendix B. Of the several features we find for St = 0.2, perhaps the main one is the emergence of anywhere from three to seven counterflowing radial jets in both the particle and gas fluids. There is always one main midplane jet whose tip lies at $z = 0$, and this is further sandwiched by jet pairs at symmetric locations away from the midplane. In the simulations involving St = 0.2 particles, two symmetric jet pairs form by the time the midplane layer achieves $\varepsilon = 1$. With increasing distance from the midplane the jets are counterflowing with respect to one another: the locations of the tips of these counterflowing jets for St = 0.2 are generally found at 2.5 and 5 particle scale heights away from the midplane (see, e.g., black arrows in top row of Figure 20), while for St = 0.04 the jets tips are found at $2H_p$ and $3.5H_p$ away from the midplane. We note also that the amplitude of the jet flow—especially the midplane jet—varies epicyclically, exhibiting periods of flow reversal (see further below).

The perturbation azimuthal velocity fields (i.e., $v'_{g,p}$) also display multiple jet flow characteristics like u, but by contrast the profile is dominated by the prominent midplane jet. Only by later times (see, e.g., top rows of Figures 20 and B1, second and third panels) do weaker counterflowing jets also appear above and below the midplane.

As the particles continue to settle, the radial and azimuthal vorticity components of the jet vorticity—$\omega_x = -\partial_z v$, $\omega_y = \partial_z u$ (respectively for each fluid)—steadily increase since H_p continuously shrinks. When the particles sufficiently settle so that $\varepsilon_0 = \mathcal{O}(1)$, the components of vorticity in each fluid are similarly $\mathcal{O}(\Omega_0)$.

We find that the particle and gas velocity fields generally follow one another especially at regions well above one particle scale height. We have defined center-of-mass velocity

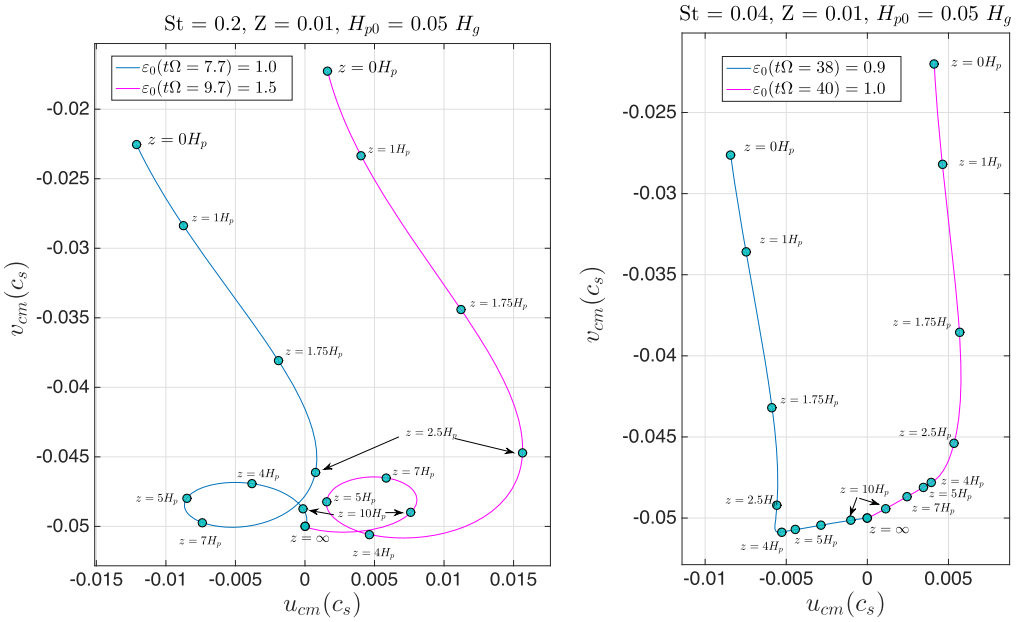

Figure 21. Ekman spirals, constructed on the center-of-mass horizontal velocities, based on the 1D settling solutions at selected times: St = 0.2 (left) and St = 0.04 (right). Several fixed values of $z/H_p(t)$ are labeled.

quantities,

$$u_{\rm cm} \equiv \frac{u_g + \varepsilon u_p}{1+\varepsilon}; \qquad v_{\rm cm} \equiv \frac{v_g + \varepsilon v_p}{1+\varepsilon}, \tag{41}$$

and similarly derive corresponding vorticities, $\omega_{x,\rm cm} = -\partial_z v_{\rm cm}$ and $\omega_{y,\rm cm} = \partial_z u_{\rm cm}$. These are shown throughout all plots in Figures 20–B1. In the same spirit, we define an effective averaged density fluctuation around a mean state in each fluid denoted by subscript "0" as the following sum:

$$\frac{\rho'_{\rm cm}}{\rho_{g0}+\rho_{p0}} = \frac{\rho'_g/\rho_{g0} + \epsilon\rho'_p/\rho_{p0}}{1+\epsilon}. \tag{42}$$

The buoyancy, b, is defined as the vertical gravity multiplying the density fluctuation. Since for all practical concerns here the gas is effectively incompressible ($\rho'_g \approx 0$), the buoyancy simplifies to

$$b_{\rm cm} \approx g\frac{\epsilon\rho'_p/\rho_{p0}}{1+\epsilon} = \Omega_0^2 z \cdot \frac{\epsilon}{1+\epsilon}\frac{\rho'_p}{\rho_{p0}}, \tag{43}$$

which follows on the physically motivated form introduced by Chiang (2008).

One immediately notes how Ekman-layer structure develops with increasing severity as the particles continue their collapse. Figure 21 predicts intensifying Ekman spirals based on the 1D solutions. This Ekman flow—which exhibits varying horizontal velocities as a function of height away from the midplane—is shown for both St values at different times, corresponding to values of ε_0 around 1. The emergence of such behavior is not a surprise and is expected to be a generic feature of midplane-settled protoplanetary disk dust layers (Cuzzi et al. 1993; Dobrovolskis et al. 1999). The plots, indicating the center-of-mass horizontal velocities, also have several values of z/H_p labeled. Interestingly, the spiral structure is more pronounced for St = 0.2, as the velocity fields exhibit more than one complete loop. We note that the $z/H_p \to \infty$ limit corresponds to zero radial speeds and an azimuthal velocity corresponding to $-0.05c_s$, which is the expected limiting form under a uniform pressure gradient in a region absent of particles according to Equation (B20) with $\delta = 0.05$ (see also Lin 2021). For comparison, Figure 22 shows the Ekman flow structure as appearing in the simulations at various time steps. The basic qualitative agreement between the restricted 1D calculation and the simulations is evident during the early settling and bounce phases of the simulations. A further detailed comparison to assess how far along in time the 1D solutions predict the observed mean horizontal flow structure should be done in a future follow-up study.

The radial jet profiles have several inflection points, i.e., locations z_i where $\partial_z^2 u|_{z=z_i} = 0$, indicating that the flows violate the Rayleigh criterion for stability against shear roll-up (see, e.g., red arrows in the top row of Figure 20). Additionally, we also observe the Fjørtoft criterion, which states that unstable linear perturbations of shear flows must have locations $z = z_f$ in which $\mathcal{F}(z_f) < 0$, where

$$\mathcal{F}(z) \equiv (u(z) - u(z_i)) \cdot \partial_z^2 u|_z. \tag{44}$$

The black arrows in the top row of Figure 20 both designate the level of each jet tip and indicate that these locations clearly satisfy the Fjørtoft criterion. We see that the jets and the locations where these varied stability criteria are met are significantly removed from the particle layer itself. In other words, if these jets go unstable, they do so free from the direct influence of the particles themselves. Of course, these jets are a direct result of the passage of particles through that level during settling.

To this end, we calculate $\mathrm{Ri} = \mathrm{Ri}_{\rm eff}$ at every vertical level as a function of time in the 1D simulations; these are shown in Figure 23. However, instead of plotting the predicted Ri on the horizontal axis in terms of time, we opt for showing them in terms of the midplane value of ε_0—as defined in Equation (40)—which is a more useful proxy for the particle layer's ever-shrinking scale height. We highlight the contour lines where

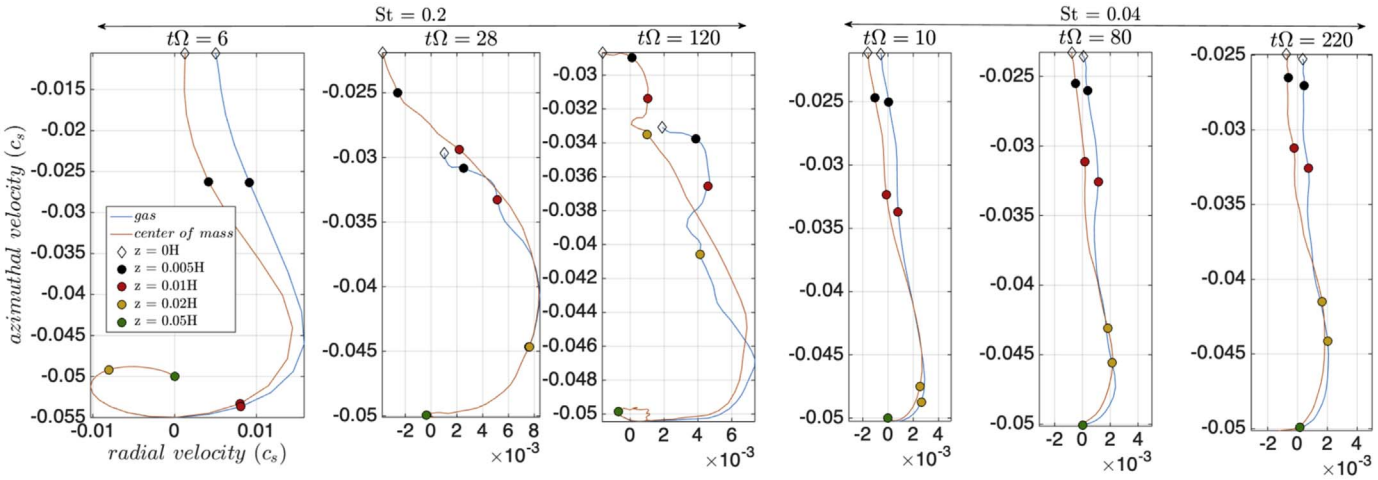

Figure 22. In comparison to Figure 21, we show the emergent Ekman spirals from the simulations of the previous section at several time stamps. Here we show radially azimuthally averaged gas ($\langle u_g \rangle_{xy}$ and $\langle v_g \rangle_{xy}$) and center-of-mass velocities—as defined in Equation (23) with several layer heights labeled for reference. Simulations shown: B3D-2M for St = 0.2 (left three panels) and B3D-04M for St = 0.04 (right three panels). Note that the Ekman flow structure is strongest for St = 0.2 and that it persists well into the turbulent state.

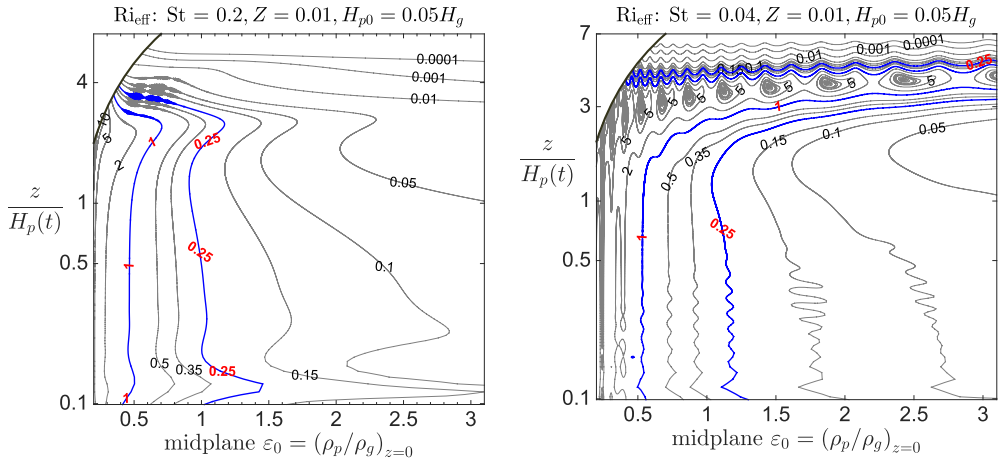

Figure 23. Effective values of $\mathrm{Ri} \leftrightarrow \mathrm{Ri}_{\mathrm{eff}}$ as a function of $z/H_p(t)$ and time, which is proximately represented by the ever-increasing values of $\varepsilon_0(t)$ according to Equation (40). The left panel shows St = 0.2, while the right panel displays St = 0.04. Various values of Ri are labeled. The special values of Ri = 0.25 and 1 are shown with blue contours. The dark arc bounding the upper left corner of each panel represents the fixed vertical physical scale of our PENCIL-code-derived solutions, i.e., $z_b/H_p(t)$.

both $\mathrm{Ri}_{\mathrm{eff}} = 1/4$ and $\mathrm{Ri}_{\mathrm{eff}} = 1$ based on our discussion above. In all cases considered, $\mathrm{Ri}_{\mathrm{eff}}$ becomes less than $1/4$—especially for regions containing the dust-rich layers—once the midplane value of ϵ_0 begins surpassing 1. This is especially evident in the simulation St = 0.2 (Figure 23, left panel), where $\mathrm{Ri}_{\mathrm{eff}} < 0.25$ over the entire vertical extent of the settling layer. For St = 0.04 (Figure 23, right panel) the criterion begins to be violated at $\varepsilon_0 \approx 1$ and gradually expands toward larger values of z/H_p as the midplane gets more dense. In fact, a layer in which $\mathrm{Ri}_{\mathrm{eff}} > 0.25$ appears sandwiched above and below, with vertical extent generally diminishing as the midplane density increases. We note the appearance of oscillatory structure in the contour lines, which is likely due to the well-known and clearly observed epicyclic motions of the jet layer (e.g., Li et al. 2018; Li & Youdin 2021).

It might seem that a similar line of reasoning would lead to the prediction of KH roll-up by nonaxisymmetric perturbations to v owing to its strong midplane jet quality. However, it is likely that such nonaxisymmetrically driven dynamics get washed out by rapid differential azimuthal stretching experienced by all flow lines owing to the strong radial Keplerian shear (as suggested in Ishitsu et al. 2009). However, this remains a conjecture at this point.

Gerbig et al. (2020) have suggested that Ri = 1 constitutes a meaningful transition condition for these settled layers, a possibility we further consider in the next subsection. In anticipation, therefore, we also label in Figure 23 those places corresponding to Ri = 1. We observe that this generally corresponds to values of $\varepsilon_0 = 0.5$.

5.2. Disk Analog of Symmetric Instability

There are recent suggestions that the condition for stability of particle–gas shear flows in strongly rotating protoplanetary disk models, like the ones of concern here, does not need the usual Miles–Howard criterion, $\mathrm{Ri} > 1/4$, to be satisfied (Gómez & Ostriker 2005; Johansen et al. 2006; Barranco 2009; Gerbig et al. 2020)—a possibility supported by some theoretical considerations of the nonlinear stability of stratified flows (e.g., Abarbanel et al. 1984; Miles 1986), and certainly by our numerical simulations reported here. Model atmospheric flows that support nonbarotropic motions can be unstable for

$\mathrm{Ri} > 1/4$. One example of this is the so-called symmetric instability (SymI hereafter), in which axisymmetric azimuthal mean flows whose flow isolines are misaligned with respect to density/entropy isolines are strongly unstable to axisymmetric perturbations for values of Ri up to 1 (e.g., Stone 1966; Vanneste 1993; Stamper & Taylor 2017). The total azimuthal flow profiles considered here, which are the sum of the Keplerian flow $(-3\Omega_0 x/2)$ and $v_{\rm cm}(z, t)$, certainly exhibit isolines that are misaligned with respect to the particle density isolines that vary only with height. This is suggestive that axisymmetric disturbances of the flow profiles during particle settling may indeed go unstable by the same type of mechanism that drives the SymI of atmospheric and oceanic flows.

We note that it has recently been argued that the vertical shear instability (VSI; Nelson et al. 2013) is the disk analog of the SymI (sometimes referred to as "sloping convection" in the geophysical fluid dynamics literature; Yellin-Bergovoy et al. 2021). Indeed, a latitudinal temperature gradient gives rise to a radial variation in planetary zonal flow, while a similar vertical variation of Keplerian flow emerges from a radial temperature gradient that leads to the VSI. The conditions leading to the VSI resemble those giving rise to sloping convection when thermodynamic cooling is instantaneous (zero cooling time-scale) within the disk. In both scenarios, therefore, there is a misalignment between the density and azimuthal/zonal flow isolines. For further exposition see Yellin-Bergovoy et al. (2021).

In the models shown in the figures presented at the end of the previous section we find that the condition $\mathrm{Ri} = 1$ is met over significant volumes of the disk's vertical extent once the midplane ϵ begins exceeding 0.5. At this stage we conclude that under these conditions the particle layer is quite possibly prone to a disk analog version of the SymI.

5.2.1. Motivation

The turbulent transition in the $\mathrm{St} = 0.2$ experiments unambiguously shows the primary role that the KHI plays in churning up the particle layer. This shear roll-up is associated with the jet pairs located at least 2–3 particle scale heights away from the midplane. However, close inspection also reveals that non-Kelvin–Helmholtz-unstable dynamics are also present in the particle layer itself, where the Fjørtoft and Rayleigh criteria for shear instability are not clearly met. This feature is even more prominent in the $\mathrm{St} = 0.04$ simulation, where KH roll-up in the layers away from the particle layer is far weaker, and the evidence for dynamic activity in the particle layer (within $1H_p$–$2H_p$ of the midplane) falls into even further relief. In the observed dynamics we have also found that the primary roll-up occurs in exactly axisymmetric or nearly axisymmetric perturbations.

We argue by analogy to submesoscale atmospheric and oceanic dynamics that dynamical activity in these settled particle layers is driven by the twin action of the SymI and KH roll-up. We suspect that the significance of the SymI in characterizing the VSI (Yellin-Bergovoy et al. 2021) and the vertical shearing streaming instability (VSSI; Lin 2021) also applies to the turbulent development of the midplane dynamics we report here—especially for simulations showing sustained turbulent activity in which the SI emerges either weakly or not at all.

Indeed, analysis of the $\mathrm{St} = 0.04$ simulation after it achieves a quasi-steady shear-driven turbulent state shows that the effective Richardson numbers are near or larger than $1/4$, an important feature also observed in the simulations reported in Gerbig et al. (2020). While it remains to be a circumstantial claim without a more comprehensive analysis, having $\mathrm{Ri}_{\rm eff} > 0.25$ maintained in this turbulent state inspires us to consider that the dynamics are not only driven by KH roll-up (while keeping in mind that a rotationally modified KH roll-up dynamic may also be operating, as suggested originally by Gómez & Ostriker 2005). Most importantly, it is our hypothesis that the KH roll-up is associated primarily with the vertical gradient in the radial flow velocities (whether they be expressed as that of the gas or as those of the center of mass), while SymI action is driven mainly by the vertical gradient of the radial–azimuthal mean of v, i.e., the azimuthal velocity departures from Keplerian flow. As elucidated in submesoscale atmospheric dynamical studies and translated to our disk gas particle framework, the main ingredients for the SymI are that the total mean flow (azimuthal) velocities have isolines that are misaligned with respect to isodensity lines (e.g., Vanneste 1993).

5.2.2. Model Formulation

We therefore present here a motivated single-fluid model (see details in Appendix C) providing an analytically tractable demonstration of the SymI for midplane disk layers. The simplified model can be thought of as the isothermal (i.e., $\gamma \to 1$) and perfectly coupled terminal velocity limiting form of the single-fluid model for dusty-gas mixtures (e.g., Laibe & Price 2014; Lin & Youdin 2017). This limiting form is the extreme limit of the recast two-fluid equation framework developed in Laibe & Price (2014), where the equations of motion are written without approximation instead in terms of center-of-mass velocities and relative velocities of the two-fluid species. This "single-fluid" limiting form emerges from this recast set of equations after both assuming the terminal velocity approximation and taking the asymptotic limit of nearly zero particle stopping times.

To isolate the SymI effect from KH roll-up, we assume that there is only a purely azimuthal mean flow state, which is the sum of the Keplerian profile plus a departure $\tilde{v}_0$ with a parabolic vertical variation given by

$$\tilde{v}_0 = \delta v_{00}\left(1 - \frac{1}{2}\frac{z^2}{H_s^2}\right), \tag{45}$$

where δv_{00} characterizes the mean azimuthal velocity drop across 2–3 particle scale heights. We adopt this as a reasonable facsimile of the center-of-mass azimuthal flow of the simulations, especially during the bounce and shear-turbulent phase of the runs; see also Figure 15 for more details. We justify neglecting the vertical variation of the radial flow based on its relatively small amplitude in comparison to the azimuthal flow —e.g., based on how $\mathrm{Ri}_r \gg \mathrm{Ri}_\phi$ for all of the shear phase $\mathrm{St} = 0.04$ simulations depicted in Figure 14.

The parabolic form for v adopted in Equation (45) is a good fit for the mean profiles that emerge in 3D simulations at various early to intermediate stages of turbulent shear phase development (discussed at the end of Section 3.5) and embodied in the assumed approximate Gaussian form expressed in Equation (28). We assume a mean density ρ_0

whose vertical variation is given by

$$\partial_z \ln \rho_0 = -\frac{z}{H_p^2}, \tag{46}$$

and, following both Chiang (2008) and Gerbig et al. (2020), subject to a reduced gravity term acting toward the midplane, and given in magnitude by

$$g = g_{\rm red} = \frac{\varepsilon_0}{1+\varepsilon_0}\Omega_0^2 z, \tag{47}$$

where ε_0 is a constant (unlike its interpretation and usage in the previous section), nominally representing the dust-to-gas ratio of the midplane, in the same sense as used in Section 5.1. In this framework given Equations (45)–(46) together with no radial velocity, we find according to Equation (24)'s definition of the azimuthal Richardson number that

$$\mathrm{Ri} = \mathrm{Ri}_\phi = \frac{\varepsilon_0}{1+\varepsilon_0}\frac{\Omega_0^2 H_s^4}{\delta v_{00}^2 H_p^2}. \tag{48}$$

We note that henceforth we consider only values of $\mathrm{Ri} > 0$, i.e., stably stratified flows. In order to connect to results discussed in Section 3.5, Ri_ϕ should be considered as being parallel to and in the same spirit of the definition for $\mathrm{Ri}_{\phi,0}$ expressed in Equation (29).

We assume that the dynamics are incompressible, which means that the radial and vertical velocity perturbations may be written in terms of a single stream function ψ. However, vertical density variations are advected by the perturbation flow and give rise to buoyancy effects in the dynamics. Except for being set in a shearing-box framework, there is no other physics including drag exchange and fluid viscosity, have been modeled.

All perturbations are axisymmetric, and we assume normal mode solutions that have the functional form for the stream function ψ', i.e., $=\hat{\psi}(z)\exp(-i\omega_0 t + ikx) + \text{c.c.}$, where ω_0 is the normal mode frequency, k is the horizontal wavelength of the disturbance, and $\hat{\psi}$ is the vertical eigenmode structure function.

In Appendix C we analyze normal mode solutions of the above-described idealized model, which are expressed in terms of parabolic cylinder functions $\mathcal{D}_m(z/\tilde{\beta})$ (Abramowitz & Stegun 1972). Here $\tilde{\beta}$ is the length scale whose real part quantifies the Gaussian decay length scale characterizing $\mathcal{D}_m(z/\tilde{\beta})$—see Equation (C16). The general solution for the frequency ω_0 is given in Equation (C22), which is a function of three parameters: Ri as defined in Equation (48), the nonnegative integers m signifying the number of vertical nodes in the disturbances, and finally μ, in which

$$\mu \equiv \frac{(2m+1)^2}{2k^2 H_p^2}\cdot\frac{\varepsilon_0}{1+\varepsilon_0}, \tag{49}$$

which characterizes a single-parameter family of solutions containing k and ε_0. The general solution for the normal mode response is found in Equation (C22) reproduced here in slightly rewritten form:

$$\frac{\omega_0^2}{\Omega_0^2} = \sqrt{\mu\left(2\frac{\mathrm{Ri}-1}{\mathrm{Ri}} + \mu - \frac{2i}{\nu}\sqrt{\frac{2\mu}{\mathrm{Ri}}}\right)} - \mu + \frac{i}{\nu}\sqrt{\frac{2\mu}{\mathrm{Ri}}}, \tag{50}$$

where we have introduced $\nu \equiv 2m+1$ for notational convenience. Further analysis found in Appendix C proves that normal modes come in growing/decaying pairs for all finite values of $\mathrm{Ri} \neq \mathrm{Ri}_c(m)$, in which

$$\mathrm{Ri}_c(m) \equiv 1 - \frac{1}{\nu^2} = \frac{4m(m+1)}{(2m+1)^2}. \tag{51}$$

Normal modes are marginal for the countably infinite set of $\mathrm{Ri} = \mathrm{Ri}_c(m)$ values. Inspection of Figure 24 indeed shows that the growth rates become dramatically large once Ri passes below Ri_c. Given Ri_c's dependence on m, nominally speaking we expect strong instability when Ri passes under 1, with instability appearing first as $m \to \infty$.

It is instructive to showcase certain limiting cases for the above solutions, which we do in the following subsections.

5.2.3. $\mu \gg 1$ Limiting Form, an $\mathrm{Ri} < 1$ Criterion

We first start by considering the fate of modes in the limit where $\mu \gg 1$, which corresponds to large values of m and/or small values of kH_p. According to Equation (C27), we find

$$\frac{\omega_0^2}{\Omega_0^2} \approx \left(1 - \frac{\mathrm{Ri}_c}{\mathrm{Ri}}\right)\left(1 + i\frac{1}{\nu}\sqrt{\frac{2}{\mu\mathrm{Ri}}}\right) + \mathcal{O}\left(\frac{1}{\mu}\right), \tag{52}$$

which means that up to $\mathcal{O}(1/\sqrt{\mu})$, ω_0 is

$$\frac{\omega_0}{\Omega_0} = \pm\sqrt{1 - \frac{\mathrm{Ri}_c}{\mathrm{Ri}}}\cdot\left(1 + i\frac{1}{2\nu}\sqrt{\frac{2}{\mu\mathrm{Ri}}}\right) + \mathcal{O}\left(\frac{1}{\mu}\right). \tag{53}$$

There is a dramatic change in the character of the modes when $\mathrm{Ri} - \mathrm{Ri}_c$ crosses zero. When $\mathrm{Ri} > \mathrm{Ri}_c$, the oscillating disturbances, while being unstable, have a growth rate that is weak and proportional to $1/\sqrt{\mu}$. However, once $\mathrm{Ri} < \mathrm{Ri}_c$, then the modes show order 1 growth. This says that the character of the disturbances undergoes a stark transition at $\mathrm{Ri} \approx \mathrm{Ri}_c$. We also observe that the modes with the highest values of m are the most unstable when $\mathrm{Ri} < \mathrm{Ri}_c$. For a layer undergoing collapse, where the value of Ri is steadily going down, the modes with the highest values of m begin to go unstable once $\mathrm{Ri} < 1$ since $\mathrm{Ri}_c(m \to \infty) = 1$. Outside of $m = 0$, for which the theory predicts stability for all Ri, the critical values for the first few vertical nodes are $\mathrm{Ri}_c(m = 1, 2, 3, 4, 5, \cdots) = 8/9, 24/25, 48/49, 80/81, 120/121$, and so on. Therefore, for all practical reasons we view SymI to be relevant once the particle layer satisfies $\mathrm{Ri} < 1$ throughout most of its bulk. For the collapsing layer solutions considered in the previous subsection, this would appear to start taking root once the midplane particle layer achieves values of $\varepsilon_0 \approx 0.5$ (see, e.g., both panels of Figure 23).

5.2.4. $0 < \mu \ll 1$ Limiting form

We consider values of μ that are small, which for all practical purposes corresponds to very large values of kH_p and/or small values of ε_0; however, we consider the former case to be of practical use. From Equation (C26) we find to leading

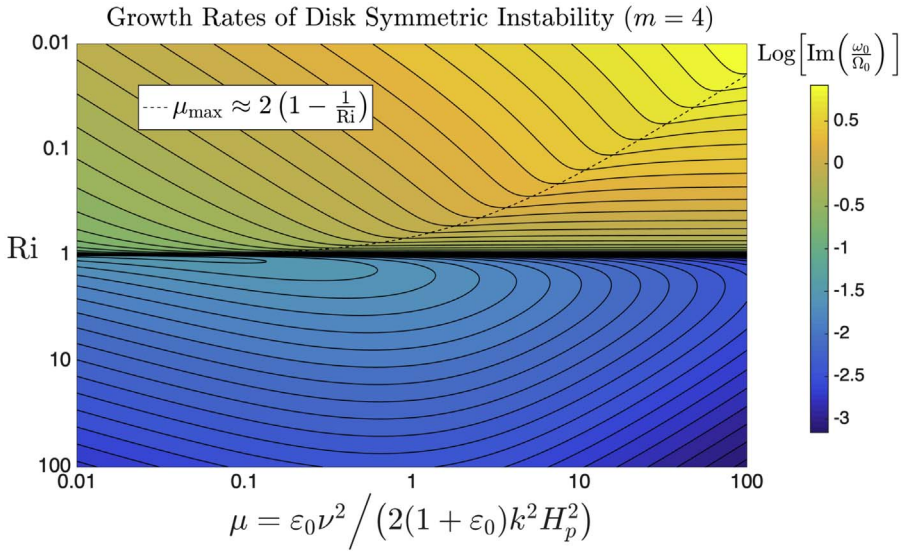

Figure 24. Growth rates of the disk analog of the symmetric instability: $m = 4$ ($\nu \equiv 2m + 1$). The general character of these growth rates is the same for all values of m, where the critical value of Ri asymptotically approaches 1. Overplotted is the approximate value $\mu = \mu_{\max}$ corresponding to the fastest-growing mode for $\mathrm{Ri} < 1$. Note that this corresponds to a distinct value $k_{\max} H_p$ that is implicitly a function of vertical node number m and other properties of the settled particle layer like ε_0 and Ri; see Equation (58).

order that

$$\frac{\omega_0^2}{\Omega_0^2} \approx i\sqrt{\frac{2\mu}{\mathrm{Ri}}}\left[\frac{1}{\nu} - \sqrt{1 - \mathrm{Ri}}\right]. \tag{54}$$

The critical value $\mathrm{Ri} = \mathrm{Ri}_c$ is easily recovered by equating to zero the expression found within the brackets. The growth rates, while nonzero all throughout $\mathrm{Ri} \neq \mathrm{Ri}_c$, are fairly muted for $\mathrm{Ri} > \mathrm{Ri}_c$ but shoot up with a dramatic change in character once $\mathrm{Ri} < \mathrm{Ri}_c$. The oscillation frequency also shows a strong shift around $\mathrm{Ri} = \mathrm{Ri}_c$.

5.2.5. m $\gg 1$ and $kH_p = \mathcal{O}(m)$: A Maximum Growth Rate

One can consider the asymptotic limiting form of Equation (50) in the limit where $m \gg 1$ together with maintaining $kH_p = \mathcal{O}(m)$. This tandem limit keeps μ an $\mathcal{O}(1)$ quantity according to its definition in Equation (49). Thus, to leading order it follows that

$$\frac{\omega_0^2}{\Omega_0^2} = \sqrt{\mu^2 - 2\mu\left(\frac{1}{\mathrm{Ri}} - 1\right)} - \mu + \mathcal{O}\left(\frac{1}{m}\right). \tag{55}$$

An elementary analysis shows that $\mathrm{Im}(\omega_0)$ achieves a maximum value when the expression underneath the square root operator equals zero. Therefore, we define a maximally growing value of μ to be

$$\mu_{\max} = 2\left(\frac{1}{\mathrm{Ri}} - 1\right), \tag{56}$$

whereupon it follows that—provided, of course, $\mathrm{Ri} < 1$—the fastest-growing mode has a growth rate, $\sigma_{\max} \equiv \mathrm{Im}(\omega_0)$, approximately given by

$$\frac{\sigma_{\max}}{\Omega_0} = \sqrt{\mu_{\max}} = \sqrt{2\left(\frac{1}{\mathrm{Ri}} - 1\right)}. \tag{57}$$

We show overlaid on Figure 24 the approximate relationship $\mu_{\max}(\mathrm{Ri})$. Finally, restoring the relationship between kH_p and μ, we find a corresponding fastest-growing horizontal mode, $k_{\max}$, to be

$$k_{\max} H_p \approx \left(m + \frac{1}{2}\right)\sqrt{\frac{\varepsilon_0}{1+\varepsilon_0} \cdot \frac{\mathrm{Ri}}{1 - \mathrm{Ri}}}. \tag{58}$$

Inspection of Figures 24–25 indicates that Equation (58) does a fairly good job at predicting the fastest-growing mode even for $\mathcal{O}(1)$ values of m. The asymptotic growth rate expression from Equation (57) works well as an upper bound. Nevertheless, its utility is self-evident, as it overpredicts the low-order m growth rates by about 25%, at most.

5.3. Transition to Secondary State via SI?

It is worthwhile to ask for the two St numbers simulated, if the transition from the shear-driven turbulence phase into the nonlinear pattern state is consistent with the SI. We consider this by estimating the growth rate of the particle scale height during this transition phase by approximating the domain-averaged time-dependent scale height $\bar{H}_p(t)$ as

$$\bar{H}_p(t) = H_{p,\alpha} + \delta h \exp\left(\frac{t}{t_g}\right). \tag{59}$$

$\bar{H}_p(t)$ can also be interpreted as the sum of a mean turbulently set particle scale height, $H_{p,\alpha}$, that also corresponds to an estimated value of $\alpha \approx \mathrm{St}(H_{p,\alpha}/H)^2$ (Dubrulle et al. 1995) and an exponentially growing perturbation piece characterized by an amplitude δh and a growth timescale t_g. The aim here is to compare the simulation-derived values of t_g with the prediction made in the theory of turbulent SI developed in Chen & Lin (2020) and Umurhan et al. (2020).

The left and middle panels of Figure 26 shows a log-linear plot of the time series for $\bar{H}_p$ for four simulations. Various dashed lines show our estimated fitted values for $H_{p,\alpha}$ and corresponding estimated slopes (dotted lines) drawn over the secondary growth phase where the approximate values of $\bar{H}_p(t) \approx \tilde{H}_p(t)$ may be read off of these lines for any input time t_i falling nominally in the growth rate time range. Based on this

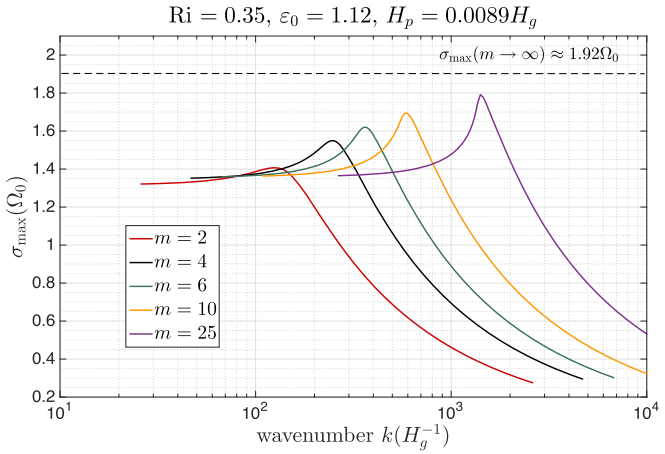

Figure 25. Following Equation (50), this figure depicts predicted growth rates of the SymI shown as a function of radial wavenumber for several vertical parameters m for a given set of values Ri, ε_0, and H_p. Following the analysis of Section 5.2.4, the asymptotic growth rate $\sigma_{\max}(m \to \infty)$ is also shown.

understanding of $\tilde{H}_p(t)$, it follows that

$$\ln\left[\tilde{H}_p(t_i) - H_{p,\alpha}\right] \approx \ln\delta + \frac{2\pi t_i}{t_g}, \tag{60}$$

which, after selecting two times from the fitted lines, allows one to estimate t_g, i.e.,

$$t_g \approx (t_2 - t_1) \Big/ \ln\left[\frac{\tilde{H}_p(t_2) - H_{p,\alpha}}{\tilde{H}_p(t_1) - H_{p,\alpha}}\right]. \tag{61}$$

Taken from the theory developed in Umurhan et al. (2020), the right panel of Figure 26 shows the predicted growth timescales of the SI for $Z = 0.01$ and $\beta = 0.05$ as a function of α and St as maximized over wavenumber. Note that the growth timescales in that study are quoted in units of local orbit times, i.e., $P_{\rm orb} = 2\pi\Omega^{-1}$. Thus, we read off the quoted values from that graph and multiply it by 2π, and we call the result $t_{g,\rm th}$ in order to compare the predicted growth rates against the values of t_g derived from the simulations presented here, the latter of which are in units of Ω^{-1}. The results of this exercise are summarized in Table 4.

Examining the right panel of Figure 26, depicting the results of the low-to-moderate-resolution runs with St = 0.2, we find that the level set during the onset of the shear-turbulent phase has a lower value of $H_{p,\alpha}$ (by about 15%) for the higher resolution of the two, a trend observed in other simulations of the SI (e.g., Yang et al. 2017; Li et al. 2018). The lower-resolution run therefore operates at a higher effective α. Theoretically it would imply a longer growth rate for the lower-resolution run, and this trend is borne out by the prediction for turbulent SI. However, a comparison of $t_{g,\rm th}$ against the measured t_g values found in Table 4 shows that the theory appears to systematically underpredict growth rates.

The middle panel of Figure 26 shows the corresponding runs for St = 0.04. The same trends, i.e., vis-à-vis shear-turbulent phase, are manifest here as well: the lower-resolution run corresponds to higher turbulence levels compared to the higher-resolution run, with concomitant faster growth rates of the latter compared to the former. However, the growth rates are vastly shorter than those predicted for the turbulent SI according to Umurhan et al. (2020).

At this stage it is difficult to conclude as to what may be driving this secondary growth, and we can at best only speculate. It might be possible for these runs that the classical SI is acting in conjunction with a secondary effect that derives from the turbulent vertical shear profile (e.g., the VSSI, Lin 2021), but that the effect of the classical SI is stronger than this secondary effect in the St = 0.2 case—resulting in a better match based on just the SI growth rates alone—while the secondary effect is stronger than the SI in the St = 0.04 case, in which the actual observed growth timescales are much shorter than those predicted from the turbulent SI prediction. We think that the VSSI is the leading candidate mechanism to explain this effect; however, an investigation of this hypothesis is outside the scope of this paper but should be considered in follow-up work.

6. Discussion

6.1. On Turbulence in Particle-laden Sheared Midplane Layers

The simulations conducted here appear to indicate that midplane-settled particle layers that are not strongly susceptible to the SI instead erupt via other stratified axisymmetric fluid instabilities involving the vertical shear of both the radial and azimuthal velocities. These instabilities appear to lead to an early turbulent phase from which some secondary processes take root, possibly involving the SI, which leads to a sinusoidal pattern state of varying degrees of coherence and characterized by some amount of radial drift.

The instability mechanisms leading to the early turbulent phase involve the particle component as a collective agent, and mainly in a stabilizing role. The flow analysis conducted indicates that the primary mechanism driving instability depends on the St number of the particle component, and although we have examined only two values of St, we can confidently say that there are at least two types of destabilizing processes: Based on the St = 0.04 suite of simulations, it appears that these settled layers primarily experience the protoplanetary disk analog of the SymI, whose dynamic relies on the vertical shear of the azimuthal velocity profile and requiring Ri < 1. Based on the St = 0.2 suite of numerical experiments, the settled layers experience radial KH roll-up within layers located about 1–2 particle scale heights away from the midplane. Further, the assessed Ri values within the settled particle layers for St = 0.2 should support, in principle at least, azimuthal KH roll-up as well, but visualization of the flow fields does not present clear evidence for it either.

During the review phase of this manuscript one of the reviewers commented on the possibility that the nonturbulent SI could explain the early bounce phase turbulent development. We have examined this possibility by doing a spot-check on the predicted growth rates for the St = 0.04 case using the laminar SI theory of YG2005. For the apparent length scales ($\lambda \sim 0.01H$) emerging during the early bounce phase (see, e.g., the w_g field in Figure 6 at $t\Omega = 6$), the predicted SI growth rate in the zero turbulent limit falls in the range $0.05\Omega_0$–$0.1\Omega_0$, which is at least a factor of 5 weaker than the corresponding growth rate of the SymI under those similar conditions. A detailed examination of this matter, to better illustrate this case, deserves to be done in the future.

In either case, however, the midplane layers exhibit unsteady motions—apparently turbulent—which eventually leads into a secondary transition resulting in a pattern-forming state. We

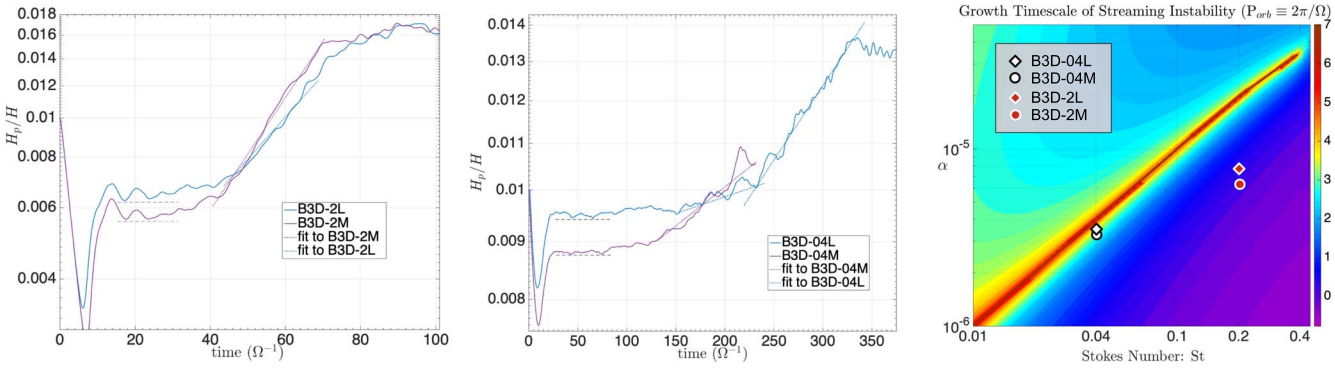

Figure 26. Particle scale height vs. time for several 3D simulations and a semilog plot, together with approximate baselines (dashed lines) for $H_{p,\alpha}$ and approximate growth lines (dotted lines) described further in the text: low-to-moderate-resolution runs for St = 0.2 (left), and low-to-moderate-resolution runs for St = 0.04 (middle). Right panel: predicted growth rates for the SI maximized over wavenumber (Umurhan et al. 2020) as a function of St and α, where the four simulations shown in the left two panels are represented with symbols. Note that all simulations appear on the relatively active side of the SI.

Table 4
Simulations and Predicted SI Growth Rates Maximized over Wavenumber

Simulations Identifier	St	$\frac{H_{p,\alpha}}{H}$	$\alpha \times 10^6$	$t_g\Omega$	$t_{g,\mathrm{th}}\Omega$
B3D-04L	0.04	0.0095	3.57	2306	15,800
B3D-04M	0.04	0.0088	3.10	59.7	2513
B3D-2L	0.2	0.00625	7.83	10.5	16.5
B3D-2M	0.2	0.0056	6.30	9.11	11.2

Note. Based on theoretical predictions of Umurhan et al. (2020).

have examined whether the drifting patterned state is an instance of the SI, and the predictions also appear mixed: for the St = 0.2 case the measured growth rates between the initial putative turbulent phase and the final pattern state appear to be consistent with SI under turbulent conditions if, however, systematically somewhat faster acting than predicted (e.g., following the theory of Chen & Lin 2020; Umurhan et al. 2020). On the other hand, in the St = 0.04 case, the corresponding measured transition phase growth rates are far more rapid than those predicted by one to two orders of magnitude (see Table 4). What is responsible for this growth, and what is the cause for the dynamical differences between these two St values, remains uncertain. Is it the SI working in tandem with a secondary process, which senses the underlying turbulent state in the mean? Might the secondary transition be an instance of the proposed VSSI, a process recently examined in a theoretical model by Lin (2021)? Furthermore, is it possible that this emergent drifting pattern state is a numerical artifact that goes away if the radial and/or azimuthal box scales are made larger? These are all questions that need immediate resolution in future studies. In Section 6.7 we further reflect on the possible action of KH roll-up for $\mathrm{Ri} > 1/4$.

Often rooted in simulations of relatively large St simulations (e.g., St > 0.2), it is a commonly held assumption that settled particle layers subject to the SI are likely also susceptible to azimuthal KH roll-up (e.g., Barranco 2009; Lee et al. 2010a, 2010b). Our findings suggest that there is, in fact, a diversity of processes at play, and which actor dominates depends on the layer's St and local metallicity Z. Indeed, the St = 0.04, Z = 0.01 simulations examined here appear to be driven entirely by the axisymmetric SymI effect. Increasing St to 0.2 while keeping Z fixed appears to lead to both the SymI and radial KH roll-up being the primary dynamical mechanisms.

6.2. On the Relationship to the Findings of Ishitsu et al. (2009)

In their unpublished study Ishitsu et al. (2009) examined the fate of particle–gas setups like those considered here, in which an imposed radial pressure gradient induces a relative streaming between gas and particles. Their simulations were 3D axisymmetric and considered two sets of St = 0.001 and 1.0. The early development of the layer in the St = 0.001 case is highly reminiscent of the transition observed in our St suite of runs. In particular, the top right panel of Figure 6 of Ishitsu et al. (2009) shows off-midplane filament development where the particle layer's vertical gradient is greatest. This character is very similar to the dynamical structure observed throughout the early development of both our 3D axisymmetric and full 3D simulations. For the St = 1.0 simulation shown, their simulation erupts into the kind of pattern characteristic of KH roll-up as reported in Barranco (2009; see, e.g., Figure 7 of that work). No such KH roll-up pattern is discernible in the St = 0.001 run reported in Ishitsu et al. (2009).

In this sense we think these authors are justified in writing "However, the instability of two-fluid shown in this work has the axis-symmetric unstable mode. As a result, the stabilization caused by the increase of the azimuthal wavenumber due to the radial shear is not effective. We expect that the instability occurs in the radial direction, and then the perturbation with small azimuthal wavenumber grows" (Ishitsu et al. 2009, pg. 14).

Not only do our 3D axisymmetric simulations confirm this notion, but our full 3D investigations suggest that nonaxisymmetric dynamics—like azimuthal KH roll-up—are not the primary instability mechanism driving turbulence in low St midplane-settled particle layers, i.e., our findings implicate axisymmetric modes as the primary driver of turbulence in full 3D scenarios.

6.3. This Study in Relation to Lin (2021)

Lin (2021) undertake a two-fluid stability analysis of a model similar in setup to what has been considered here. In that study the author considers the stability of an already-settled particle layer whose particle equilibrium is established within the framework of a local α-disk shearing-box model often used to capture the essence of particle profiles within gas-driven turbulence (e.g., Dubrulle et al. 1995; Youdin & Lithwick 2007; Laibe et al. 2020) and as recently used in the analysis of the SI by Chen & Lin (2020) and Umurhan et al. (2020). For input

values of Z, St, and α the particle–gas equilibrium in the radial–azimuthal mean admits solutions with nontrivial vertical variations in all quantities on which a numerical stability analysis is done. For conditions examined most similar to ours (see case C with the St = 0.04 runs treated here) Lin (2021) reports that the fastest-growing mode has a horizontal wavenumber $kH_g \approx 1100$ with growth rate $\sim 0.6\Omega$ and, most importantly, with a mode amplitude becoming greatest at about 1–2 scale particle scale heights. Perhaps most importantly, Lin (2021) shows that the vertical shearing instability revealed in the two-fluid setup is recovered within a single-fluid framework as well.

While our findings agree in spirit with those reported in Lin (2021), there are notable differences likely attributed to our differing steady states, since ours are drawn directly from those exhibited by actively collapsing solutions as opposed to those equilibria resulting from their adopted putative turbulence model. Since our analysis includes neither particle diffusion nor a model for turbulent viscosity, we predict that instability persists as $m \to \infty$, with corresponding fastest-growing radial wavenumber similarly diverging, and this is similar in quality for the VSSI in the inviscid limit as reported in Lin (2021). However, a notable difference in predictions of the inviscid limit is that we predict growth rates that asymptote to $\mathcal{O}(1)$ values of Ω while the VSSI seems to grow without bound as $kH \to \infty$ (see, e.g., Figure 15 of Lin 2021). Of course, viscosity due to any developing turbulence should temper growth rates at short wavelengths, at least in reality.

However, the simple setup that went into motivating the SymI analysis developed in Section 5.2 captures the essence of what occurs during the settling and transition phase of the numerical experiments conducted here, especially the St = 0.04 simulations. Both studies demonstrate that an effectively single-fluid process can lead to strong instability and quite likely explains the dynamical source of turbulence in these midplane-settled layers. Moreover, by being an effectively single-fluid model, it shows that the process does not need a relative stream between the two fluids in order to become active as required for the SI (in this regard see recent conceptual advances of Squire & Hopkins 2018a, 2018b). Despite this broad conceptual agreement, further work is needed to reconcile these two theoretical approaches. However, it would seem that the VSSI framework might be best applied in analyzing how an already-turbulent sublayer further develops, as it already has built into it a model of turbulence. Perhaps it might be used in explaining the secondary transition into the drifting pattern state we have reported on here. This is grounds for further investigation.

6.4. The Current Work in the Context of Garaud & Lin (2004)

Garaud & Lin (2004) conducted similar studies in order to investigate the evolution of the settled dust layer in a two-fluid approximation. Their work used a monodisperse population of small dust grains along with a gas disk that is strictly laminar in the absence of solids. However, in their working perturbation equations (their Equations (15)–(19)) the term containing the Coriolis force, and hence the effect of rotation in the problem, is absent. This is a major and the most important difference between their work and the current one. The emergence of SymI in the work presented here is axisymmetric in nature and emerges solely from the vertical variations of the azimuthal flow velocity that has its root in the cross-velocity components in the Coriolis term, whereas Garaud & Lin (2004) put their emphasis on the growth of nonaxisymmetric perturbations absent Coriolis influences. Hence, the evolution of the shear layer reported in their study belongs to a general class of KH instability without any possibilities of SymI. Apart from this point, Garaud & Lin (2004) put significant effort on the effect of cooling time of the stability of the shear layer, whereas we adhere to a strictly isothermal condition for our entire analysis. It is noteworthy that they observe the boundary of instability to extend beyond the classical limit of Ri = 1/4 when cooling effects are included in simplified analytical modeling. Whether these effects play a role in realistic disks remains to be explored.

6.5. A Note on Dust Settling Instability

Settling dust grains can also give rise to the dust settling instability (DSI), a by-product mechanism of the general class of resonant drag instabilities (RDIs; Squire & Hopkins 2018a; Krapp et al. 2020). As noted in Squire & Hopkins (2018a), the settling instability has two regimes: (i) for modes in which $k_x w_{sx} \neq -k_z w_{sz}$, where $\boldsymbol{w}$ is the streaming velocity, the growth rates are generally $\leqslant \Omega$, but (ii) as $k_x w_{sx} \to -k_z w_{sz}$, growth rates show divergence with increasing absolute wavenumber k. In the latter case, and so long as $w_{sz} \neq 0$, Squire & Hopkins (2018a) predict that a rapid eruption of activity will appear at the smallest length scales, with growth rates $\sim k^{1/3}$ (for $\epsilon \ll 1$). Krapp et al. (2020) observe the development of fine-scale structure in their highly resolved simulations centered on disk sections centered at heights $z \sim H_g$ with box sizes $\sim 0.1 H_g$. Most of the activity of the DSI is expected to happen far from the midplane, nominally at locations where the product combination of settling velocities and local mean dust densities is maximized. Moreover, the unrestricted growth rates for increasing wavenumber suggest that capturing the effects of DSI may need more resolution than what we have in our simulations. In our simulation results we conjecture that the DSI may be operating, especially far from the midplane, although we have not noticed any obvious signature in our simulation domain spanning only $0.2 H_g$. However, in our analytical model, the primary equations do not have any vertical velocity under equilibrium (see Equations (C2)–(C5)) that can give rise to DSI. This lack of signs of the DSI in the simulations reported here may be because the simulations take place close to the midplane, where the settling velocities are expected to be small since $w_{sz} \sim \Omega H_p \mathrm{St}$ (see, e.g., Equation (B6)). However, with sufficiently high numerical resolution the fastest-growing mode ought to appear as very short vertical wavenumber midplane parallel banded structures, which, given our current resolution capabilities, are not resolvable. Additionally, there is as yet no Richardson number analysis for the DSI based on which a more quantitative distinction between the two processes might be made. Lastly, while the DSI can lead to disorder in the flow as the flow settles, whether or not it can drive sustained midplane turbulence once the main settling phase has receded is not expected.

6.6. On Spectra and Simulation Convergence

The St = 0.2 kinetic energy power spectrum from Figure 17 makes it evident that for the 3D simulations the power-law index of the inertial range changes when we increase the

resolution. The root cause of this effect, not being properly pinpointed in this work, could be multifaceted. It is possible that the 3D simulations are not yet resolved at 512^3 resolution (2560 grids/H_g) and that higher resolution is required. Another possibility could be due to the number of particles used in the simulations with moderate and high resolutions: in order to minimize the computation expense, the number of particles used per grid point in the high-resolution run (B3D-02H) is only 0.125 (i.e., one particle per eight grids), compared to 1.0 in the moderate-resolution run (see Table 2). The gas and the particle fields in the system communicate with each other through a drag term with a finite relaxation time (Equations (2)–(4)), where the momentum exchange through the density fluctuations is nonlinear, implying scale-to-scale energy transfer. Hence, the implementation of a comparatively low number of superparticles may influence the gasdynamics. We disfavor this explanation because when settling is present particles cluster toward the disk midplane, effectively reaching more than one particle per grid. We also do not see any bottleneck effect in the gas kinetic energy beyond the dissipation scale, so the possibility of back-scattering of energy can be ruled out.

It is also interesting to note that for 3D axisymmetric simulations the energy spectra for both high- and super-high-resolution simulations are converged with similar power-law index for the inertial range. For both $\mathrm{St} = 0.2$ and 0.04, the power-law index hovers between 2.1 and 2.2. The small difference here for the two different St values is consistent with the trend reported by Pandey et al. (2019), where the authors found a dependence of the energy spectrum on the overall mass-loading effect, especially at the higher wavenumbers. Note that the highest 3D axisymmetric simulations have 10,240 grids/H_g, so it is possible that, for the full 3D simulations, going beyond 512^3 may show convergence in the energy spectrum. Given the relatively minor change in power-law slope in the 3D axisymmetric suite of runs going from high resolution (512^2) to superhigh resolution (2048^2), we cautiously conjecture that the 512^3 resolution full 3D simulation might be close to convergence for the dynamically resolved scales. Unfortunately, we were limited by available computational resources to carry out simulations with resolution higher than 512^3 and are unable to verify this conjecture at this time or characterize the turbulent behavior at high resolution for $\mathrm{St} = 0.04$.

It is also important to note that the character of the 3D axisymmetric simulations in the inertial range is fundamentally different from that of the full 3D ones, in terms of both the slope of the power spectrum and the location of the integral (k_{integral}) scale. Classic 2D turbulence is characterized by simultaneous downscale enstrophy cascade and upscale energy cascade, together with an $E_k \sim k^{-3}$ behavior in the inertial range (Kraichnan & Montgomery 1980), while in full 3D isotropic turbulence energy cascades toward smaller scales with $E_k \sim k^{-5/3}$. 3D axisymmetric scenarios in a disk might exhibit cascade properties similar to purely 2D flows, but this is not quite certain as yet. The statistical behavior under conditions where rotation and stratification are on equal footing is complicated by wave dynamics, which present alternate pathways for scale-to-scale energy exchange beyond just nonlinear velocity advection (i.e., inertial effects). Little is known about how this unfolds under this dual influence in both atmospheric/geophysical flows (see, e.g., discussion of this for atmospheric flows in Section 4.5 of Alexakis & Biferale 2018), and much less in dust-laden protoplanetary disk models. It is known that strongly stratified flows, or dimensionally constrained settings, can exhibit mixed/split and anisotropic energy cascades while strong rotation can support some amount of inverse cascade behavior under suitable forcing and/or vertical scales. In these cases new exchange pathways emerge owing to wave dynamics and produce inertial range spectral slopes that deviate from that expected from pure 2D turbulence (k^{-3}) or from full 3D Kolmogorov ($\sim k^{-5/3}$). For example, under relatively strong stratification and moderate wavenumbers in atmospheric models there exists the so-called Bolgiano−Obukhov scaling, where the kinetic energy behaves like $E_k \sim k^{-11/5}$ before it eventually turns down to $E_k \sim k^{-5/3}$ at sufficiently high wavenumbers. In this scenario energy exchange carries kinetic energy into potential energy through wave transfer via gravity waves upon which nonlinear potential energy advection forward-spreads energy toward smaller scales. In our particle-laden sheared setting there are nonlinearities in the gas−dust drag exchange terms. Exactly how this dynamical pathway mitigates and/or directs the cascade of energy—and how it ultimately shapes the resulting energy spectra—is yet to be systematically examined in 3D axisymmetric and/or full 3D settings.

In short, the energy content in these flows depends on whether the equations are being treated as full 3D or not, as well as the fact that the spatial energy distribution may not be Kolmogorov, especially at intermediate scales bridging energy injection and the very short scales that should exhibit $k^{-5/3}$ Kolmogorov character. Therefore, looking back on our results, while large-scale structures look qualitatively similar in both axisymmetric and full 3D, a one-to-one correspondence between the two may not be an accurate representation on the small scales were particles are expected to cluster. As a result, we are cautioned to infer very much about what happens on the small scales based on the results of currently available high-resolution axisymmetric simulations. We expect better light will be shed on this upon the advent of high-resolution 3D experiments or new simulation tools with wider dynamical scale resolution.

6.7. On Turbulent Activity Where $Ri > 1/4$

The persistence of activity in disks where the Richardson number exceeds the classical critical value of $1/4$ remains enigmatic. Here, we briefly review what is known about this feature of protoplanetary disk models and place our findings with regard to the SymI in that context.

Gerbig et al. (2020) unequivocally demonstrated the emergence of sustained (and probably turbulent) 3D activity in midplane-settled dust layers exhibiting $\mathrm{Ri} > 1/4$. The antecedents to this can be found in the three studies of Gómez & Ostriker (2005), Johansen et al. (2006), and Barranco (2009), where, in order to isolate and better understand operative physical effects, the stability and nonlinear response of a midplane-settled particle–disk setting were examined within a restricted 2D, azimuthal−vertical slice. Initiated with vertical shears in the azimuthal velocity field, over time it can be seen that the particle layer develops sinusoidal undulations that eventually grow in amplitude and finally erupt to generate strong vertical mixing (see esp. Barranco 2009). Johansen et al. (2006), who examined this dynamic for the two-fluid model, calculate the effective Richardson number as a function of disk

height for simulations after reaching their putative equilibrated statistical state, for which they find that $\mathrm{Ri} \approx 1$ within the confines of the disk containing most of the dust. Barranco (2009) similarly reports effective minimum Ri values that significantly exceed $1/4$ for simulations in their well-developed stage.

Gómez & Ostriker (2005) perform a corresponding stability analysis in a tractable one-fluid physical model and find that values of Ri as high as 5 could be linearly unstable. Similarly, Barranco (2009) reports the possibility of linear instability for values of Ri as high as 1.25. For the nonlinear models presented in these three studies, the period of time from initiation of a model run until the manifestation of full-fledged nonlinear layer development ranges from 5 to 10 orbit times, or, in our units, after $t\Omega = 30$–60. Similar roll-up times are reported for KH roll-up in Johansen et al. (2006).

Gómez & Ostriker (2005) and Barranco (2009) attribute to Coriolis effects the tendency for such layers to be unstable even when $\mathrm{Ri} > 1/4$. Indeed, the classic KH roll-up analysis involves the analysis of a 2D vertically sheared stratified fluid. The $\mathrm{Ri} = 1/4$ criterion is technically only appropriate for that simple setup sans rotation. The corresponding incompressible linear stability problem, in the guise of the Taylor−Goldstein equation (e.g., Garaud & Lin 2004), is technically second order in time. Introduction of Coriolis effects—i.e., in the way they appear in the disk problem considered here and in the aforementioned studies—raises the problem's temporal order by one, which certainly enriches the range of normal mode behavior. As we have seen, the added complexity introduced by rotation is also reflected in the dynamics responsible for the SymI. Indeed, the structures of the perturbation equations for the SymI—i.e., Equations (C2)–(C5)—are similar to the corresponding ones for KH roll-up considered in the single-fluid setup of Barranco (2009).

In light of these reflections, one may define a characteristic Rossby number in terms of the amplitude and scale of the azimuthal velocity shear via

$$\mathrm{Ro} = \delta v_{00}/2\Omega H_s, \tag{62}$$

e.g., like those based on averaged fits to $\langle v_g \rangle_{xy}$ or V_{cm} discussed in Section 3.5 and Equation (28) in particular. Indeed, activity persists for $\mathrm{Ri} > 1/4$ for $\mathrm{Ro} \gtrapprox 1$—especially throughout all phases of development in the $\mathrm{St} = 0.04$ suite of simulations (see last column of Table 3). This should be considered in comparison to the Rossby number of Keplerian flow, $\mathrm{Ro}_K = 3/4$. Thus, it seems that for problems of this sort the critical Richardson number should in general be a function of the Rossby number, i.e., $\mathrm{Ri}_c = \mathrm{Ri}_c(\mathrm{Ro})$, in which the classical stratified limit is recovered when rotation goes away,

$$\mathrm{Ri}_c(\mathrm{Ro} \to \infty) = 1/4. \tag{63}$$

We think that this is a worthwhile program—one that was instigated in Barranco (2009)—for future clarification in the context of midplane-settled protoplanetary disk modeling.

Nevertheless, we think that the SymI dynamics unfolding in the $\mathrm{St} = 0.04$ simulation dominate the rotationally modified KH roll-up likely simultaneously present. While we have not done a detailed KH roll-up analysis to complement that done in Barranco (2009), we can see from that study that the predicted growth rates for a configuration that most resembles our $\mathrm{St} = 0.04$ simulations, with $H_p \approx 0.01 H_g$, predicts growth rates $\sim 0.1\Omega$ (see third column, third row of Figure 5 in Barranco 2009), which is a factor of 5 times slower than what is seen in our simulations.

We think that the SymI is a part of the explanation for why such settled particle layers go turbulent in the simulations conducted both here and in Gerbig et al. (2020). All of our simulations manifest clear layer transition by 1 orbital period and fully developed nonlinear activity by 2–2.5 orbital periods (i.e., $t\Omega = 12$–15), which is far shorter than the time it takes nonaxisymmetric KH roll-up to develop according to the abovementioned studies. Therefore, we conjecture that 3D axisymmetric dynamics like the SymI and radial KH roll-up are the main drivers of activity, at least for the range of St numbers considered here. A comprehensive study in this respect should start with a theoretical single-fluid model that parses the relative importance of KH roll-up and the SymI in 3D axisymmetry. This, then, should be followed with understanding how these dynamics play out in the presence of two-stream dynamics including the SI. In principle, the results of the single-fluid theory ought to be contained in the generalized VSSI framework, particularly within its single-fluid limit (Lin 2021).

7. A Hard-boiled Summary with Some Final Remarks

We provide summary bullet points of the major findings and conclusions of this paper concerning small midplane sections of protoplanetary disks not subject to an external source of turbulence:

1. Midplane-settled particle layers impart both upon itself (as a second fluid) and upon the gas fluid a complex Ekman pattern of radial and azimuthal jets in the azimuthal−radial mean. The emergent epicyclically oscillating jet profiles are a result of the momentum exchange between the gas and particles and come about while the particles are settling toward the midplane.
2. The jet flows are subject to classic KH roll-up, as well as being unstable to the so-called SymI. The SymI relies on a mismatch in density and azimuthal velocity isolines in a rotating atmosphere and is well known to be relevant to mixing-layer dynamics in the ocean and frontogenesis in the atmosphere, among other geophysical phenomena (e.g., Hoskins 1974; Bennetts & Hoskins 1979; Thomas et al. 2013; Stamper & Taylor 2017; Zeitlin 2018; Zhou et al. 2022).
3. In the $\mathrm{St} = 0.2$ simulations radial KH roll-up appears to act in distinct layers that are at least $2H_p$–$3H_p$ away from the midplane and with relatively short growth rates $\sim \Omega$. This axisymmetric dynamic appears to be present in the previously unpublished study of Ishitsu et al. (2009), which has recently been examined in a new theoretical framework in Lin (2021). These KH roll-up dynamics play a primary role in driving instability of the midplane region for $\mathrm{St} = 0.2$, but it appears to operate together with SymI. Nonetheless, we note its significance in that this classical shear instability acts on layers substantially removed from where the particles reside, contrary to previously held assumptions or expectations.
4. The axisymmetric SymI acts primarily within $1H_p$–$2H_p$ of the midplane. Its growth rate is relatively short at $\approx 1\Omega$–2Ω, it appears to be the other main driver of midplane turbulence in the $\mathrm{St} = 0.2$ simulations, and it might be the primary—if not sole—driver of instability in

the St = 0.04 runs, as the Ri numbers are near 1 in the latter case. In the St = 0.04 case, we find that the SymI erupts into unsteady dynamics by $t\Omega = 6$, which is comparable to the KH roll-up timescale in the St = 0.2 simulation, suggesting that both processes are active and act on similar timescales. Thus, for the numerical experiments conducted here we posit that while the shapes of the mean flows that develop in settling layers are St dependent, the following unstable dynamics taking root in them are that of a single perfectly coupled fluid responding to an St-dependent flow profile.

5. We note that the SymI is distinct from the SI, as the latter emerges as a result of momentum exchange between components drifting through one another, while the former only requires strong vertical gradients in both the perturbation azimuthal gas velocity (v_g) and mean density, together with isoline misalignment between particle density and total azimuthal gas velocity ($V_K + v_g$). In essence, the SymI is effectively a single-fluid baroclinic dynamic.
6. Furthermore, we have reason to suspect that the SymI we observe in these layers is of the fundamentally same kind of mechanical process that drives the VSI based on the connection of the latter with the "sloping convection" effect well known in geophysical fluid flows (Yellin-Bergovoy et al. 2021).
7. The analytical theory we developed indicates that a layer will experience strong widespread instability in the particle layer due to the SymI once Ri < 1. The fastest-growing mode's growth rate is well approximated by Equation (57), $\sqrt{2/\mathrm{Ri} - 2}\,\Omega$, where Ri is based on the azimuthal velocity's vertical shear. The fastest-growing wavelength depends on integer vertical mode number $m > 0$ and is given in Equation (58).
8. We believe that this finding goes toward explaining the results reported in Gerbig et al. (2020), where they find that settled turbulent particle layers have effective values of Ri to be well above 1/4 but less than 1, especially for simulations where $Z > 0.01$ (see, e.g., Figure 6 of Gerbig et al. 2020). We therefore suspect that the SymI plays a role—and a prominent one depending on St—in driving midplane turbulence in all numerical computational studies of the SI in otherwise laminar disk models.
9. Given the above findings, we therefore conclude that these particle-settled midplane layers are subject to three simultaneously acting instabilities: the abovementioned two, and the SI. Based on the simulations with the specific input parameters we have conducted here, we conjecture that the SI is the weakest of the three, with the slowest growth rates (Chen & Lin 2020; Umurhan et al. 2020). We conjecture that whenever the parameters for St and Z (or Z/Π as proposed in Sekiya & Onishi 2018) permit the SI with relatively fast growth rates, it does so out of a turbulent state driven by the other two shear instabilities.
10. We have produced spacetime diagrams of the azimuthally averaged particle surface density field and have examined the azimuthally averaged particle surface densities at late times. As has been done before, in those simulations that admit the SI and allow for its nonlinear development and saturation (i.e., the $Z = 0.01$, St = 0.2 simulation), its signature is clearly visible by the emergence and maintenance of radially drifting coherent particle overdensities. In the high-resolution simulation of $Z = 0.01$, St = 0.04, the spacetime diagram indicates intermittent manifestation of overdensities—that appear to form and drift, and later dissipating only to reform and repeat this dynamic once again. At this stage it is unclear whether this observed intermittency is a result of the SI struggling to emerge or it is some other collective turbulent effect that momentarily drives particle overdensities, only to be later destroyed (e.g., Yang et al. 2018). This requires further analysis.
11. We have calibrated the PENCIL code used here by simulating 3D Kolmogorov turbulence in a nonrotating frame free of particles by forcing the simulation at approximately 1/3 the box size. We recover the expected $n_g = 5/3$ inertial range power-law behavior (i.e., $\varepsilon_{k,g} \sim k^{-n_g}$) down to a wavenumber $k_{\mathrm{N},D} = k_{\mathrm{N}}/4$, where k_{N} is the simulation's Nyquist wavenumber. At length scales smaller than $2\pi/k_{\mathrm{N},D}$ the gas kinetic energy plummets superexponentially. This therefore means that downscale-propagating turbulent kinetic energy does not appreciably reach scales less than 6–8 grid points in these simulations. All subsequent analyses, including statistical measures of underlying turbulence, are therefore here restricted to scales larger than $2\pi/k_{\mathrm{N},D}$.
12. For the particle–gas simulations done here with box sizes = $0.2H$ we conjecture that all medium-sized 256^3 simulations are not statistically converged. We have confirmed this to be the case for the St = 0.2 simulation, as the nominal inertial range power-law slopes for both the particle and gas kinetic energies ($\varepsilon_{k,p} \sim k^{-n_p}$ and $\varepsilon_{k,g} \sim k^{-n_g}$, respectively) steepen for the corresponding high-resolution 512^3 run. Unfortunately, due to limitations of available resources, we were not able to confirm this trend for a concomitant high-resolution run in the St = 0.04 case.
13. We have run a corresponding series of high-resolution (512^2-element) and super-high-resolution (2048^2-element) 3D axisymmetric simulations for which we find that the power-law slope of the gas kinetic energy appears to be converged at 512^2: for St = 0.2 we find $n_g \approx 2.1 \pm 0.05$, while for St = 0.04, $n_g \approx 2.15 \pm 0.05$. The inertial range particle kinetic energies appear converged for the St = 0.04 case with $n_p \approx 0.42 \pm 0.05$. However, the corresponding inertial range power-law slope shows steepening for St = 0.2 with $n_p = 0.92 \pm 0.1$ for high resolution and $n_p = 1.1 \pm 0.05$ at superhigh resolution.
14. Based on this 3D axisymmetric finding, we cautiously conjecture that the inertial range power slope reported for the St = 0.2 high-resolution full 3D simulation might be converged or close to convergence with $n_g = 1.37 \pm 0.03$ and $n_p = 0.64 \pm 0.04$. In that case the inertial range appears to emerge at $k \approx 200 H_g^{-1}$, corresponding to about 1/6 the box size, which is roughly 3 particle scale heights viewed symmetrically from the midplane. What these inertial range behaviors say about the nature of turbulent kinetic energy cascade remains to be understood.

Much of the findings reported in this study owe their illumination to the earlier axisymmetric study of Ishitsu et al. (2009). It therefore strongly suggests that axisymmetric instabilities primarily operate in midplane-settled particle layers

in gaseous protoplanetary disks not subject to external sources of turbulence and where the SI is at best only weakly operative. The recent results of Gerbig et al. (2020) appear to confirm that such layers are sufficiently active even though the SI is weakly operating. If such weakly turbulent disk conditions are realizable in realistic protoplanetary disk models, then it remains a challenge to understand how low St number conditions can lead to planetesimal formation. Indeed, global evolution modeling of particle growth in turbulent disks shows that disks maintain low St particles for weak to moderate levels of external turbulence during the first million years after disk formation (e.g., Estrada et al. 2016; Sengupta et al. 2019). If such externally driven turbulence scenarios shut off for some reason, then such low St number particles would settle to the midplane, then to be subjected to the particle-shear-driven turbulent state (discussed thus far), which could conceivably further act to thwart planetesimal accumulation. We are therefore swayed by the concerns stated in the conclusions of Ishitsu et al. (2009), where they write, "Thus, even though the global turbulence is weak in the dead zone, the turbulence due to the instability described in this paper may play the role of avoiding planetesimal formation and floating dust in the disk."

We are grateful to P. E. Estrada, J. N. Cuzzi, and K. Shariff of NASA-ARC for many illuminating discussions and institutional support. D.S. was supported by the NASA Postdoctoral Program (NPP) fellowship, and partly by the NASA Astrobiology Institute. O.M.U. acknowledges the NASA Planetary Science Division ISFM for Planet Formation and Exoplanets Theory at NASA/Ames for financial and computational support, as well as the NASA ROSES TCAN grant "Dynamical instabilities in the aid of planet formation in circumstellar disks" (20-TCAN20-0011). We thank the anonymous referee for many insightful comments and suggestions that significantly improved the quality of this manuscript. We are also indebted to insights shared with us by our TCAN Collaboration colleagues W. Lyra, J. Simon, C. C. Yang, and A. Youdin. All the simulations presented in this paper are performed on the NASA Advanced Supercomputing (NAS) facility, with generous computational resources provided through NPP and ISFM allocations.

Appendix A
Reformulating Particle Fluid Evolution Equations in Terms of μ

Our aim is to rewrite the particle fluid evolution Equations (3)–(4) in terms of the variable $\hat{\mu}_i \equiv \sqrt{\rho_p}U_{pi}$, i.e., in terms of the full velocity field including the background Keplerian flow. We note that within this appendix we use the usual Einstein index convention and, as such, the dummy indices i and j used here are not to be confused with the particle labeling indices i or with the grid labeling indices j used extensively in Section. 2.1. Leaving the right-hand side of Equation (4) in terms of a forcing function F_i, we input this definition into the total momentum conservation and manipulate the result accordingly. The purpose of this procedure is to have the equations appear in terms of conjugate symmetric variables in Fourier space that make assessing the energy contained in the particle component straightforward. We will take the result we develop in terms of $\sqrt{\rho_p}U_{pi}$ and then restore the definition $U_{pi} = V_K\delta_{i2} + u_{pi}$ to recover the form we seek in terms of the perturbation velocities and $\mu_i \equiv \sqrt{\rho_p}u_{pi}$, starting with

$$\partial_t \rho_p U_{pi} + \partial_j \rho_p U_{pj} U_{pi} + \epsilon_{ijm}\rho_p 2\Omega_j U_{pm} = F_{pi}, \tag{A1}$$

in which $\Omega_i = \delta_{i3}\Omega_0$ and where ϵ_{ijk} is the Levi–Civita symbol. We have after rewriting the above in terms of $\hat{\mu}_i$ that

$$F_{pi} = \rho_p^{1/2}\partial_t\hat{\mu}_i + \frac{1}{2}\rho_p^{-1/2}\hat{\mu}_i\partial_t\rho_p + \partial_j\hat{\mu}_j\hat{\mu}_i + \epsilon_{ikm}\rho_p^{1/2}2\Omega_j\hat{\mu}_m. \tag{A2}$$

We similarly reexpress the dust continuity equation as

$$\partial_t\rho_p + \hat{\mu}_j\partial_j\rho_p^{1/2} + \rho_p^{1/2}\partial_j\hat{\mu}_j = 0. \tag{A3}$$

Replacing the time derivative of ρ_p in Equation (A2) by the above expression, followed by factoring out $\rho_p^{1/2}$, reveals

$$F_{pi} = \rho_p^{1/2}\Big[\partial_t\hat{\mu}_i + \rho_p^{-1/2}\partial_j\hat{\mu}_j\hat{\mu}_i - \frac{1}{2}U_{pi}U_{pj}\partial_j\rho^{1/2} - \frac{1}{2}U_{pi}\partial_j\hat{\mu}_j + \epsilon_{ijm}2\Omega_j\hat{\mu}_m\Big]. \tag{A4}$$

We may rewrite the third term on the right-hand side of the above equation through a number of derivative-by-parts maneuvers to find

$$\begin{aligned}
-\frac{1}{2}U_{pi}U_{pj}\partial_j\rho_p^{1/2} &= -\frac{1}{2}\partial_j(U_{pi}\hat{\mu}_j) + \frac{1}{2}\rho_p^{1/2}(U_{pi}\partial_j U_{pj} + U_{pj}\partial_j U_{pi}) \\
&= -\frac{1}{2}(\hat{\mu}_j\partial_j U_{pi} + U_{pi}\partial_j\hat{\mu}_j) + \frac{1}{2}(\hat{\mu}_j\partial_j U_{pi} + \hat{\mu}_j\partial_j U_{pi}) \\
&= -\frac{1}{2}U_{pi}\partial_j\hat{\mu}_j + \frac{1}{2}\hat{\mu}_i\partial_j U_{pj},
\end{aligned} \tag{A5}$$

while

$$\rho_p^{-1/2}\partial_j\hat{\mu}_j\mu_i = U_{pj}\partial_j\hat{\mu}_i + U_{pi}\partial_j\hat{\mu}_j. \tag{A6}$$

Putting these all together yields a reworked momentum evolution equation

$$\partial_t\hat{\mu}_i + U_{pj}\partial_j\hat{\mu}_i + \frac{1}{2}\hat{\mu}_i\partial_j U_{pj} + \epsilon_{ijm}2\Omega_j\hat{\mu}_m = F_i/\sqrt{\rho_p}. \tag{A7}$$

Finally, making the replacements $\hat{\mu}_i \rightarrow \mu_i + \delta_{i2}\sqrt{\rho_p}V_K$ and $U_{pi} \rightarrow u_{pj} + \delta_{i2}V_K$, we have

$$\begin{aligned}
&\partial_t\mu_i + u_{pj}\partial_j\mu_i + V_K\partial_y\mu_i + \frac{1}{2}\mu_i\partial_j v_j \\
&+ \left(V_K\partial_t\sqrt{\rho_p} + \frac{1}{2}\sqrt{\rho_p}V_K\partial_j u_{pj} + u_{px}\partial_x\sqrt{\rho_p}V_K\right)\delta_{i2} \\
&+ \epsilon_{ijm}2\Omega_j\mu_m - 2\Omega_0\sqrt{\rho_p}V_K\delta_{i1} = F_i/\sqrt{\rho_p},
\end{aligned}$$

which, after making use of Equation (A3), becomes finally

$$\begin{aligned}
&\partial_t\mu_i + u_{pj}\partial_j\mu_i + V_K\partial_y\mu_i + \frac{1}{2}\mu_i\partial_j u_{pj} + \epsilon_{ijm}2\Omega_j\mu_m \\
&+ (u_{px}\partial_x\sqrt{\rho_p}V_K - V_K u_{pj}\partial_j\sqrt{\rho_p} - V_K^2\partial_y\sqrt{\rho_p})\delta_{i2} \\
&- 2\Omega_0\sqrt{\rho_p}V_K\delta_{i1} = F_i/\sqrt{\rho_p}.
\end{aligned} \tag{A8}$$

Energy statistics on the particle fluid may be constructed based on either of the two formulations found in Equation (A7) or Equation (A8) depending on the context of interest, whether it be the total energies (the former) or the perturbation energies (the latter). In particular, these expressions will be Fourier transformed (e.g., the transform of $\mu_i(\boldsymbol{x}) = \tilde{\mu}_{k,i}(\boldsymbol{k})$), and partial energies and their scale-to-scale transfer can be assessed within the usual prescribed narrow wavenumber bins.

Appendix B
Time-dependent Settling Solutions

We consider solutions to the horizontally uniform steady settling solutions of the system. We assume that the gas density is constant and write it here as $\overline{\rho}_g$, and we assume that the gas field has no vertical velocity component. We use capital letters to designate these solutions, e.g., for the horizontal gas velocity we have $u_g = U_g(z, t)$, and so forth for the other variables. Since by assumption $W_g = 0$, the evolution equations for the gas are

$$\partial_t U_g + 2\Omega_0 V_g = -\Pi_r - \frac{\Omega_0 \varepsilon}{\mathrm{St}}(U_g - U_p), \tag{B1}$$

$$\partial_t V_g - \frac{1}{2}\Omega_0 U_g = -\frac{\Omega_0 \varepsilon}{\mathrm{St}}(V_g - V_p), \tag{B2}$$

where the particle-to-gas ratio, written here as $\varepsilon = \rho_p(z, t)/\overline{\rho_g}$, differs from its general definition in the text (i.e., ϵ), since ρ_g is also a variable. In this way ε is a proxy for the particle density ρ_p. For the particle component, the particle density continuity equation for the particle density is

$$\partial_t \varepsilon + \partial_z(W_p \varepsilon) = 0, \tag{B3}$$

while for the particle momentum equations we have

$$\partial_t U_p + W_p \partial_z U_p + 2\Omega_0 V_p = -\Pi_r - \frac{\Omega_0}{\mathrm{St}}(U_p - U_g), \tag{B4}$$

$$\partial_t V_p + W_p \partial_z V_p - \frac{1}{2}\Omega_0 U_p = -\frac{\Omega_0}{\mathrm{St}}(V_p - V_g), \tag{B5}$$

$$\partial_t W_p + W_p \partial_z W_p = -\frac{\Omega_0}{\mathrm{St}} W_p - \Omega_0^2 z. \tag{B6}$$

We begin by analyzing Equation (B6) by noting that $W_p = -\beta\Omega_0 z$ is a solution in which β is the solution of the time evolution equation,

$$\partial_t \beta = \Omega_0\left(\beta^2 - \frac{\beta}{\mathrm{St}} + 1\right). \tag{B7}$$

Solutions to this equation depend on whether or not $\mathrm{St} \leqslant 1/2$ (Lin 2021). We define

$$\beta_\pm = \frac{1 \pm \delta}{2\mathrm{St}}; \quad \delta \equiv \sqrt{1 - 4\mathrm{St}^2}. \tag{B8}$$

When $\mathrm{St} \leqslant 1/2$, the time-asymptotic stable settling solution is given by $\beta = \beta_-$ (Lin 2021).[11] When $\mathrm{St} > 1/2$, the solution is given by

$$\beta = \frac{1}{2\mathrm{St}}\left[1 + |\delta| \tan\left(\frac{|\delta|\Omega_0 t}{2\mathrm{St}}\right)\right], \qquad \left|\frac{|\delta|\Omega_0 t}{2\mathrm{St}}\right| \leqslant \frac{\pi}{2}, \tag{B9}$$

[11] For $\mathrm{St} \leqslant 1/2$ the solution $\beta = \beta_+$ corresponds to exponentially growing perturbations.

while noting here that we will not consider these solutions any further in this study. With the purely linear dependence on z for W_p, the solution to Equation (B3) has a Gaussian form

$$\varepsilon = \varepsilon_0(t)\exp\left(-\frac{z^2}{2H_p^2}\right), \tag{B10}$$

in which

$$\frac{d\ln\varepsilon_0}{dt} = -\frac{d\ln H_p}{dt} = \beta. \tag{B11}$$

The proof of this solution follows by inserting the solution from Equation (B10) together with $W_p = -\beta\Omega_0 z$ into Equation (B3), collecting the resulting expression into like powers of z followed by setting their coefficients to zero, which produces the time dependencies on ε_0 and H_p found in Equation (B11). We note that the total vertically integrated mass is conserved, as the product $\int_{-\infty}^{\infty} \rho_d(z, t)dz = \sqrt{2\pi}\,\rho_g \varepsilon_0 \cdot H_p$ is always time-independent constant for ρ_g constant. Because we will restrict our attention to problems with $\mathrm{St} < 1/2$, in all of our subsequent analyses we will assume that β achieves its time-asymptotic value β_-, in which case

$$\varepsilon_0 = \varepsilon_{00} e^{\beta\Omega_0 t}, \qquad H_p = H_{p0} e^{-\beta\Omega_0 t}. \tag{B12}$$

The constant coefficients ε_{00} and H_{p0} relate to one another on the assumption that the vertically integrated particle density $\Sigma_p = \sqrt{2\pi}\,\varepsilon_{00} H_{p0}\rho_g(0)$ is constant, in which case

$$\varepsilon_{00} = Z\left(\frac{H_g}{H_{p0}}\right), \qquad Z \equiv \frac{\Sigma_p}{\Sigma_g}, \tag{B13}$$

where Z is the local model disk metallicity (see text). Thus, solutions to the remaining equation set are defined by the parameters Z, H_{p0}, and St.

The solutions for the remaining flow variables, U_g, U_p, V_g, V_p, may be determined from solving Equations (B1)–(B2) and (B4)–(B5) after inserting for ϵ the solution for ε found in Equation (B10), as well as replacing W_p with $-\beta\Omega z$, where $\beta = \beta_-$, (Equation (B8)). Since the problem involves the solution of a settling layer, it proves beneficial to go into a spatial coordinate frame that follows this descent as the particle scale height $H_p(t)$ shrinks over time. For example,

$$U_g(z, t) \rightarrow U_g(\varphi, t); \qquad \varphi = \exp\left(-\frac{z^2}{2H_p^2}\right), \tag{B14}$$

and similarly for U_p, V_g, V_p. φ is now an independent variable that varies between 0 and 1. In these new coordinates, partial derivatives are replaced according to their coordinate transformed forms

$$z\partial_z \longrightarrow z\left(\frac{\partial\varphi}{\partial z}\right)\partial_\varphi = -2\varphi\ln\varphi\,\partial_\varphi,$$
$$\partial_t \longrightarrow \partial_t + \left(\frac{\partial\varphi}{\partial t}\right)\partial_\varphi = \partial_t - 2(\beta\varphi\ln\varphi)\partial_\varphi. \tag{B15}$$

In these new coordinates Equations (B1)–(B2) and (B4)–(B5) are now reexpressed as

$$\partial_t U_g - W_\varphi \partial_\varphi U_g - 2\Omega_0 V_g = -\Pi_r - \frac{\Omega_0}{\mathrm{St}}\varepsilon_0\varphi(U_g - U_p), \tag{B16}$$

$$\partial_t V_g - W_\varphi \partial_\varphi V_g + (1/2)\Omega_0 U_g = \frac{\Omega_0\varepsilon_0}{\mathrm{St}}\varphi(V_g - V_p), \tag{B17}$$

$$\partial_t U_p - 2\Omega_0 V_p = \frac{\Omega_0}{\mathrm{St}}(U_p - U_g), \tag{B18}$$

$$\partial_t V_p + (1/2)\Omega_0 U_p = \frac{\Omega_0}{\mathrm{St}}(V_p - V_g), \tag{B19}$$

where the speed $W_\varphi \equiv -2\beta\varphi\ln\varphi$ is always greater than zero. Note how in this transformed coordinate system the vertical advection by W_p of the horizontal particle velocities U_p, V_p is now transformed into an effective upward advection of the horizontal gas velocities, with no more vertical advection in the particle component. This makes sense because we have moved into a reference frame that follows the evolving particle scale height. The solutions to the above set of equations are sought subject to the condition that $\partial_z U_g|_{z=0} = \partial_z V_g|_{z=0} = 0$. In all cases we have determined, these gas velocity conditions automatically impose the same conditions at the midplane for U_p, V_p (i.e., at $\varphi = 1$). We use the convention described in Umurhan et al. (2020) and write $\Pi_r = -2\delta c_s\Omega_0$, where δ is the local disk opening angle. In the limit as $z \to \infty$ we make sure that the solution behaves according to the Nakagawa solutions in the limit $\epsilon \to 0$ (Nakagawa et al. 1986; Youdin & Goodman 2005; Umurhan et al. 2020; Lin 2021), i.e.,

$$\begin{aligned} &U_g(\varphi \to 0) = 0, \quad V_g(\varphi \to 0) = -\delta c_s, \\ &V_p(\varphi \to 0) = -\tfrac{\delta c_s}{1+\mathrm{St}^2}, \quad U_p(\varphi \to 0) = -\tfrac{2\mathrm{St}\delta c_s}{1+\mathrm{St}^2}. \end{aligned} \tag{B20}$$

Evidently, all velocity variables are scaled by δc_s. Henceforth we assume $\delta = 0.05$, noting that this choice has little influence on the qualitative solutions we demonstrate forthwith.

We note that a quick eigenvalue analysis of Equations (B18)–(B19) by setting the forcing terms U_g, $V_p \to 0$ shows that the eigenvalues, σ, are decaying epicyclic oscillations: $\sigma = \pm i\Omega_0 - \Omega/\mathrm{St}$. Thus, drag forcing by the gas induces temporally decaying epicyclic motions in the particle fluid. The memory of the forcing decays away on a timescale St/Ω_0. A cursory inspection of Equations (B16)–(B17) indicates that a qualitatively similar response occurs in the gas fluid owing to the drag forcing by the particles, except that the decay timescales depend on the local value of ε, which is a function of height.

Numerical Method. We use a third-order-correct upwind differencing scheme to stably calculate the advection terms in Equations (B16)–(B17). Given the sign of the derivative terms, this amounts to a forward differencing scheme on a grid $0 \leqslant \varphi_i \leqslant 1$. To better capture the decaying behavior of the solutions as $\varphi \to 0$, we further move into a stretched coordinate system in which

$$\varphi_i = \exp\left(1 - \frac{1}{\zeta_i}\right), \tag{B21}$$

where ζ_i are points on a uniform grid between 0 and 1, endpoints included. We also note that

$$\frac{\partial\zeta}{\partial\varphi} = \frac{1}{\varphi}\left(\frac{1}{1 - \log\varphi}\right)^2, \tag{B22}$$

which is used in the actual differencing scheme described further below.

We discretize in time with time step Δt, where the time at the nth time step is given by $t_n = n\Delta t$. All dependent variables at time step n are denoted with superscripts "n." Spatial values of the dependent variables are designated by the subscript "i," where i runs from 1 to N, the total number of grid points in the domain. We implement an exponential time integrator common in varied applied mathematical studies (Cox & Matthews 2002), including some astrophysical applications (e.g., Umurhan & Regev 2004; Umurhan et al. 2007). Thus, for the particle component the evolution follows

$$\begin{aligned} U_{p,i}^{n+1} = &\exp\left(-\frac{\Delta t\Omega_0}{\mathrm{St}}\right) \\ &\cdot [U_{p,i}^n \cdot \cos(\Delta t\Omega_0) + 2V_{p,i}^n \sin(\Delta t\Omega_0)] \\ &+ \frac{\Delta t\Omega_0}{\mathrm{St}} \cdot \exp\left(-\frac{\Delta t\Omega_0}{2\mathrm{St}}\right) \\ &\cdot \left[U_{g,i}^n \cdot \cos\left(\frac{\Delta t\Omega_0}{2}\right) + 2V_{g,i}^n \sin\left(\frac{\Delta t\Omega_0}{2}\right)\right], \end{aligned} \tag{B23}$$

$$\begin{aligned} V_{p,i}^{n+1} = &\exp\left(-\frac{\Delta t\Omega_0}{\mathrm{St}}\right) \\ &\cdot \left[-\frac{1}{2}U_{p,i}^n \cdot \sin(\Delta t\Omega_0) + V_{p,i}^n \cos(\Delta t\Omega_0)\right] \\ &+ \frac{\Delta t\Omega_0}{\mathrm{St}} \cdot \exp\left(-\frac{\Delta t\Omega_0}{2\mathrm{St}}\right) \\ &\cdot \left[-\frac{1}{2}U_{g,i}^n \cdot \sin\left(\frac{\Delta t\Omega_0}{2}\right) + V_{g,i}^n \cos\left(\frac{\Delta t\Omega_0}{2}\right)\right]. \end{aligned} \tag{B24}$$

The evolution of gas velocity quantities follows

$$\begin{aligned} U_{g,i}^{n+1} = &\exp\left(-\frac{\Delta t\Omega_0}{\mathrm{St}}\varepsilon(t_n)\varphi_i\right) \cdot U_{g,i}^n \\ &+ \Delta t \exp\left(-\frac{\Delta t\Omega_0}{2\mathrm{St}}\varepsilon(t_n)\varphi_i\right) \cdot F_{g,i}^n, \end{aligned} \tag{B25}$$

$$\begin{aligned} V_{g,i}^{n+1} = &\exp\left(-\frac{\Delta t\Omega_0}{\mathrm{St}}\varepsilon(t_n)\varphi_i\right) \cdot V_{g,i}^n \\ &+ \Delta t \exp\left(-\frac{\Delta t\Omega_0}{2\mathrm{St}}\varepsilon(t_n)\varphi_i\right) \cdot G_{g,i}^n, \end{aligned} \tag{B26}$$

where

$$F_{g,i}^n = W_{\varphi,i}(D_\varphi U_g^n)_i + 2\Omega_0 V_{g,i}^n - \Pi_r + \frac{\Omega_0}{\mathrm{St}}\varepsilon_0(t_n)\varphi_i U_{p,i}^n \tag{B27}$$

$$G_{g,i}^n = W_{\varphi,i}(D_\varphi V_g^n)_i - (1/2)\Omega_0 V_{g,i}^n + \frac{\Omega_0}{\mathrm{St}}\varepsilon_0(t_n)\varphi_i V_{p,i}^n. \tag{B28}$$

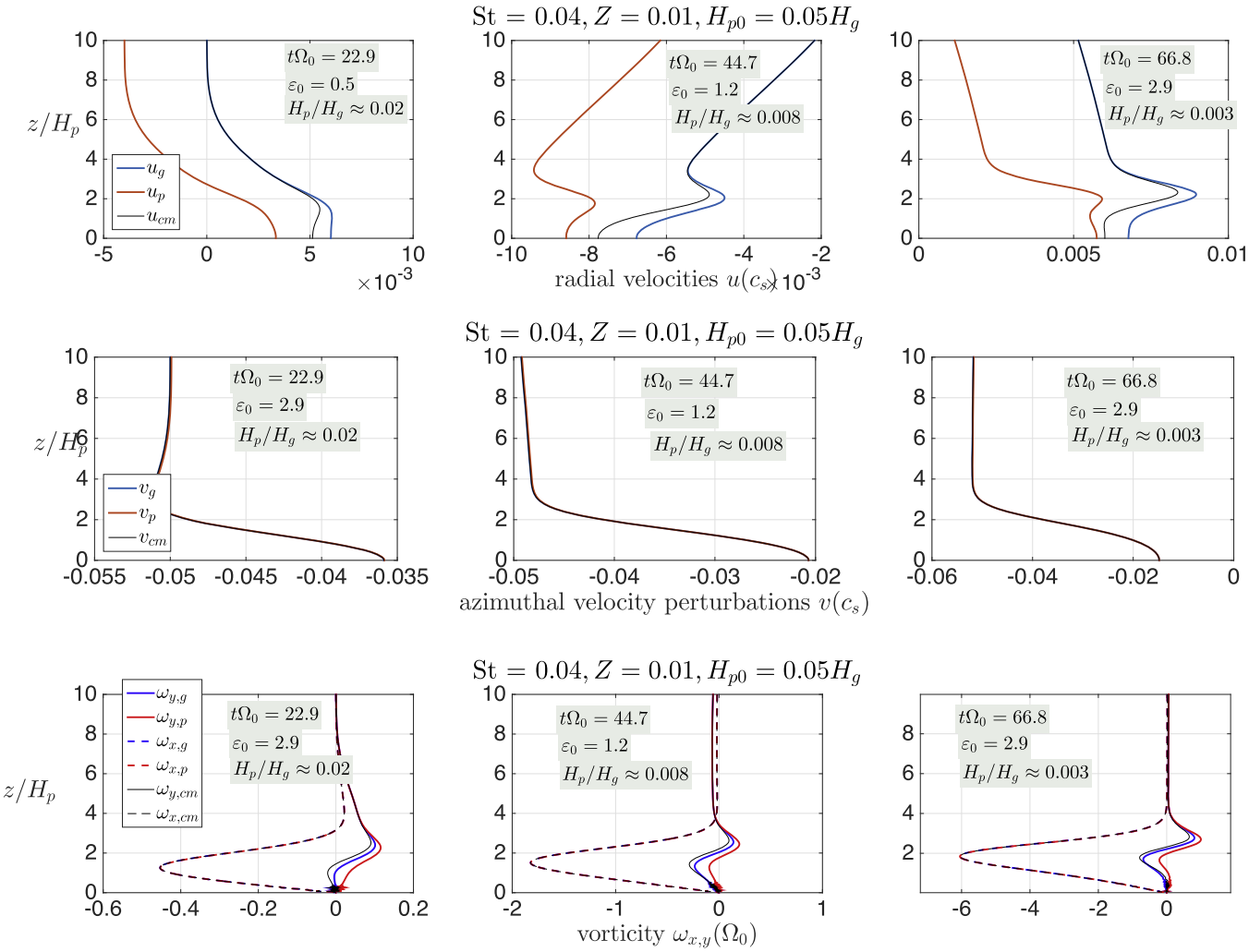

Figure B1. Like Figure 20; settling solutions for St = 0.04, $Z = 0.01$, and initial particle scale height $H_{p0} = 0.05H_g$, at three selected times.

The derivative stencil is given by a third-order forward differencing scheme in φ. Because we go into the stretched coordinates defined in Equations (B21)–(B22), this derivative operation is written out as

$$(D_\varphi U_g^n)_i \longrightarrow \left(\frac{\partial \zeta}{\partial \varphi}\right)_i \left(-\frac{11}{6}U_{g,i}^n + 3U_{g,i+1}^n - \frac{3}{2}U_{g,i+2}^n + \frac{1}{3}U_{g,i+3}^n\right), \tag{B29}$$

and similarly for $(D_\varphi V_g^n)_i$. All numerical solutions for U_g, V_g, U_p, V_p are initiated with the spatially uniform solutions found in Equation (B20). In addition, all solutions displayed in the text were derived on a uniform grid $0 \leqslant \zeta_i \leqslant 1$ with either $N = 512$ or $N = 1024$ points (the latter usually to check for convergence), and all time steps were in the range of $0.01\mathrm{St} < \Delta t < 0.025\mathrm{St}$. And finally, $\varepsilon_0(t_n) = \varepsilon_{00}\exp(\beta t_n)$.

Figures B1 and 20 display a sample set of generated solutions of the horizontal velocities and associated vorticities. A detailed discussion of these solutions may be found in the main body of the text. Note that, by Howard's semicircle theorem, the magnitude of the azimuthal vorticity denotes upper bounds of the growth rates of shear-induced instabilities when, of course, the Richardson criterion is met.

Appendix C
A Motivated Single-fluid Model Problem for the Disk Analog of the Symmetric Instability

We consider the linear normal mode response of a simplified single-fluid "toy" problem that exemplifies the essential processes we believe to be responsible for the layer overturn during the bounce phase of the simulations. As observed in the simulations, settling dust imparts momentum on the gas with a vertical dependence. The resulting collective motion of the gas and dust shows a net vertical variation in the azimuthal flow in the center-of-mass frame, as depicted in Figure 22 and shown in Figures 20 and B1. In the terminal velocity and zero stopping time limit of the recast two-fluid equations, the momentum exchange forcing will manifest as an effective nonzero vertically varying external force acting in both the radial and azimuthal directions. In the following examination we consider only the radial component of this force, $f_r(z)$, at present, and we say that it is not dynamically active. This immediately leads to a new effective steady-state azimuthal velocity $\tilde{v}_0$ that adjusts to the force, i.e.,

$$-2\Omega_0 \tilde{v}_0(z) = f_r(z); \tag{C1}$$

the analysis considered henceforth assumes single-fluid perturbations atop this basic state.

We view the instability as being primarily axisymmetric, driven by the shear in that part of the mean azimuthal flow that departs from the basic Keplerian ($=-(3/2)\Omega_0 x$), which is driven by the background pressure gradient and the particle stream, defined in the text as $\tilde{v}_0(z)$. We treat buoyancy effects driven by the particle layer in the Boussinesq approximation, namely, that density fluctuations—whether they are driven by advective motions or are a result of weak compressibility dependencies on temperature—are dynamically significant only when coupled to the external gravitational field (Spiegel & Veronis 1960). The background density field of the model single fluid is represented by $\rho_0(z)$. It is also assumed that the gas fluid is incompressible. Thus, the simple model for the perturbation quantities u', v', w', Δ' is

$$\partial_t u' - 2\Omega_0 v' = -(1/\rho_{00})\partial_x p', \tag{C2}$$

$$\partial_t v' + (1/2)\Omega_0 u' + w'\partial_z \tilde{v}_0 = 0, \tag{C3}$$

$$\partial_t w' = -(1/\rho_{00})\partial_z p' - g(z)\Delta', \tag{C4}$$

$$\partial_t \Delta' + w'\rho_0^{-1}\partial_z \rho_0 = 0. \tag{C5}$$

where ρ_{00} is taken as a reference constant scale measure of the density. These equations are supplemented with the statement of incompressiblity,

$$\partial_x u' + \partial_z w' = 0. \tag{C6}$$

The definition found in Equation (C6) motivates the definition of a stream function (ψ) and vorticity (ω') where

$$u' = \partial_z \psi', \quad w' = -\partial_x \psi',$$
$$\omega' \equiv \partial_z u' - \partial_x w' = (\partial_x^2 + \partial_z^2)\psi'. \tag{C7}$$

The vertical component of gravity is taken to be

$$g(z) = -\frac{\varepsilon_0}{1+\varepsilon_0}\Omega_0^2 z, \tag{C8}$$

where we have included the factor $\varepsilon_0/(1+\varepsilon_0)$, where ε_0 is the midplane value of ϵ, to represent an effective reduced gravity in a single-fluid formulation of the gas−particle fluid (e.g., Chiang 2008). We note that, per our observations in the simulations, the mean gas density varies little and its dynamics are largely incompressible, especially on the scales on which the particles cluster about the midplane. We therefore represent the mean density layer profile and its gradient via

$$\rho_0^{-1}\partial_z \rho_0 = \partial_z \ln \rho_0 = -\frac{z}{H_p^2}. \tag{C9}$$

The set of Equations (C2)–(C9) may be viewed as the linearized perturbations of the dual terminal velocity (i.e., "strong-drag/small-grain") and isothermal limit of the one-fluid equivalent representation of a two-fluid system, as motivated by both Laibe & Price (2014) and Lin & Youdin (2017). We note that this limit contains no two-stream effects.

We rewrite all perturbation quantities as normal modes, e.g., $\psi' \to \psi_k(z)\exp[ikx - i\omega_0 t]$, and similarly for all the other quantities. We derive an equation for the perturbation vorticity by operating on Equation (C2) by ∂_z and subtracting from it the result of operating on Equation (C4) by $-\partial_x$. After inserting the assumed normal mode form into the result, as well as into Equations (C3) and (C5), we find the following three equations:

$$-i\omega_0(\partial_z^2 - k^2)\psi_k - 2\Omega_0\partial_z v_k = ikg(z)\Delta_k, \tag{C10}$$

$$-i\omega_0 v_k - ik\psi_k\partial_z\tilde{v}_0 + (\Omega_0/2)\partial_z\psi_k = 0, \tag{C11}$$

$$-i\omega_0\Delta_k - ik\psi_k\cdot\partial_z \ln\rho_0 = 0. \tag{C12}$$

The above three equations may be further combined into a single equation for ψ_k:

$$\mathcal{L}\psi_k = (\Omega_0^2 - \omega_0^2)\partial_z^2\psi_k + 2\Omega_0 ik\partial_z(\psi_k\partial_z\tilde{v}_0) + \omega_0^2 k^2\psi_k + k^2\psi_k(g\partial_z \ln\rho_0) = 0. \tag{C13}$$

Our aim is to assess the growth rate, $\mathrm{Im}(\omega_0)$, and frequency response, $\mathrm{Re}(\omega_0)$, to perturbations to Equation (C13) subject to the condition that all perturbation quantities (i.e., ψ_k, $\partial_z\psi_k$) decay as $z \to \pm\infty$. To facilitate analytical treatment, we consider a model for the background functions that permit us to seek solutions of Equation (C13) in terms of parabolic cylinder functions $\mathcal{D}_m(\zeta)$. We therefore adopt the following:

$$g\partial_z \ln\rho_0 = -\frac{\varepsilon_0\Omega_0^2}{1+\varepsilon_0}\frac{z^2}{H_p^2}, \quad \tilde{v}_0 = v_{\mathrm{cm},\infty} + \delta v_{00}\left(1 - \frac{1}{2}\frac{z^2}{H_s^2}\right), \tag{C14}$$

where $v_{\mathrm{cm},\infty}$ is the asymptotic constant value far from the particle layer and H_s is the scale factor associated with the vertical variation of the azimuthal perturbation flow field as uncovered and discussed in the text. Typically it is slightly larger than the particle scale height H_p, but for our purposes here it is immaterial to the final outcome below. It is important that the variation in v be parabolic for what follows. Thus, Equation (C13) may be rewritten in terms of a standard parabolic cylinder equation form if we introduce

$$\psi_k = e^{-az^2/4}\Psi_k; \qquad a = -\frac{2ik\delta v_{00}\Omega_0}{H_s^2(\omega_0^2 - \Omega_0^2)}, \tag{C15}$$

and the vertically stretched coordinate $z = \tilde{\beta}\zeta$, where the scale $\tilde{\beta}$, satisfies

$$\frac{\tilde{\beta}^4\gamma^2}{\Omega_0^2 - \omega_0^2}\left(\mathrm{Ri} - \frac{\Omega_0^2}{\Omega_0^2 - \omega_0^2}\right) = \frac{1}{4}; \qquad \gamma^2(k) \equiv \frac{\delta v_{00}^2 k^2}{H_s^4}. \tag{C16}$$

We note that $\tilde{\beta}$ may be complex and that we have reexpressed constants in terms of the azimuthal form of the Richardson number, Ri_ϕ defined in Equation (24), i.e.,

$$\mathrm{Ri} \longleftrightarrow \mathrm{Ri}_\phi = -\frac{g\partial_z \ln\rho_0}{(\partial_z\tilde{v}_0)^2} = \frac{\frac{\varepsilon_0\Omega_0^2}{1+\varepsilon_0}\frac{z^2}{H_p^2}}{\frac{\delta v_{00}^2 z^2}{H_s^4}} = \frac{\varepsilon_0}{1+\varepsilon_0}\frac{H_s^4}{H_p^2}\frac{\Omega_0^2}{\delta v_{00}^2}. \tag{C17}$$

Equation (C13) now simplifies into the canonical form in terms of the nondimensional independent variable ζ,

$$\partial_\zeta^2\Psi_k + \left[\frac{\omega_0^2 k^2 - i\Omega_0\gamma}{\Omega_0^2 - \omega_0^2}\tilde{\beta}^2 - \frac{1}{4}\zeta^2\right]\Psi_k = 0. \tag{C18}$$

The solutions to the above are the standard parabolic cylinder functions $\mathcal{D}_m(z/\tilde{\beta})$ (Abramowitz & Stegun 1972), provided certain conditions ensuring that either ψ_k rapidly decays as $z \to \pm\infty$ or the quantization condition is satisfied: (i) first, the

quantization condition is

$$\frac{\omega_0^2 k^2 - i\Omega_0\gamma}{\Omega_0^2 - \omega_0^2}\tilde{\beta}^2 = m + \frac{1}{2}, \tag{C19}$$

which must be satisfied for nonnegative integer values of m; (ii) the asymptotic behavior of ψ_k for $|z|$ large is given by

$$\psi_k(|z| \to \infty) \sim \exp\left[-\left(a + \frac{1}{\tilde{\beta}^2}\right)\frac{z^2}{4}\right], \tag{C20}$$

which means that we require that

$$\mathrm{Re}\left(a + \frac{1}{\tilde{\beta}^2}\right) > 0. \tag{C21}$$

The quantization condition Equation (C19), together with Equation (C16), straightforwardly leads to solutions for ω_0^2 given by

$$\frac{\omega_0^2}{\Omega_0^2} = \sqrt{\mu\left(2\frac{\mathrm{Ri} - 1}{\mathrm{Ri}} + \mu - 2i\frac{\sqrt{2\mu/\nu^2}}{\sqrt{\mathrm{Ri}}}\right)} - \mu + i\frac{\sqrt{2\mu/\nu^2}}{\sqrt{\mathrm{Ri}}}, \tag{C22}$$

in which

$$\nu \equiv 2m + 1, \qquad \mu \equiv \frac{1}{2}\frac{\varepsilon_0}{1 + \varepsilon_0}\frac{\nu^2}{k^2 H_p^2}. \tag{C23}$$

We have deliberately rewritten the above in order to express all vertical velocity gradient information in terms of Ri.

The above form for ω_0^2 satisfies the condition that solutions exhibit Gaussian decay as $|z| \to \infty$. (The algebraic procedure also admits solutions for ω_0^2 where the sign of the first (square root) term on the right-hand side of Equation (C22) is negative. However, we find that these solutions violate the large $|z|$ asymptotic decay criterion in both the $\mathrm{Ri} \to \infty$ and $\mathrm{Ri} \to 0$ limits. There still remains the possibility that a second branch of solutions associated with this possible root might be viable in some intermediate Ri limit, but this is not yet determined at this stage.) The solutions are characterized by three parameters: the vertical node m (through ν); the parameter μ, which contains information about the stratification and the horizontal wavenumber; and Ri, containing the relative measure of shear to stratification.

We note several features. Most importantly, we see that $\omega_0 = 0$ solutions exist for specific values of Ri. Setting ω_0 to zero in both Equations (C16) and (C19) reveals that this is possible if both of the following relationships are simultaneously satisfied:

$$\tilde{\beta}^4\gamma^2(\mathrm{Ri} - 1) = \frac{1}{4}, \qquad i\tilde{\beta}^2\gamma = -\frac{\nu}{2}. \tag{C24}$$

Eliminating $\tilde{\beta}$ in both expressions shows that this is possible only when $\mathrm{Ri} = \mathrm{Ri}_c$, where

$$\mathrm{Ri}_c \equiv 1 - \frac{1}{\nu^2}. \tag{C25}$$

This condition signifies a strong change in the character of these solutions. Furthermore, a series expansion of Equation (C22) for $0 < \mu \ll 1$ shows

$$\frac{\omega_0^2}{\Omega_0^2} \approx i\sqrt{\frac{2\mu}{\mathrm{Ri}}}\left[\frac{1}{\nu} - \sqrt{1 - \mathrm{Ri}}\right] + \mathcal{O}(\mu), \tag{C26}$$

which is written by taking into account the branch cut at $\mathrm{Ri} = 1$ in the first square root term on the right-hand side of Equation (C22). The sign of the square bracketed term changes sign when Ri crosses Ri_c. In the other limit where $\mu \to \infty$ we find

$$\frac{\omega_0^2}{\Omega_0^2} \approx \left(1 - \frac{\mathrm{Ri}_c}{\mathrm{Ri}}\right)\left(1 + i\frac{1}{\nu}\sqrt{\frac{2}{\mu\mathrm{Ri}}}\right) + \mathcal{O}\left(\frac{1}{\mu}\right). \tag{C27}$$

Once again, what stands out is the gross change in character when Ri passes Ri_c. The large μ limit (high m or small horizontal wavenumbers k) shows that the leading-order behavior of ω_0 is that of weakly growing oscillations with growth rates $\mathcal{O}(\mu^{-1/2})$ when $\mathrm{Ri} > \mathrm{Ri}_c$ to very strong $\mathcal{O}(1)$ widespread growth when $\mathrm{Ri} < \mathrm{Ri}_c$. While $\mathrm{Ri} = 1$ designates an important boundary indicating a stark transition in character, we note that all normal modes show growth for all noninfinite values of Ri.

The limiting form for when the shear is nearly absent recovers at leading order the known oscillatory behavior of disk inertia−gravity oscillations. A series expansion of Equation (C22) in inverse powers of Ri reveals that

$$\frac{\omega_0^2}{\Omega_0^2} = \sqrt{\mu(2 + \mu)} - \mu + \frac{i\sqrt{2}}{\nu\sqrt{\mathrm{Ri}}}\left(\sqrt{\mu} - \mu\sqrt{\frac{1}{2 + \mu}}\right) + \mathcal{O}\left(\frac{1}{\mathrm{Ri}}\right). \tag{C28}$$

If we write $\omega_0 = \omega_{00} + i\omega_{i,0} + \cdots$ and assume that $\omega_{i,0}$ scales like $\mathrm{Ri}^{-1/2}$, then to leading order we find

$$\frac{\omega_{00}}{\Omega_0} = \pm\sqrt{\sqrt{\mu(2 + \mu)} - \mu},$$
$$\frac{\omega_{i,0}}{\Omega_0} = \frac{1}{\sqrt{2}\,\nu\omega_{00}}\left(\sqrt{\mu} - \mu\sqrt{\frac{1}{2 + \mu}}\right). \tag{C29}$$

The leading-order expression for $\tilde{\beta}^2$ (denoted by β_{00}^2) is given as

$$\frac{\tilde{\beta}_{00}^2}{H_p^2} = \frac{1}{\nu\sqrt{2}}\left(1 + \frac{1}{\varepsilon_0}\right)\sqrt{[\mu(1 + \mu - \sqrt{\mu(2 + \mu)})]}. \tag{C30}$$

We observe that the growth rate $\omega_{0,i}$ has a μ dependence, predicting growth for all values of μ, with a corresponding maximum value at $\mu \equiv \mu_{\max} = 2/3$. In this large Ri limit, we define the maximum growth rate $\omega_{\mathrm{m}} \equiv \omega_i(\mu_{\max})$ and find that it is given by

$$\frac{\omega_m}{\Omega_0} = \frac{\sqrt{1 + \frac{1}{\varepsilon_0}}}{2\sqrt{2}\,(2m + 1)}\left(\frac{\delta v_{00}}{2\Omega_0 H_p}\right) = \frac{1/\sqrt{\mathrm{Ri}}}{2\sqrt{2}\,(2m + 1)}. \tag{C31}$$

We can similarly identify the fastest-growing radial wavenumber based on the definition of μ found in Equation (C23). We define a corresponding radial wavelength for the fastest-growing mode (λ_m), related to $k_m = k(\mu = \mu_{\max})$ via

$k_m \equiv 2\pi/\lambda_m$. This leads to

$$\frac{\lambda_m}{H_p} = \frac{2\pi/\sqrt{3}}{m+\frac{1}{2}}\sqrt{1+\frac{1}{\varepsilon_0}}. \tag{C32}$$

Finally, the vertical scale characterizing variations in the parabolic cylinder function is set by β, and we estimate its value at k_m based on β's leading-order behavior found in Equation (C30). We therefore say $\widetilde{\beta}_{\max}$ where

$$\widetilde{\beta}_m \approx \widetilde{\beta}_{00}(\mu=\mu_m) = \left(\frac{1}{6\sqrt{3}}\right)^{1/4}\left[\frac{\varepsilon_0+1}{\varepsilon_0(m+1/2)}\right]^{1/2} H_p. \tag{C33}$$

In order to help generate an analytic solution to discuss the physical content of the simulations we have developed in the text, we have chosen a vertical profile for ν that extends parabolically to infinity. However, we know that the mean time-instantaneous profiles found in Section 5.1 approach constant profiles in that limit but show a parabolic profile in the region around the midplane. Furthermore, since the function $\mathcal{D}_m(z/\beta)$ shows Gaussian decay on a length scale defined by β, it is reasonable to suppose that these analytical solutions are representative of the more realistic circumstances found in Section 5.1 so long as the decay scale is less than the particle scale height, i.e., $\beta < H_p$. Additionally, the first few zeros of $\mathcal{D}_m(\zeta)$ for given values of m occur for values of $\zeta = \zeta_{0i} < 1$. This feature ensures that the modes have multiple nodes across the vertical extent. Based on this reasoning, we expect that the fastest growing of the analytic modes we have developed here are representative so long as $\tilde{\beta}_{\rm m} < 1$. Thus, by Equation (C33) we require

$$\left(\frac{1}{6\sqrt{3}}\right)^{1/4}\left(\frac{\varepsilon_0+1}{\varepsilon_0(m+1/2)}\right)^{1/2} \leqslant 1, \tag{C34}$$

and this expression places the following constraint on m:

$$m+\frac{1}{2} > \left(\frac{1}{6\sqrt{3}}\right)^{1/2}\left(\frac{1+\varepsilon_0}{\varepsilon_0}\right), \tag{C35}$$

in order to plausibly apply these approximate—though analytically derived—solutions to interpret the flow transitions considered in this study.

Let $\pm\,\zeta_{m,i}$ denote the ith zero of $\mathcal{D}_m(\zeta)$. For each order m there are m such zeros that are also those of the Hermite polynomials $\mathcal{H}_m(\zeta)$. The values of these are $\zeta_{2,\pm1} = \pm\sqrt{2}/2$, $\zeta_{3,i=\{0,\pm1\}} \approx 0, \pm 1.22474$, $\zeta_{4,i=\pm1,\pm2\}} \approx \pm 0.52464, \pm 1.65068$, $\zeta_{4,i=\{0,\pm1,\pm2\}} \approx 0, \pm 0.95857, \pm 2.02018$, and so on (Abramowitz & Stegun 1972). Because of the vertical scaling associated with the fastest-growing mode, β_m defined in Equation (C33), the distance between successive nodes for solution index m is therefore

$$\Delta z_{m,i} = \tilde{\beta}_{\rm m}(\zeta_{m,i} - \zeta_{m,i-1}). \tag{C36}$$

Due to symmetry considerations, it is enough to quantify $\Delta z_{m,i}$ by restricting consideration to values of $1 \leqslant i \leqslant m/2$ for even m and $1 \leqslant i \leqslant (m-1)/2$ for odd m.

Appendix D
Hyperdiffusion and Hyperviscosity Scheme in PENCIL Code

The flux of viscous momentum can be cast to be proportional to the rate-of-strain tensor, which can be written as

$$S_{mn} = \frac{1}{2}\left(\frac{\partial u_m}{\partial x_n} + \frac{\partial u_n}{\partial x_m} - \frac{1}{3}\delta_{mn}\nabla\cdot\boldsymbol{u}_g\right), \tag{D1}$$

which, in the incompressible limit, along with constant dynamical viscosity $\mu = \nu\rho$, translates to a viscous acceleration as $\nu\nabla^2\boldsymbol{u}_g$, where ν is the kinematic viscosity. Note that, in Equation (D1), p and q are used as dummy indices in order to denote the gas velocity components. The viscous acceleration $f_{\rm visc}$, in its most general form can be written as

$$f_{\rm visc} = \frac{1}{\rho}\nabla\cdot[2\rho\nu\boldsymbol{S}]. \tag{D2}$$

With the PENCIL code, however, we are using a higher-order (sixth) hyperdissipation, and hence the rate-of-strain tensor gets replaced by a higher-order version as follows:

$$f_{\rm visc}^{\rm (hyper)} = \frac{1}{\rho}\nabla\cdot[2\rho\nu_n\boldsymbol{S}^{(n)}]. \tag{D3}$$

Here $n = 3$, which corresponds to the sixth-order hyperdissipation. With this, a simple hyperviscosity is applied in the following form:

$$f_{\rm visc} = \begin{cases} \nu_3\nabla^6\boldsymbol{u}_g, & \text{if } \mu = \text{constant;} \\ \nu_3[\nabla^6\boldsymbol{u}_g + 2\boldsymbol{S}^{(3)}\cdot\nabla\ln\rho_g], & \text{if } \nu = \text{constant.} \end{cases} \tag{D4}$$

The spectral range over which the hyperviscosity operates is small, and it is used only as a high-frequency filter in the numerical setup. Moreover, given its artificial nature, the strict requirement of momentum conservation is dropped (Lyra et al. 2017; see also the PENCIL code manual). It is important to note that the simplified expression from Equation (D4) can be written as the divergence of a rate-of-strain tensor as

$$S_{mn}^{(3)} = \frac{\partial^5 u_m}{\partial x_n^5}. \tag{D5}$$

For more details on the hyperdissipation scheme used in the code, see the PENCIL code manual and Lyra et al. (2017).

ORCID iDs

Debanjan Sengupta https://orcid.org/0000-0003-0801-3159
Orkan M. Umurhan https://orcid.org/0000-0001-5372-4254

References

Abarbanel, H. D. I., Holm, D. D., Marsden, J. E., et al. 1984, PhRvL, 52, 2352
Abod, C. P., Simon, J. B., Li, R., et al. 2019, ApJ, 883, 192
Abramowitz, M., & Stegun, I. A. 1972, Handbook of Mathematical Functions (New York: Dover), 1972
Alexakis, A., & Biferale, L. 2018, PhR, 767, 1
Barranco, J.-A. 2009, ApJ, 691, 907
Bennetts, D. A., & Hoskins, B. J. 1979, QJRMS, 105, 945
Brandenburg, A. 2001, ApJ, 550, 824
Carrera, D., Johansen, A., & Davies, M. B. 2015, A&A, 579, A43
Chambers, J. E. 2010, Icar, 208, 505
Chandrasekhar, S. 1961, International Series of Monographs on Physics (Oxford: Clarendon), 1961
Chen, K., & Lin, M.-K. 2020, ApJ, 891, 132

Chiang, E. 2008, ApJ, 675, 1549
Cox, S. M., & Matthews, P. C. 2002, JCoPh, 176, 430
Cuzzi, J. N., Dobrovolskis, A. R., & Champney, J. M. 1993, Icar, 106, 102
Dobrovolskis, A. R., Dacles-Mariani, J. S., & Cuzzi, J. N. 1999, JGR, 104, 30805
Drazin, P. G., & Reid, W. H. 2004, in Hydrodynamic Stability, ed. P. G. Drazin & W. H. Reid (Cambridge: Cambridge Univ. Press) 626
Drazkowska, J., Bitsch, B., Lambrechts, M., et al. 2022, arXiv:2203.09759
Dubrulle, B., Morfill, G., & Sterzik, M. 1995, Icar, 114, 237
Estrada, P. R., Cuzzi, J. N., & Morgan, D. A. 2016, ApJ, 818, 200
Garaud, P., & Lin, D. N. C. 2004, ApJ, 608, 1050
Gerbig, K., Murray-Clay, R. A., Klahr, H., et al. 2020, ApJ, 895, 91
Goldreich, P., & Lynden-Bell, D. 1965, MNRAS, 130, 125
Gole, D. A., Simon, J. B., Li, R., et al. 2020, ApJ, 904, 132
Gómez, G. C., & Ostriker, E. C. 2005, ApJ, 630, 1093
Hartlep, T., & Cuzzi, J. N. 2020, ApJ, 892, 120
Hasegawa, Y., & Tsuribe, T. 2014, PASJ, 66, L2
Haugen, N. E. L., & Brandenburg, A. 2004, PhRvE, 70, 026405
Hockney, R. W., & Eastwood, J. W. 1981, Computer Simulation Using Particles (New York: McGraw-Hill), 1981
Hoskins, B. J. 1974, QJRMS, 100, 480
Howard, L. N. 1961, JFM, 10, 509
Ishitsu, N., Inutsuka, S.-I., & Sekiya, M. 2009, arXiv:0905.4404
Johansen, A., Henning, T., & Klahr, H. 2006, ApJ, 643, 1219
Johansen, A., Oishi, J. S., Mac Low, M.-M., et al. 2007, Natur, 448, 1022
Kraichnan, R. H., & Montgomery, D. 1980, RPPh, 43, 547
Krapp, L., Youdin, A. N., Kratter, K. M., et al. 2020, MNRAS, 497, 2715
Laibe, G., Bréhier, C.-E., & Lombart, M. 2020, MNRAS, 494, 5134
Laibe, G., & Price, D. J. 2014, MNRAS, 440, 2136
Latter, H. N., & Papaloizou, J. 2017, MNRAS, 472, 1432
Lee, A. T., Chiang, E., Asay-Davis, X., et al. 2010a, ApJ, 718, 1367
Lee, A. T., Chiang, E., Asay-Davis, X., et al. 2010b, ApJ, 725, 1938
Li, R., & Youdin, A. N. 2021, ApJ, 919, 107
Li, R., Youdin, A. N., & Simon, J. B. 2018, ApJ, 862, 14
Lin, M.-K. 2021, ApJ, 907, 64
Lin, M.-K., & Youdin, A. N. 2017, ApJ, 849, 129
Lyra, W., McNally, C. P., Heinemann, T., et al. 2017, AJ, 154, 146
Lyra, W., Raettig, N., & Klahr, H. 2018, RNAAS, 2, 195
Lyra, W., & Umurhan, O. M. 2019, PASP, 131, 072001
Miles, J. 1986, PhFl, 29, 3470
Miles, J. W. 1961, JFM, 10, 496
Mkhinini, N., Dubos, T., & Drobinski, P. 2013, JFM, 728, 29
Nakagawa, Y., Sekiya, M., & Hayashi, C. 1986, Icar, 67, 375
Nelson, R. P., Gressel, O., & Umurhan, O. M. 2013, MNRAS, 435, 2610
Nesvorný, D., Li, R., Youdin, A. N., et al. 2019, NatAs, 3, 808
Nimmo, F., Umurhan, O., Lisse, C. M., et al. 2017, Icar, 287, 12
Pandey, V., Perlekar, P., & Mitra, D. 2019, PhRvE, 100, 013114
Raettig, N., Lyra, W., & Klahr, H. 2021, ApJ, 913, 92
Schäfer, U., Johansen, A., & Banerjee, R. 2020, A&A, 635, A190
Sekiya, M. 1998, Icar, 133, 298
Sekiya, M., & Onishi, I. K. 2018, ApJ, 860, 140
Sengupta, D., Dodson-Robinson, S. E., Hasegawa, Y., et al. 2019, ApJ, 874, 26
Simon, J. B., Armitage, P. J., Youdin, A. N., & Li, R. 2017, ApJL, 847, L12
Spiegel, E. A., & Veronis, G. 1960, ApJ, 131, 442
Squire, J., & Hopkins, P. F. 2018a, ApJL, 856, L15
Squire, J., & Hopkins, P. F. 2018b, MNRAS, 477, 5011
Stamper, M. A., & Taylor, J. R. 2017, OcDyn, 67, 65
Stone, P. H. 1966, JAtS, 23, 390
Thomas, L. N., Taylor, J. R., Ferrari, R., et al. 2013, DSRII, 91, 96
Umurhan, O. M., Estrada, P. R., & Cuzzi, J. N. 2020, ApJ, 895, 4
Umurhan, O. M., Menou, K., & Regev, O. 2007, PhRvL, 98, 034501
Umurhan, O. M., & Regev, O. 2004, A&A, 427, 855
Vanneste, J. 1993, Math Comput Model, 17, 149
Weidenschilling, S. J. 1980, Icar, 44, 172
Yang, C.-C., Johansen, A., & Carrera, D. 2017, A&A, 606, A80
Yang, C.-C., Mac Low, M.-M., & Johansen, A. 2018, ApJ, 868, 27
Yellin-Bergovoy, R., Umurhan, O. M., & Heifetz, E. 2021, GApFD, 895, 4
Youdin, A., & Johansen, A. 2007, ApJ, 662, 613
Youdin, A. N., & Goodman, J. 2005, ApJ, 620, 459
Youdin, A. N., & Lithwick, Y. 2007, Icar, 192, 588
Zeitlin, V. 2018, PhFl, 30, 061701
Zhou, H., Dewar, W., Yang, W., et al. 2022, ComEE, 3, 28